IMPERIAL

Department of Mechanical Engineering
Imperial College London
SW7 2AZ

Application of machine learning for quality data generation and materials modelling

A thesis submitted for the Degree of Doctor of Philosophy (PhD) and the Diploma of Imperial College London

by

James Dear

September 2024

Abstract

This PhD thesis focuses on the application of machine learning (ML) techniques to thermomechanical testing, with a particular emphasis on improving strain rate control and determining constitutive properties. The integration of ML techniques into thermomechanical testing, particularly in uniaxial tensile tests, presents a novel approach to overcoming inaccuracies commonly encountered in traditional methods of Stroke-based Strain Testing (SST). The ML-based approach developed in this study provides for near-constant strain rate control, significantly reducing errors associated with non-constant strain rate and flow stress measurements.

The research employs aluminium alloy AA6082 as the primary material, where deformation behaviours under varying temperatures and strain rates were analysed. A comparison between conventional testing approaches and machine learning approach demonstrated a marked improvement in strain rate control, reducing the Mean Absolute Percentage Error (MAPE) by over 90%. Additionally, this study examines the effectiveness of several constitutive models, including the Norton-Hoff, Johnson-Cook, and ODE (Ordinary Differential Equation) based unified viscoplastic equations, which were calibrated against experimental data to enhance their reliability in metal forming simulations.

This innovative data-driven deep learning method provides an effective tool for controlling strain rate under a range of deformation conditions, allowing the accurate determination of thermomechanical properties of sheet metals.

Declaration of Originality

I confirm that the work presented in this thesis is my own and was all produced during the course of my PhD studies at Imperial College London. Any contributions from others have been highlighted and appropriately referenced. None of the work presented in this thesis has been submitted elsewhere for another qualification.

Copyright Declaration

I, James Dear, declare that the work presented in this thesis titled ‘Application of machine learning for quality data generation and materials modelling’ is my own, all else is appropriately referenced. The copyright of this thesis rests with the author. Unless otherwise indicated, its contents are licensed under a Creative Commons Attribution-NonCommercial 4.0 International Licence (CC BY-NC).

Under this licence, you may copy and redistribute the material in any medium or format. You may also create and distribute modified versions of the work. This is on the condition that: you credit the author and do not use it, or any derivative works, for a commercial purpose.

When reusing or sharing this work, ensure you make the licence terms clear to others by naming the licence and linking to the licence text. Where a work has been adapted, you should indicate that the work has been changed and describe those changes.

Please seek permission from the copyright holder for uses of this work that are not included in this licence or permitted under UK Copyright Law.

Acknowledgements

I am very grateful to my two academic supervisors, Professor Jianguo Lin FREng and Dr Zhusheng Shi, who have throughout my PhD, very effectively guided my research onto topics, of much interest to me, and have been very supportive and helpful along the way. I am also deeply indebted to Dr Ruiqiang Zhang and Jiaqi Li, who have been very helpful with advising and assisting and training me in laboratory research, as well as guidance and help, with putting together research papers. I wish to express my sincere thanks to the technical staff of the Department of Mechanical Engineering at Imperial.

My PhD research was supported by the Engineering and Physical Sciences Research Council (EPSRC) [Grant number EP/R001715/1] on "Lightform: Embedding Materials Engineering in Manufacturing with Light Alloys".

I also give special thanks to Professor Daniel Balint, Professor Bamber Blackman, Professor Li-Liang Wang, Professor Catrin Davies, Professor Mike Lowe FREng as well as Dr Jun Liu and Dr Haibao Liu, for their academic support and guidance during my PhD. I would also like to thank Professor Marc Hodes, Professor Mike Zimmerman and Professor Sevket Durucan.

I am grateful to other PhD and Postdoctoral researchers and friends who have helped me along the way, just a few mentioned here Richard Brooks, Derek Sui, Xiaochen Lu and many others at Imperial as well as Rob Crocker and James Crocker of Rolls-Royce, Bristol.

Finally, I very much appreciate the long-standing support from my partner, Angelica and our new baby, Poppy, our faithful dog, Max, as well as my sister, Caroline and my Mother and Father and Uncle for all their help and support over the years.

List of Publications

1. **J. Dear**, R. Zhang, Z. Shi and J. Lin, "Benchmarking of implicit numerical integration methods for stiff unified constitutive equations in metal forming applications", Cogent Engineering, vol. 11, no. 1, p. 2371523, 2024, doi: https://doi.org/10.1080/23311916.2024.2371523.
2. **J. Dear**, R. Zhang, Z. Shi and J. Lin, "A novel data-driven machine learning approach for improved strain rate control in thermomechanical testing of sheet metals", Engineering Applications of Artificial Intelligence, In Press.
3. **J. Dear**, Z. Shi and J. Lin, "An efficient numerical integration system for stiff unified constitutive equations for metal forming applications", in IOP Conference Series: Materials Science and Engineering, 2022, vol. 1270, no. 1: IOP Publishing, p. 012008, doi: https://doi.org/10.1088/1757-899X/1270/1/012008.

Acronyms

AA	Aluminium Alloy.
ADAM	Adaptive Moment estimation.
BDF	Backward Differentiation Formula.
BIW	Body In White
CDRX	Continuous Dynamic Recrystallisation.
CNN	Convolutional Neural Network.
DIC	Digital Image Correlation.
DIRK	Diagonally Implicit Runge Kutta.
FEA	Finite Element Analysis.
FPS	Frames Per Second.
GRU	Gated Recurrent Unit.
HFQ	Hot Forming Quench.
IE	Implicit Euler.
MSE	Mean Squared Error.
MAPE	Mean Absolute Percentage Error.
ML	Machine Learning.
NE	Number of Equations.
NN	Neural Network.
ODE	Ordinary Differential Equation.
PD	Percentage Difference.
RNN	Recurrent Neural Network.
RK	Runge Kutta.
SST	Stroke controlled based Strain Testing.
SHT	Solution Heat Treatment.
TR	Trapezoidal rule.
UTZ	Uniform Temperature Zone.
XPOL	Cross Polarisation.

Nomenclature

$\boldsymbol{A}$, $\boldsymbol{b}$ & $\boldsymbol{c}$	-	Runge-Kutta coefficients determining the order and type of method.
D & $\mathbb{C}$	-	Region of absolute stability for a numerical method & Set of complex numbers.
e	-	Local truncation error vector.
f_k	-	Shortened notation for function evaluated at t_k.
G	-	Function which arises from nonlinear root finding.
I	-	Identity matrix of size *NE*.
$\boldsymbol{J}$	-	Jacobian matrix of size *NE* evaluated at t_k.
K_i	-	Intermediate stages within the Runge-Kutta method.
$\Delta L(t)$	mm	Displacement at time *t*.
L_k	-	Total number of strain locations along the gauge length in the k^{th} dataset.
M	-	Total number of datasets used for training and testing.
N_k	-	Total number of time increments in the k^{th} dataset.
k_γ	-	Factor of truncation error within the TR-BDF2 method at γ.
$\mathcal{O}$	-	Big $\mathcal{O}$ notation, meaning the order of approximation.
$\boldsymbol{p}$	-	Vector of the material dependant parameters of the model.
$Q(\gamma)$	-	Edge of the region of stability for the TR-BDF2 at γ.
$\mathrm{Re}(z)$ & $\mathrm{Im}(z)$	-	Real and Imaginary part of a complex number.
$\mathrm{R}(z)$	-	Stability function of a given numerical method.
S_1, S_2 & S_3	-	Values for 3-different stiffness definitions.
Tol_{Abs} & Tol_{Rel}	-	Absolute & relative tolerance.
t	s	Time.
t_k	s	The time of the k^{th} step of an integration.
t_0 & t_f	s	Initial and final fracture time value.
T_k	°C	Deformation temperature for the k^{th} dataset.
$V_{\max}$, $V_{\min}$	-	Maximum or minimum values of variable V.
V'	-	Normalised variable.
$\boldsymbol{W}$	-	Matrix used in the Rosenbrock method.
X_{Input}	-	Input data structure of the ML networks.

x	mm	Position of a point along the gauge length.
Y_{Output}	-	Output data structure of the ML networks.
$\boldsymbol{y}$	-	Vector of the state variables of size *NE*; *NE* is dimension of the ODE system.
$\boldsymbol{y}_0$	-	Initial values of state-variables at t_0.
$\boldsymbol{y}_k$ & $\boldsymbol{y}_{k+1}^{(n)}$	-	Shortened notation for state-variables y at t_k & the n^{th} iteration within a Newton iteration in each root finding problem y at t_{k+1}.
$\dot{\boldsymbol{y}}$	-	Derivative of the state variables of size *NE*.
Δt	s	Step size at the k^{th} time step of an integration.
γ	-	Stability and characteristic parameter for the TR-BDF2 method, $\gamma \in (0, 1)$.
λ	-	The set of eigenvalues of the Jacobian.
λ_{min} & λ_{max}		Minimum and maximum eigenvalues of negative real part.
$\varepsilon(x,t)$, $\dot{\varepsilon}(x,t)$	- & /s	Strain and strain rate at position x and time t.
$\hat{\varepsilon}(x,t)$	-	Predicted strain.
$\dot{\varepsilon}_{\mathrm{T}}$	/s	Target strain rate.
α	-	Learning rate.

List of Tables

Table 2.1 Advantages and disadvantages of different Neural Networks. 25
Table 2.2 Comparison of different methods for strain measurement and control, highlighting their advantages and disadvantages. 39
Table 3.1 Test programme for AA6082 under HFQ conditions for conventional approach. (√) indicating a test conducted at that deformation conditions. 45
Table 3.2 Optimal setting for DIC in GOM Correlate [120]. 46
Table 4.1 Effects of deformation temperature and target strain on standard deviation and mean of the strain field when employing the conventional approach. 55
Table 4.2: Minimum and maximum values for the normalisation for each variable in inputs and outputs. 58
Table 4.3 Conditions including the deformation temperatures and strain rates of the datasets used for training and testing the LSTM networks, in which the conventional approach was adopted for the strain rate control. 59
Table 4.4: Architecture of Neural Network giving the Shape and Parameters of each layer. .60
Table 4.5: Test programme for AA6082 under HFQ conditions for machine learning approach. (√) indicating a test conducted at that deformation conditions. 64
Table 5.1 effects of deformation temperature and target strain on standard deviation and mean of the strain field, at strain of 0.5. 71
Table 5.2 MAPE between the target strain and achieved true strain for both the ML and Conv based SST 74
Table 5.3 MAPE between the target strain rate and achieved true strain rate for both the Conv and ML based SST. 76
Table 5.4 Summary of the mechanical properties of the AA6082 test piece under the different considered deformation condition for the ML approach. 85
Table 5.5 Fitted parameters of the N-H model based on ML and conventional displacement time relationships. 89
Table 5.6: Fitted parameters of the JC model for ML and Conventional displacement time relationships. 91
Table 5.7 Fitted parameters of the ODE type Equation Set 1 model for ML and conventional displacement time relationships. 94

Table 6.1 Different definitions of numerical stiffness criteria. 100
Table 6.2 Butcher Tableau used to determine the RK method. 102
Table 6.3 Butler Tableau for a DIRK method. 103
Table 6.4 Butcher tableau for the TR-BDF2 formulated as a DIRK. 104
Table 6.5 Butcher tableau for the RADAU5 formulated as a Radau IIA. 108
Table 6.6 Stability function for the implicit methods by applying the test equation Equation (6.11). 108
Table A.1 Determined material constants used to model elastic-viscoplastic deformation and material hardening of micro-alloyed steel at a temperature 1100 K. 124
Table A.2 Determined material constants for creep-ageing of AA2050-T34 at 428 K. 125
Table A.3 List of the constant values used for the set of CDRX equations for AA7050. 127

List of Figures

Figure 1.1: The Chapters of this PhD Dissertation. 6
Figure 2.1 Graph of CO_2 emitted globally by each sector as reported by [12]. 8
Figure 2.2 Distribution of manufacturing processes in the industry by weight, data sourced from [14]. 9
Figure 2.3 Structural composition of the Airbus A380 with key materials are identified [15]. 10
Figure 2.4 Metallic components of an automotive Body-In-White (BIW) – the critical components are highlighted red, in this case, are Martensitic Steel (MS) UHSS components e.g. front and rear bumpers, door frame, sill reinforcement and roll cage [17]. 11
Figure 2.5 Global production of aluminium per year (2000-2024) data sourced from International Aluminium Institute [24]. 12
Figure 2.6 Hot stamping of a steel component, showing heating, forming and quenching process leading to a component with full martensitic formation in the steel which has high strength. Martensite is a lens-like formation of BCC steel distorted by carbon which is locked into its structure and as such is very hard and strong but can be brittle unless heat treated: (a) manufacturing process; (b) temperature profile [30]. 14
Figure 2.7 Stages of the HFQ process [35]. 15
Figure 2.8 Phase diagram for an aluminium alloy AA6082 showing the different phases present for this aluminium, magnesium, silicon alloy. This is with labels X showing key temperatures for a 1.6 wt. % Mg_2Si in aluminium alloy, top X is solid solution temperature, middle X is heat treatment temperature and lower X is temperature to which alloy is quenched [36]. 16
Figure 2.9 Schematic of Forming Limit Diagram (FLD) showing the Forming Limit Curve (FLC) which identifies the onset of localised necking leading to failure [38]. 17
Figure 2.10 Schematic illustration of machine learning model. 17
Figure 2.11 AI models are improving every year [42]. 18
Figure 2.12 The growth of ML - The number of published papers containing the terms “Machine Learning” and “Materials” via the Google Scholar search engine [43]. 19
Figure 2.13 Layered structure of an Artificial Neural Network [44]. 20
Figure 2.14 Neural network designs: (a) Recurrent Neural Network (b) Feed-Forward Neural Network 21

Figure 2.15 Schematic of the neural network architecture of an RNN.....22
Figure 2.16 Schematic of the neural network architecture of a GRU.....23
Figure 2.17 The schematic structure of the LSTM cell. 24
Figure 2.18 Learning rate and overfitting: (a) The effect of learning rate on the loss during training and (b) the effect of overfitting on the training and validation loss [53]. 27
Figure 2.19 Comparison of computed (solid curves) and experimental (symbols) stress–strain relationships for AA 6082 alloy deformed at different strain rates and temperatures [91]. 33
Figure 2.20 Schematic illustration of material deformation under applied stress (σ) leading to necking and the formation of intergranular voids. The magnified view shows the microstructural details, highlighting the presence of grains and intergranular voids that contribute to material failure.....36
Figure 2.21 Conventional SST for 0.1, 0.2 and 0.5 /s.....37
Figure 3.1 Experimental configuration for themomechanical testing. 41
Figure 3.2 Temperature-time profile under HFQ conditions and experimental setup.....43
Figure 3.3 Electric and magnetic vectors of linearly and circularly polarised electromagnetic waves in the spatial domain, and the mechanism by which cross-polarisation blocks light with random polarisation angles [119].....47
Figure 3.4 Schematic diagram of an optical setup for analysing a specimen using polarised light [119].....47
Figure 4.1 Major strain fields and distributions within the gauge area at different normalised times 20%, 40%, 60%, 80% and 95%, and evolution of the major strain at the specimen centre throughout deformation under different target hot stamping conditions. 50
Figure 4.2: Scheme for collecting the strain distributions along the gauge length based on the strain fields measured using DIC. xj denotes the locations along a central gauge length of 50 mm, with an initial distance of 0.5 mm from any two adjacent locations. In particular, the specimen centre was marked as x51.....51
Figure 4.3: Data smoothing for a window size of 20, 60 and 120 using the Savitzky-Golay filter of polynomial order 2 on deformation conditions of temperature 450 °C and target strain rate of 0.1 /s.....52
Figure 4.4: True strain distribution across the aluminium alloy specimen centred at the failure point, as captured by DIC, at t/tf = 0.2, 0.4, 0.6, 0.8 and 0.95 when employing the conventional

approach. Each subfigure (a) to (f) corresponds to a unique deformation condition with temperature and target strain rate defined in the bottom left. 54
Figure 4.5 Evolution of normalised maximum strain rate at the failure location of aluminium alloy tensile specimen under varying conditions employing the conventional approach, for: (a) different temperatures of 400 °C, 450 °C and 500 °C and a target strain rate of 0.5/s, and (b) different target strain rates of 0.1, 0.5 and 2.5 /s at a constant temperature of 450 °C. 56
Figure 4.6 Schematic of training process and prediction process. 62
Figure 4.7: Evolution of training loss and testing loss (i.e. the MSE) against the number of epochs at different learning rates, and the MSE of individual datasets used for both training and testing. 63
Figure 4.8 Displacement predicted using the novel data-driven ML (solid lines) and conventional approach (dashed), for stretching specimens under different hot stamping conditions. The horizontal axis represents the product of the target strain rate ε_{Target} and time *t*, namely the target strain. 65
Figure 5.1 Comparison of the evolution of tensile force of aluminium alloy specimen for the conventional (dashed lines) and ML (solid lines) based on SST approaches, with sub-figures: (a) and (b), corresponding respectively to different temperature conditions (at the strain rate of 0.5 /s) and different strain rate conditions (at the temperature of 450 °C). 67
Figure 5.2 Comparison of the force versus displacement of an aluminium alloy tensile specimen for the conventional and ML based SST approach, with sub-figures: (a) and (b) corresponding respectively to different temperature conditions (at the strain rate of 0.5 /s) and different strain rates (at the temperature of 450 °C). 68
Figure 5.3 Different positions (0, 2.5, 5, 10 and 20 mm from the fracture location) and the calculated average strain from the corresponding sections. 69
Figure 5.4 True strain distribution across the aluminium alloy specimen centred at the failure point, as captured by DIC, at $t/tf = 0.2$, 0.4, 0.6, 0.8 and 0.95 under the ML based approach. Each sub-figure, (a) to (e), corresponds to a different temperature and strain rate combination. 70
Figure 5.5 Comparison of the evolutions of the maximum strain at the failure location of tensile specimen for the conventional and ML based SST approach with the target strain-time line (dashed, black), with sub-figures: (a) and (b) correspond respectively to different temperature

conditions (at the strain rate of 0.5 /s) and different strain rates (at the temperature of 450 °C). 72
Figure 5.6 Comparison of the evolution of normalised maximum strain rate at the failure location of aluminium alloy tensile specimen for the conventional and ML SST approach, against the target strain-time plot, with sub-figures: (a) to (e) corresponding to a different temperature and strain rate condition.....75
Figure 5.7 Strain rate distribution across the aluminium alloy specimen centred at the failure point, as captured by DIC, at t/tf = 0.3, 0.5, 0.7, and 0.9 under the ML based SST approach. 77
Figure 5.8 Comparison of true stress-strain curves obtained from the average over the cross section at the failure location, for the Conventional and ML SST approaches, for (a) different temperatures at a constant strain rate of 0.5 /s and (b) different strain rates under a constant temperature of 450 °C.....78
Figure 5.9 Flow stresses at different specific strain levels for the deformation temperature of 450 ºC and different target strain rates with the ML and conventional approaches, showing a good linear fitting and the fitted equation. σε denotes the true stress at a strain level of ε, i.e. 0.05, 0.25 and 0.5.....79
Figure 5.10 Percentage elongation at different target strain rates for constant deformation temperature of 450 ºC over the ML and conventional approaches.....81
Figure 5.11 Flow stresses at different specific strain levels under different deformation temperature for a constant target strain rate of 0.5/s using the ML and Conventional approaches. 82
Figure 5.12 Flow stress versus inverse temperature for a constant target strain rate of 0.5 /s from the ML and Conventional approaches. This is with σε denoting the true stress at a particular strain level of ε, i.e. 0.05, 0.25 and 0.5.....83
Figure 5.13 Elongation for 20 mm gauge length at different temperatures, for the ML and conventional approaches, for a target strain rate of 0.5 /s. 84
Figure 5.14 Linear fit between the strains along the different directions at deformation temperature of 450 °C and target strain rate of 0.5 /s for the ML approach, for the determination of strain ratio and Lankford coefficient. 86
Figure 5.15 Stress-strain relationships for the conventional method with: (a) different temperature and (b) different strain rate. 88

Figure 5.16 Stress-strain relationships for the ML approach with: (a) different temperature and (b) different strain rate. 89
Figure 5.17 Stress-strain relationships for the conventional method with: (a) different temperature and (b) different strain rate. 90
Figure 5.18: Stress-strain relationships for the ML approach with: (a) different temperature and (b) different strain rate. 91
Figure 5.19 Stress-strain relationships for the conventional method with: (a) different temperature and (b) different strain rate. 93
Figure 5.20 Stress-strain relationships for the ML approach with: (a) different temperature and (b) different strain rate. 94
Figure 5.21 Comparison of Mean Absolute Percentage Error (MAPE) between experimental data and different models (NH, JC, ODE) across varying conditions of temperatures and strain rates. With: (a) Conventional approach and (b) ML approach. 95
Figure 6.1 Maximum (solid curves) and minimum (dashed curves) eigenvalues and their ratios for: equation SET 1 at a strain rate of $\varepsilon T = 0.1$ /s for $0 \leq t \leq 5$ s at 1100 K, equation SET 2 at a stress level of $\sigma = 180$ MPa for $0 \leq t \leq 18$ hr at 428 K, and equation SET 3 at a strain rate of $\varepsilon T = 0.1$ /s for $0 \leq t \leq 5$ s at 693 K. 99
Figure 6.2 The factor kγ within the local truncation error and the region of absolute stability for the TR-BDF2 method. The latter is shown within the Argand diagram in which $Re\Delta t \cdot \lambda$ and $Im\Delta t \cdot \lambda$ denote the real and imaginary part, respectively, of a complex number $\Delta t \cdot \lambda$. 106
Figure 6.3 Regions of absolute stability D for each numerical method, IE, TR, TR-BDF2, R23 and RADAU5. $Re\Delta t \cdot \lambda$ and $Im\Delta t \cdot \lambda$ denote the real and imaginary part, respectively, of a complex number $\Delta t \cdot \lambda$. 109
Figure 6.4 Computations of the constitutive equation SET 1 at three different strain rates $\varepsilon T = 0.01, 0.1, 1$ /s for $0 \leq t \leq 0.5\varepsilon T$ s at 1100 K. 111
Figure 6.5 Numerical benchmarking of the five considered implicit integration methods (IE, TR, TR-BDF2, R23, and RADAU5) against equation SET 1 at a strain rate of $\varepsilon T = 0.1$ /s for the time interval of $0 \leq t \leq 5$ s. 112
Figure 6.6 Comparison of stiffness criteria S1 and S3 evaluated over the solution trajectory for equation SET 2, for three different stresses $\sigma = 140, 180, 220$ MPa at 428 K for the time interval of $0 \leq t \leq 18$ hr. 114

Figure 6.7 Numerical benchmarking of the five considered implicit integration methods (IE, TR, TR-BDF2, R23, and RADAU5) against equation SET 2 at $\sigma = 180$ MPa for the time interval of $0 \leq t \leq 18$ hr. 115
Figure 6.8 Computations of constitutive equations SET 3, at three different strain rates given by $\varepsilon T = 0.01, 0.1, 1$ /s and at a temperature of 693 K for the time interval of $0 \leq t \leq 0.5\varepsilon T$ s. 116
Figure 6.9 Numerical benchmarking of the five considered implicit integration methods (IE, TR, TR-BDF2, R23, and RADAU5) against equation SET 3 at $\varepsilon T = 0.1$ /s and 693 K for the time interval of $0 \leq t \leq 5$ s. 117

Table of Content

Abstract ..... *I*

Declaration of Originality ..... *II*

Copyright Declaration ..... *III*

Acknowledgements ..... *IV*

List of Publications ..... *V*

Acronyms ..... *VI*

Nomenclature ..... *VII*

List of Tables ..... *IX*

List of Figures ..... *XI*

Table of Content ..... *XVII*

1 Introduction *1*

1.1 Background **1**

1.2 Problem Description for this PhD Research **2**

1.3 Main aim and objectives **4**

1.4 Structure of the Thesis **5**

2 Literature Review *7*

2.1 Introduction **7**

2.2 Lightweighting **7**

2.2.1 CO_2 emission and lightweighting 7

2.2.2 Structures 9

2.2.3 Aluminium alloy 12

2.2.4 Hot stamping and HFQ 13

2.3 Machine Learning **17**

2.3.1 Artificial Neural Networks (ANNs) 19

2.3.2 Recurrent Neural Networks (RNNs) 21

2.3.3 Gated Recurrent Unit (GRU) 22
2.3.4 Long Short-Term Memory (LSTM) 23
2.3.5 Adams optimiser 25
2.3.6 Effect of hyperparameters 26
2.4 Machine Learning Applications in Materials Testing and Modelling 27
2.5 Unified constitutive equations 29
2.5.1 Holloman power law 29
2.5.2 Norton-Hoff model 30
2.5.3 Johnson-Cook model 30
2.5.4 ODE-type unified constitutive equations 31
2.5.5 Unified constitutive equations for HFQ 32
2.5.6 Numerical integration of constitutive equations 33
2.6 Thermomechanical Testing for Metal Forming 35
2.6.1 Comparison of different types of strain rate control 36
2.7 Summary 39
3 Experimental Methodologies 40
3.1 Introduction 40
3.2 Material and specimen design 40
3.3 Thermomechanical tensile tests 40
3.3.1 Experimental setup 42
3.3.2 Testing conditions 44
3.3.3 Digital Image Correlation (DIC) 45
3.4 Summary of main findings and relation to the following Chapters 48
4 Deep Learning Platform Approach 49
4.1 Introduction 49
4.2 Data collection and preparation 49
4.2.1 Data pre-processing 49
4.2.2 Data characteristics 52
4.2.3 Data normalisation 57

4.3 Learning strategies and architecture of LSTM models 58
4.3.1 Training data structure 59
4.3.2 Deep learning platform 61
4.4 Effect of learning rate 62
4.5 Uniaxial test programme using ML predictions. 63
4.6 Displacement relationships 64
4.7 Discussion of main findings 65
5 Experimental Results for Materials Characterisation 66
5.1 Introduction 66
5.2 Force and displacement relations 66
5.3 Strain distribution and evolution 68
5.4 Strain rate evolution 74
5.5 Stress-strain behaviour 77
5.6 Effect of strain rate on stresses and ductility 79
5.7 Effect of temperature on stresses and ductility 81
5.8 Viscoplastic constitutive models 86
5.8.1 Norton-Hoff model 87
5.8.2 Johnson-Cook model 89
5.8.3 Ordinary Differential Equation (ODE)-type unified constitutive model 91
5.9 Summary of main findings 95
6 Numerical Benchmarking for Constitutive Equations 97
6.1 Introduction 97
6.1.1 Numerical stiffness assessment 98
6.2 Implicit methods for stiff ODEs 100
6.2.1 Implicit Euler (IE) 101
6.2.2 Runge-Kutta (RK) methods 101
6.2.3 Trapezoidal Rule-Backwards Differentiation Formulae 2 (TR-BDF2) 103

6.2.4 Rosenbrock 2-3 (R-23) method 106
6.2.5 RADAU5 method 107
6.3 Comparison of stability regions of RK methods 108
6.4 Numerical computations of stiff ODEs using implicit methods 109
6.4.1 Numerical computations of stiff equation SET 1 110
6.4.2 Numerical computations of stiff equation SET 2 112
6.4.3 Numerical computations of stiff equation SET 3 115
6.5 Summary 117
7 Conclusions and Future Work 119
7.1 Conclusions 119
7.1.1 Application of the machine learning approach 119
7.1.2 Thermomechanical properties of AA6082 under HFQ 120
7.1.3 Unified constitutive equation determination 120
7.1.4 Numerical integration 121
7.2 Suggestions for future work 122
Appendix A 123
Material forming dataset for warm forming – SET 1 123
Material dataset for creep ageing deformation of aluminium alloy – SET 2 124
Material forming dataset for recrystallisation of aluminium alloys - SET 3 125
References 128

1 Introduction

1.1 Background

Metal forming, in its various kinds, has been around since very early days. The Chinese were some of the first people to produce very intricate designs in metal, for example, the Bronze chariots and horses in the Mausoleum of the First Qin Emperor were fabricated when Terracotta Army was constructed more than 2000 years ago [1]. In recent times, much of the focus of the current research has been directed at producing strong lightweight metallic structures for transport systems, whether they be automotive cars, railway vehicles, buses, trams or aircraft structures. Reducing the mass and still maintaining strength for crashworthiness is a key consideration in terms of the safety of personal and public transport systems. Aluminium alloys, particularly those alloys that can be strengthened by precipitation hardening are very attractive as lightweight strong metals. These alloys include the 2000, 6000 and 7000 series aluminium alloys. There are also some superalloys, e.g. Nickel superalloys for the hot section and turbine blades of a jet engine and some stainless steels which exhibit this phenomenon. A precipitation hardening alloy, sometimes called an age hardening or particle hardening alloy is subject to a final process of heat treatment to increases its strength. The heat treatment temperature is chosen to produce a fine distribution of precipitates, or particles of another phase, in the metallic structure which impede dislocation motion and so increase the strength. Aluminum alloy AA6082 was selected as the focus material and is known for its lightweight properties and high strength-to-weight ratio [2]. The alloy AA6082 has excellent corrosion resistance, good weldability and high strength and is often used in aerospace components, automotive structures, and marine applications.

Understanding the material deformation behaviour is very important for metal forming. Thermomechanical uniaxial tensile tests are commonly conducted to understand how a material deforms under combined thermal and mechanical loading conditions. Thermomechanical tensile testing under hot stamping conditions is often conducted within the highly capable Gleeble 3800 thermal-mechanical simulator. This is because the Gleeble simulator gives a particularly good replication of complex thermal cycles involved in real world metal forming processes [3, 4]. Thermal control to the specified thermal cycle is achieved using integrated feedback control systems to ensure accurate and repeatable results.

Within the Gleeble simulator, temperature control of the specimen is measured using thermocouples and induced by the Joule heating effect caused by the current flow along the specimen. This PhD research is focussed on obtaining accurate constitutive relationships for aluminium alloys.

Machine Learning (ML) has emerged as a new tool in material science and metal forming, that enables neural networks to learn patterns and relationships from data without explicit programming. It works by training algorithms on input data to recognise patterns, relationships, or trends, which can then be used to make accurate predictions under different scenarios. ML based methods are particularly useful in handling nonlinearities, high-dimensional data, and interactions that are challenging to model with traditional analytical methods. Additionally, once trained, ML models are computationally more efficient than approaches like Finite Element Analysis (FEA). The primary aim of this thesis is to leverage these state-of-the-art Machine Learning and related techniques to advance understanding and quality data generation in Gleeble tensile testing.

1.2 Problem Description for this PhD Research

During Gleeble thermomechanical testing, the temperature is accurately controlled to a complex temperature profile specified by users' requirements. However, the heat loss by the water-cooled jaws holding the specimen in place, results in a temperature gradient and non-homogeneous deformation. The effects of specimen design on the temperature gradient were analysed in detail in [5] and subsequently these temperature gradient effects were reduced by grip designs in [6]. Even under improved specimen designs, the existence of a temperature gradient is still inevitable because of the water-cooled jaws, and further improvement in the temperature gradient by specimen modification is very difficult. Tensile tests are conducted to understand how a material deforms under combined thermal and mechanical loading. Aluminium alloy exhibits sensitivity to strain rate and the temperature of the deformation and these conditions play a significant role in the complex deformation. Many researchers use thermomechanical testing to establish constitutive relationships under different hot/warm forming processes for a wide variety of deformation conditions within the Gleeble simulator. Failure to control accurately the deformation temperature or strain rate during tensile testing leads to the measured mechanical properties, such as yield strength and strain-hardening

behaviour being inaccurately determined. Consequently, those inaccurate testing results lead to inaccurate material models and predictions because material constants for the material model are calibrated against the thermomechanical testing results.

With improvements in the ability to measure strain, an important consideration is the accurate strain rate control in thermomechanical testing. Over the years, many different methods of strain rate control have been adopted. Some researchers use L-gauge where the average strain over a fixed gauge length is used to control the displacement [7]. The L-gauge can only provide adequate strain rate control over the gauge length if the strain distribution is uniform. Similarly, a C-gauge can be employed to measure the lateral, or transverse strain, by clamping the gauge at the midpoint of the specimen [8]. However, the C-gauge could sometimes be inadequate, as the deformation and subsequent fracture location does not always exactly coincide with the geometrical midpoint. As a result, neither the L-gauge nor C-gauge can provide reliable strain rate control. Most commonly in practice, Stroke-based Strain Testing (SST) is used where pre-determined displacement-time relationship are used to control the grip-to-grip displacement within the simulator. Researchers adopted relationships by making different assumptions on the deformation. The most used conventional strain rate control is by identifying the Uniform Temperature Zone (UTZ) and assuming uniform strain over the UTZ. However, due to localisation of deformation in, for example, a neck, or other local reduction of width or thickness of the test piece, it is difficult to provide a constant maximum strain rate through the specimen once the neck forms. Improved strain rate control was achieved at an evaluated temperature by conducting tests with constant tensile displacement rate under a new grip design [6]. However, a divergence between the target strain rate and the measured strain rate was found during localisation of strain caused by necking and other effects. When employing the conventional strain rate control relationship, it was found in all cases that the maximum strain rate exceeded the target strain rate by up to 500% [9]. This also means that the measured stress-strain behaviour may vary and is dependent on the method of strain rate control. In many cases, strain rate control is a major problem, and this means that it is difficult to determine whether the observed hardening behaviour during plasticity is due to strain and strain rate hardening effects or poor strain rate control.

Determination of the exact displacement-time relationship for each deformation temperature, and target strain rate, is significantly challenging because the strain field is also dependent on

the temperature gradient, applied strain rate, thermal expansion, specimen geometry and other factors. Therefore, a machine learning approach, to predict the strain field under a non-uniform temperature distribution, for a wide variety of deformation conditions, is needed. This is so an exact displacement-time relationship can be determined which provides optimised strain rate control under that target strain rate and deformation temperature.

1.3 Main aim and objectives

The main aim of this research is to develop approaches for better strain rate control to make accurate measurements of the stress-strain relationships for metallic alloys to be employed in metal forming. This is such that the yield and plastic deformation of the metallic alloys and its dependence on temperature and strain rate, as employed in metal forming processes, can be determined accurately. A key problem, when employing the Gleeble 3800 Thermal-Mechanical simulator to obtain these constitutive relationships for a metallic alloy is that a neck forms, usually at the centre of the gauge section and this leads to a localisation of strain and local increase of strain rate and so it is difficult to precisely define a constant strain rate for the stress-strain curve.

The following are the key objectives of the research:

1. Make use of Machine Learning (ML) to develop approaches to accurately control the strain rate in thermomechanical tests and determine the constitutive properties for the metallic alloys and understand better the precise stress-strain behaviour.
2. Obtain high quality experimental data for tensile testing of aluminium alloy AA6082 using the Gleeble 3800 Thermal-Mechanical simulator to determine the constitutive stress-strain behaviour of metallic alloys for metal forming applications.
3. Employ mathematical methods and numerical techniques to understand better the physics, micro-mechanical and metallurgical effects where appropriate.
4. Compare the methods of assessment of numerical stiffness in ODE-based unified constitutive equations for metal forming and benchmark the use of different implicit numerical solvers on three representative stiff unified constitutive equations.

1.4 Structure of the Thesis

The thesis has seven chapters, as shown in Figure 1.1, with further description of each chapter below.

Chapter 1. Introduces the background, objectives, as well as thesis structure for this PhD Dissertation.

Chapter 2. Reviews the literature, including hot stamping, machine learning and numerical modelling and integration. Furthermore, the hot deformation behaviours of aluminium alloys are reviewed and highlighted as a key interest of this PhD research.

Chapter 3. Outlines the experimental procedures employed in this research.

Chapter 4. Defines the principles of Machine Learning (ML) which is the technique mostly employed for analysis of the experimental data.

Chapter 5. Presents experimental results for the deformation behaviour of AA6082 under Hot Forming Quench (HFQ) at various temperatures and strain rates.

Chapter 6. Investigates the use of numerical benchmarking of different numerical solvers on three Ordinary Differential Equations (ODE) type constitutive equations which have been identified as numerical stiff.

Chapter 7. Summarises the main outcomes of this PhD research and suggests future work.

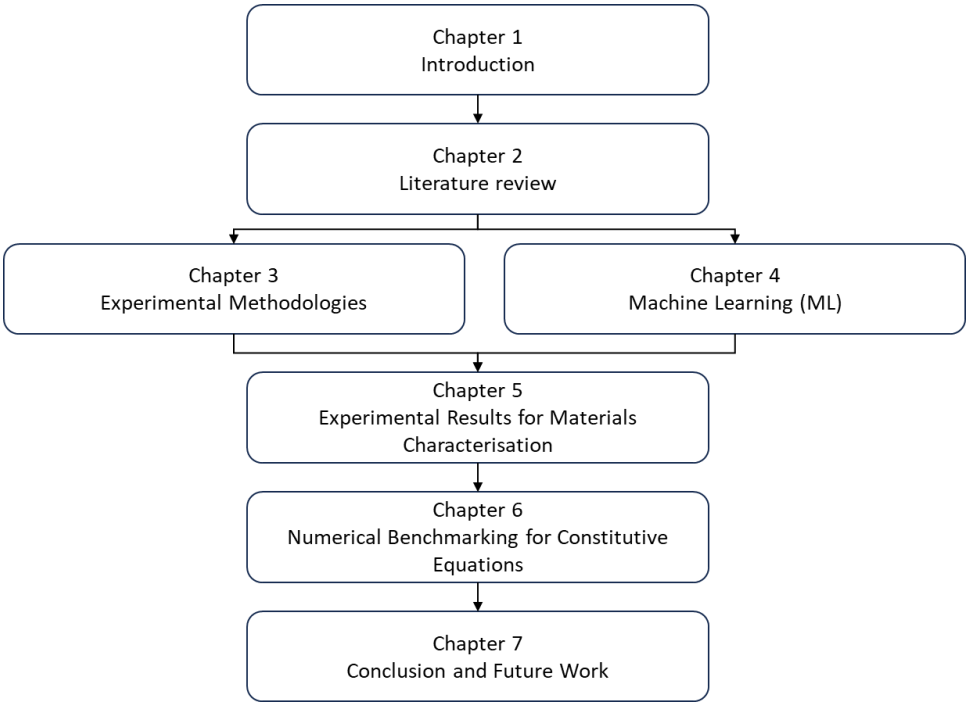


Figure 1.1: The Chapters of this PhD Dissertation.

2 Literature Review

2.1 Introduction

This chapter first emphasises, in Section 2.2, the importance of controlling CO_2 emissions in both the road transport and other industrial sectors, particularly through the strategy of lightweighting materials. Sections 2.3 and 2.4 review the basic machine learning models and explore the integration of Machine Learning (ML) particularly for application into experimental testing for metal forming processes, underscoring its potential to enhance material characterisation. Section 2.5 reviews constitutive modelling, which is crucial for accurately predicting material behaviour under various deformation conditions, and related numerical integration methods to solve the constitutive equations. Furthermore, Section 2.6 introduces thermomechanical testing for obtaining experimental data for constitutive modelling and compares available methods of strain rate control within the context of thermomechanical testing, highlighting the specific challenges and advantages associated with each method. By comparing and reviewing these approaches, the chapter provides critical insights that lay the groundwork for the innovative methodologies proposed in this research, aimed at improving material characterisation and optimising the thermomechanical testing process.

2.2 Lightweighting

2.2.1 CO_2 emission and lightweighting

According to the "Our World in Data", in 2020, around 25 billion tonnes (25 Gt) of CO_2 were emitted globally from the transportation sector, as shown in Figure 2.1. There has been a steady rise from 1990 where reported just under 20 Gt CO_2 globally from the road transport sector [10]. The drop in 2020 was due to the pandemic. The main contributor to CO_2 emissions is from road vehicles as illustrated in Figure 2.1, with the aviation and marine sectors being the next biggest contributors. The rail and pipeline sectors contribute at a very small level.

The adoption of alternative and clean fuels such as electric cars or hydrogen fuels cells has become more common but are far from widely adopted. A short-term strategy involves developing lightweight vehicles. The primary objective of lightweight construction design concepts is to minimise unnecessary weight of a vehicle, without compromising on its function

and safety e.g. crashworthiness. Clearly, reduction in vehicle weight improves fuel and associated energy efficiency and reduces emissions. It has been suggested, by the International Aluminium Institute, that for every 1 kg of aluminium alloy which is used to replace a heavier metal like steel, the car saves 20 kg of CO_2 over the lifetime of the vehicle. So there is a clear benefit in switching from heavy steel to light aluminium to reduce CO_2 emissions [11].

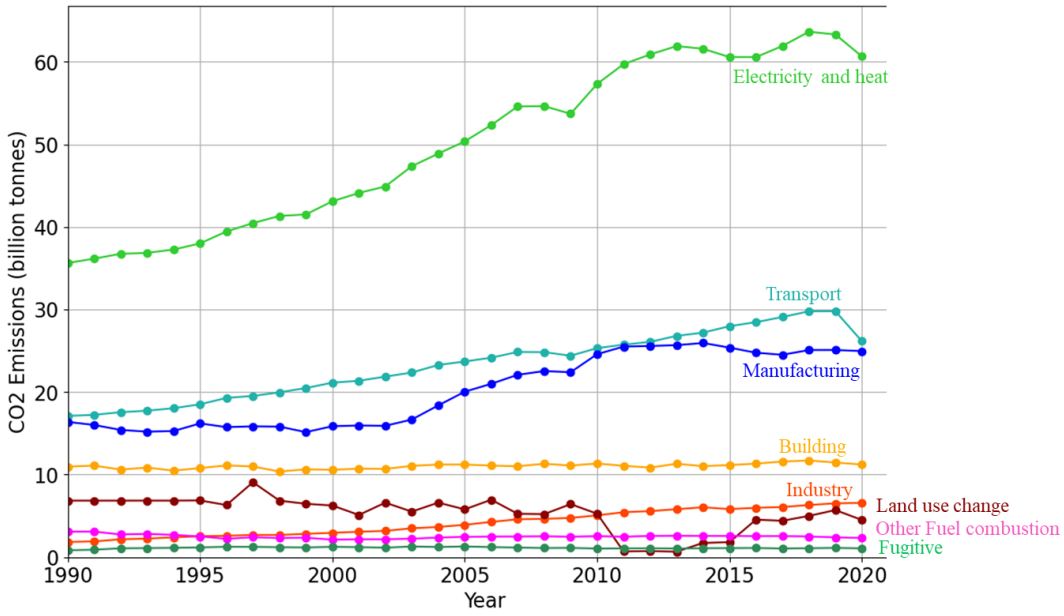


Figure 2.1 Graph of CO_2 emitted globally by each sector as reported by [12].

The transportation sector is responsible for more than a third of man-made greenhouse gas emissions [13]. There is a considerable need for lightweighting of automotive vehicles and transport systems to reduce further increase of CO_2 emissions. Different forms of materials are used in the industry. The pie chart in Figure 2.2 illustrates the distribution of various product forms by different manufacturing processes, segmented into five categories with corresponding percentages of the total manufacturing activities.

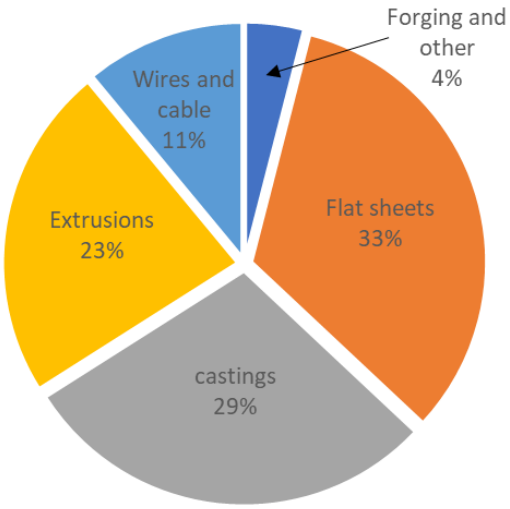


Figure 2.2 Distribution of manufacturing processes in the industry by weight, data sourced from [14].

As shown in Figure 2.2, the largest segment, representing 33% of the total by weight is dedicated to "Flat sheets". Flat sheets have wide application in numerous products and industries. This is followed closely by castings which account for 29% of the manufacturing, highlighting their importance in creating complex shapes essential for sectors such as automotive, aerospace and machinery. Extrusions account for 23%, where items of fixed cross-sectional profile like pipes, tubes and structural components are produced. Wires and cables make up 11% and forging and other processes account for 4%, which although they are not as prevalent as the other categories, remain vital for specific applications.

2.2.2 Structures

In real structures, multi material types are often employed. Figure 2.3 provides a detailed illustration of the structural composition of the Airbus A380, which is one of the largest aircrafts ever manufactured, highlighting the diverse materials used in various components of the aircraft. Figure 2.3 is critical for understanding the integration of advanced materials in modern aerospace engineering to enhance performance, reducing weight and improving overall efficiency.

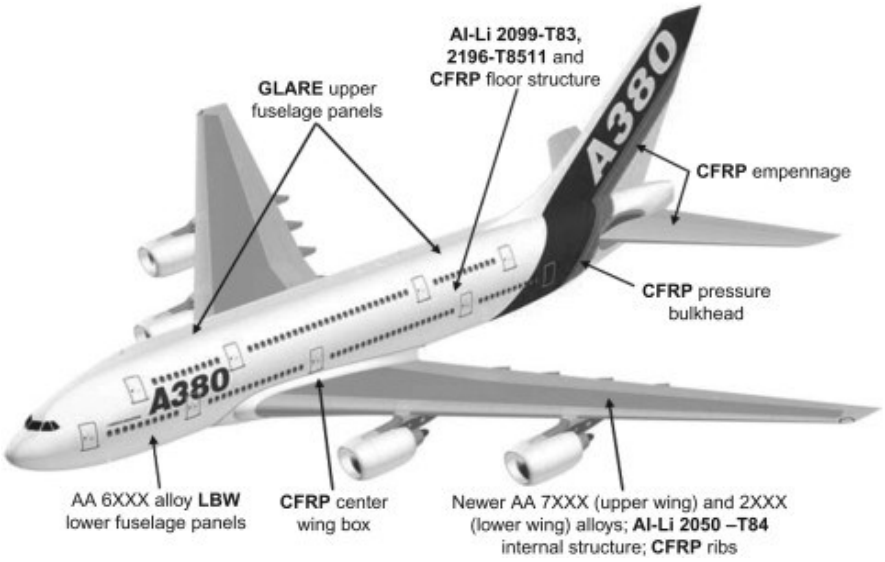


Figure 2.3 Structural composition of the Airbus A380 with key materials are identified [15].

Figure 2.3 identifies several key materials used within the aircraft structure. The upper fuselage panels are made from GLARE, a material known for its high fatigue, impact resistance and lightweight properties. This composite material combines aluminium and fiberglass layers to reduce the overall weight. Aluminium-lithium alloys Al-Li 2099-T83 and 2196-T8511, are chosen in the upper wing structures and certain floor structures, for their reduced weight and improved mechanical properties compared to traditional aluminium alloys. The extensive use of Carbon Fiber Reinforced Polymer (CFRP) in several different components is highlighted including the tail section, pressure bulkhead, centre wing box and ribs. CFRP is utilised because of its higher strength-to-weight ratio compared to metals hence reducing fuel consumption and excellent fatigue resistance increasing the life of the airframe [16]. Newer aluminium alloys, such as AA 7XXX (upper wing) and 2XXX (lower wing) alloys, as well as Al-Li 2050-T84 for internal structures, are used to further optimise the balance between strength and weight. The lower fuselage panels are constructed from AA 6XXX alloy using Laser Beam Welding (LBW) techniques, which create precise strong joints.

In relation to automotive structures, Figure 2.4 shows an automotive Body-In-White (BIW) with the critical structural elements for crashworthiness identified red. These structural elements are introduced to increase the safety of occupants during a collision and help provide a five stars safety rating by the European New Car Assessment Programme (Euro NCAP).

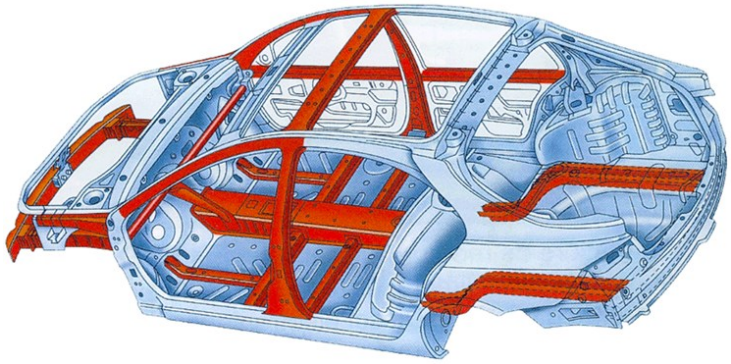


Figure 2.4 Metallic components of an automotive Body-In-White (BIW) – the critical components are highlighted red, in this case, are Martensitic Steel (MS) UHSS components e.g. front and rear bumpers, door frame, sill reinforcement and roll cage [17].

There is clearly much scope to reduce the use of steel in transport albeit a large proportion of the steel is being used in construction as well as transport and other sectors. As well as aluminium alloys being light, these alloys are also heat treatable to improve their strength and this is important as steel generally has a higher strength. For the BIW, shown in Figure 2.4, then, weight reductions of 50% have been achieved by the substitution of steel by aluminium alloy [18, 19]. An aluminium alloy also has the advantage of enhanced recyclability over steel. Steel once it loses its galvanic coating and surface paint protection can rust and steel, in an automotive structure, will have many different alloying elements which means separation and recycling becomes difficult. In terms of energy consumption, aluminium alloy is expensive to extract from its Bauxite ore. However, at the end of its life, an aluminium alloy component is cheaper to recycle as the melt temperature is lower. This is as long as the contamination issues with other alloys can be overcome. One of the shortcomings of aluminium alloy is its strength compared with steel but for some high-performance aluminium alloys, e.g. AA6082, strength is acceptable to meet crashworthiness and other considerations of automotive structures.

The obvious benefit from light-weighting vehicles is that it reduces emissions from internal combustion engines when accelerating these vehicles, ascending gradients and maintaining forward motion against air resistance. As we move to other forms of propulsion, e.g. electric vehicles or Hydrogen fuel-cells, the mass of the vehicle is clearly also important in reducing energy consumption. Many different materials have been explored including CFRP, Glass-Fibre Reinforced Polymers (GFRP), Ultra High Strength Steels (UHSS) as well as the lighter alloys e.g. aluminium and magnesium alloys. CFRP is a very expensive material to employ for automotive cars and only really finds application in F1 vehicles and very expensive sport cars.

GFRP is a cheaper raw material, but it is still difficult to manufacture quickly a car body [20]. UHSS is attractive as the automotive component can be made thinner and still achieve good crashworthiness [21]. Magnesium alloys are light but can lack ductility. The weight saving for different types of material in automotive structures is appreciable up to 40% with a potential fuel saving up to 20-30% [22].

2.2.3 Aluminium alloy

Aluminium is the second most used metal after steel with more aluminium being produced than all other nonferrous metals put together. Global demand for aluminium is substantial. According to the British Geological Survey in 2019, 3,040 million tonnes of Iron Ore were mined and 63 million tonnes of aluminium were mined [23]. Figure 2.5 presents the aluminium production from 2000 to 2024, measured in thousand metric tonnes (production up until August 2024). The bar chart separates the production of different regions around the world, illustrating trends and shifts in aluminium production over the decade.

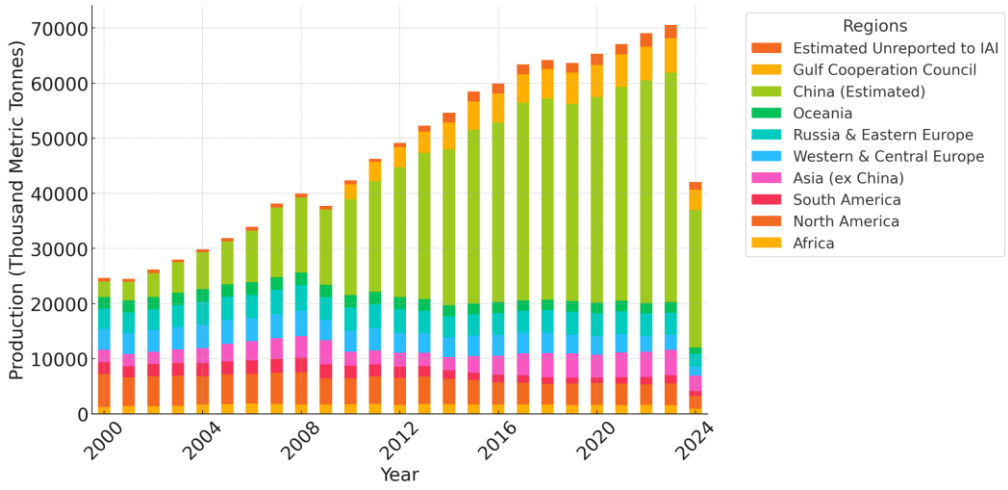


Figure 2.5 Global production of aluminium per year (2000-2024) data sourced from International Aluminium Institute [24].

Figure 2.5 shows a steady increase in global aluminium production over the decade, rising from just over 25,000 thousand metric tonnes in 2000 to an estimated over 70,000 thousand metric tonnes in 2024. Each bar represents the total production for a given year, split by region to highlight the contributions of different parts of the world to total production. China is the global leader in aluminium alloy production, where China's aluminium production shows a substantial increase over the years indicating expanding industrial capacity and growing demand for

aluminium. However, other regions such as North America and Europe show more constant production levels, indicating mature markets with steady demand. With the rest of production being made up from Africa, Asia, Oceania, and the Gulf Cooperation Council (GCC).

An aluminium alloy of particular interest is AA6082 which generally has very good characteristics due to its lightweight and high strength-to-weight ratio [2]. The alloy AA6082 is known for its excellent corrosion resistance, good weldability and high strength and is often used in aerospace components, automotive structures, and marine applications. AA6082 is well characterised in terms of its mechanical performance, including tensile and fatigue testing and this is crucial for assessing the alloy's structural integrity under different loading conditions.

2.2.4 Hot stamping and HFQ

Hot stamping is a metal forming process where high-strength steel blanks are heated and then formed in a press [25, 26]. The process allows shaping into complex forms that are difficult to achieve with cold forming because of the high strength and reduced ductility at low temperatures [27].

Hot stamping was patented and industrialised by a Swedish Company in 1977 for producing saw blades and lawn mower blades from a steel which had Boron added to provide for high quenchability [28]. Subsequently, it was found that the technology could be applied to press hardening of intrusion door frames. This was employed by Saab Automobile AB for the Saab 900 in 1984 [29]. Since then, many automotive manufacturers employ this technology to provide components with excellent strength and crashworthiness.

Figure 2.6 illustrates the hot stamping process [30]. The steel sample is heated initially up to 950 ^{o}C, where Austenite forms replacing the Ferrite-Perlite microstructure. After transfer into the die, the component is then formed and quenched resulting in formation of the hard brittle phase of Martensite [31]. Martensite is a distorted body centred cubic structure with carbon locked into the structure. This is sometimes called body centred tetragonal as one of the dimensions of the body centred cubic unit cell is longer than the other two dimensions due to the interstitial carbon distorting the structure. Subsequent heat treatment, at modest temperatures (350-550 ^{o}C), can allow the carbon to diffuse and form precipitates of Cementite which relieves the stress, increasing the ductility but still maintaining strength [32]. The exact

form of the heating and cooling profile, die temperature, metallic sheet temperature and forming tool shape and speed are very important parameters which affect the microstructure and materials properties of the final component [33].

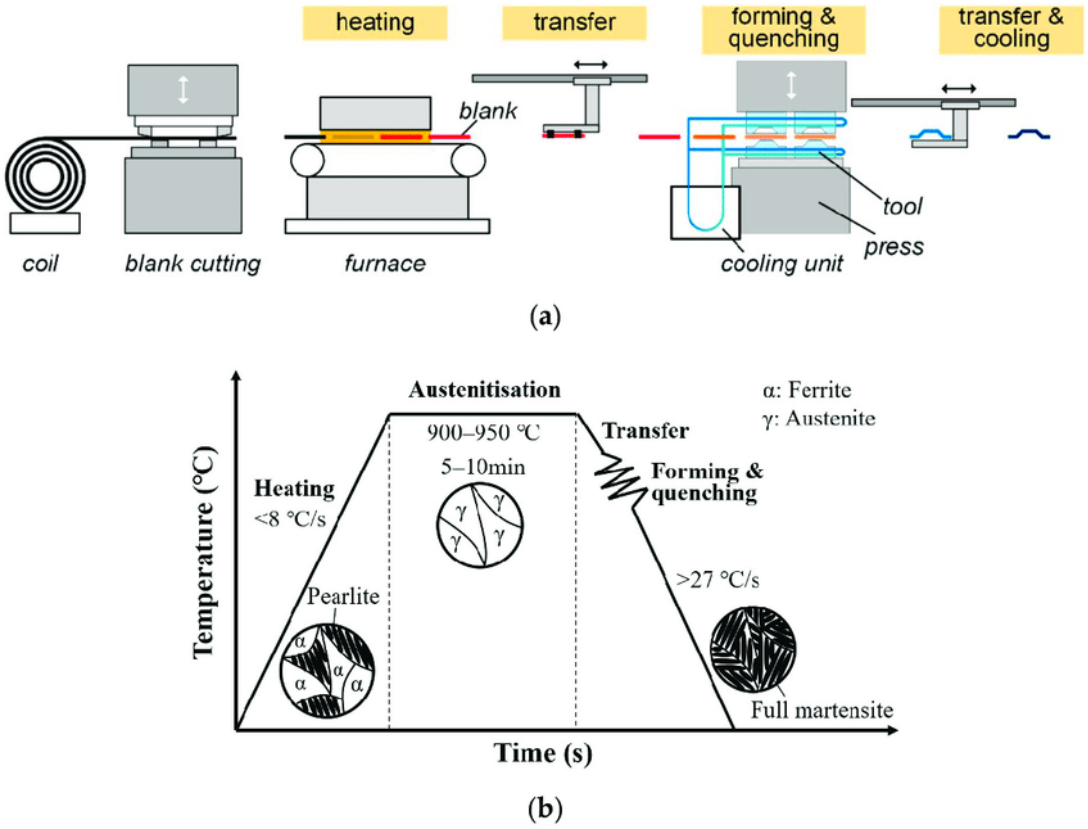


Figure 2.6 Hot stamping of a steel component, showing heating, forming and quenching process leading to a component with full martensitic formation in the steel which has high strength. Martensite is a lens-like formation of BCC steel distorted by carbon which is locked into its structure and as such is very hard and strong but can be brittle unless heat treated: (a) manufacturing process; (b) temperature profile [30].

Aluminium alloys exhibit challenges with regards to formability and there can also be significant spring-back after the forming process. To overcome the problems, a process of solution heat treatment, forming and in-die quenching (HFQ), which is also called Hot Form Quench, was developed and patented [34]. HFQ is an integrated process for stamping of heat-treatable, high strength aluminium alloys [32]. This process is illustrated in Figure 2.7. It involves solution heat treatment (SHT) of the aluminium blanks, rapid forming in the die, and quenching to achieve a Super Saturated Solid Solution (SSSS) microstructure. Subsequently, artificial ageing is performed to improve the strength of the formed alloy [33]. During artificial ageing, a fine distribution of precipitates is generated which resist dislocation motion and give

high strength to the formed alloy [33]. A distinct advantage of this HFQ technique is that complex shapes can be formed and there is minimal distortion and spring-back after forming. Also, the forming and heat treatment takes place in a continuous process and as such is of lower cost, particularly for heat treatable aluminium alloys.

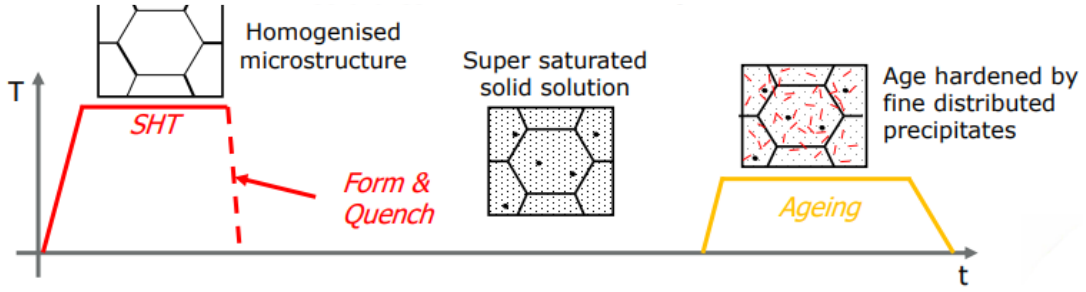


Figure 2.7 Stages of the HFQ process [35].

It is important to consider the phase diagram when determining heat treatments albeit the phase diagram is for equilibrium conditions which do not always reflect what can occur if cooling and heating processes are quick. Figure 2.8 shows the phase diagram for the aluminium magnesium silicon alloy AA6082. The vertical dashed line shows the effect of heat treating an alloy of 1.6 wt% Mg_2Si in aluminium. The top X, on the dashed vertical line, corresponds to a temperature of approximately 550 ^oC when the Mg_2Si precipitates will dissolve in aluminium to form a solid solution, labelled α, on the phase diagram. If the solid solution of 1.6 wt% Mg_2Si in aluminium is cooled by quenching down to the lowest X along the dashed line, a supersaturated solid solution would arise with no precipitation. However, if the temperature is subsequently raised to the middle X, then, at this heat treatment temperature, of approximately 250 ^oC, some precipitates of Mg_2Si would start to form in the aluminium structure. The precise heat treatment temperature chosen controls the size and distribution of Mg_2Sn precipitates. Ideally, a fine and well dispersed array of precipitates is best to impede dislocation and add strength to the alloy.

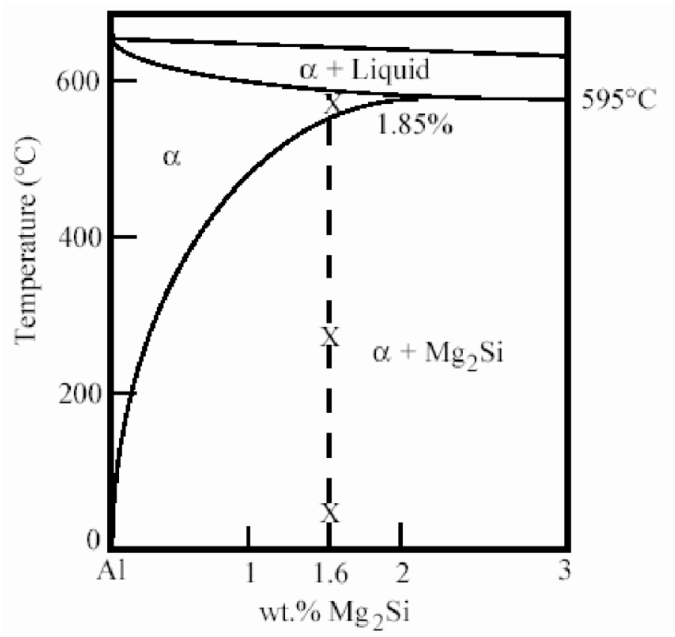


Figure 2.8 Phase diagram for an aluminium alloy AA6082 showing the different phases present for this aluminium, magnesium, silicon alloy. This is with labels X showing key temperatures for a 1.6 wt. % Mg_2Si in aluminium alloy, top X is solid solution temperature, middle X is heat treatment temperature and lower X is temperature to which alloy is quenched [36].

Understanding the formability of a sheet metal is crucial to success when employing techniques like HFQ to form a product. Figure 2.9 shows a schematic of a Forming Limit Diagram (FLD) showing the Forming Limit Curve (FLC) which identifies the onset of localised necking that leads to failure. When a material is formed, there are strains in different directions. If a material is under uniaxial tension, there will be a major strain which is positive in the direction of tension and a minor strain in the other two orthogonal directions which will be negative associated with Poisson's contraction. For a state of plane strain, one of the orthogonal strains is zero and for biaxial tension two of the orthogonal strains are positive. If the principal major (maximum) strain is plotted against the principal minor (minimum) strain, then a Forming Limit Diagram (FLD) can be defined on which there will be a locus or Forming Limit Curve (FLC). The FLC identifies the onset of localised necking which of course will lead ultimately to failure [37]. Typically, the FLC, for a given temperature of forming, will pass from uniaxial through plane strain and then onto to the biaxial tension condition. Higher FLC indicated better formability and generally, the FLC will move upwards as the temperature is increased or the forming speed is decreased.

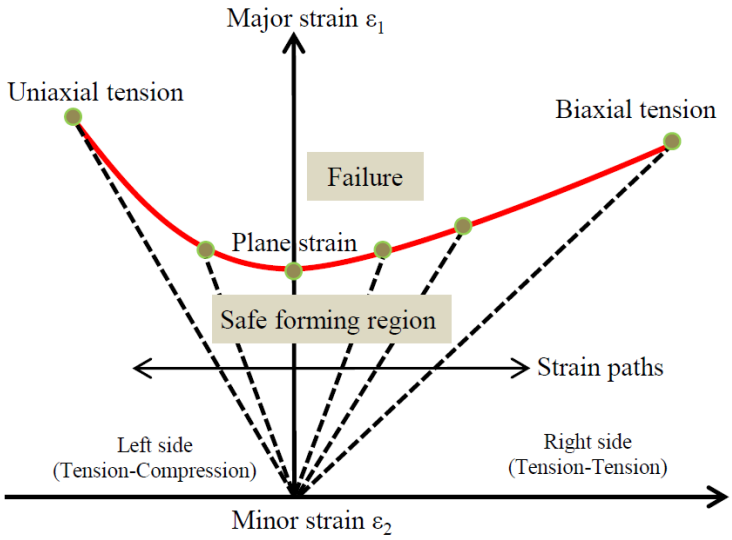


Figure 2.9 Schematic of Forming Limit Diagram (FLD) showing the Forming Limit Curve (FLC) which identifies the onset of localised necking leading to failure [38].

2.3 Machine Learning

Basic principles of machine learning are introduced in this section. The goal of machine learning is building computer programs that can automatically improve themselves in performing certain tasks from experience data [39]. The essence of the (supervised) machine learning algorithms is to learn a function $f : X \rightarrow Y$, where X is the training data, and Y is corresponding output. In Figure 2.10, this principle is illustrated.

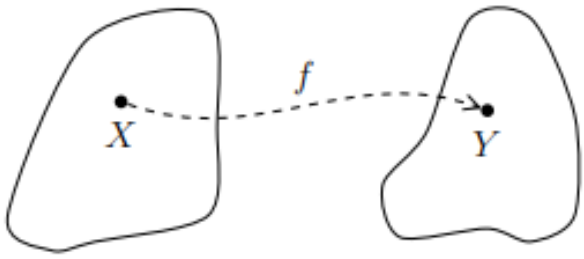


Figure 2.10 Schematic illustration of machine learning model.

Machine Learning (ML) is a subset of artificial intelligence focused on enabling computers to learn from data without explicit programming. Early methods were based on traditional statistical methods like linear regression and decision trees, and these laid the foundation for predictive modelling based on statistical analysis. Support Vector Machines (SVMs) became popular in the 1990s for effective classification tasks, by finding optimal hyperplanes in the feature space. These advances are driven by the availability of easy-to-use packages for building machine learning models, e.g. Scikit-Learn [40] and Keras [41]. Figure 2.11 shows

the progress in performance of AI models across different tasks from 2012 to 2023, with performance measured as a percentage of the human baseline set at 100%. The tasks, assisted by AI, include image classification (green), visual reasoning (blue), medium-level reading comprehension (red), visual commonsense reasoning (light blue), multitask language understanding (orange) and competition-level mathematics (purple).

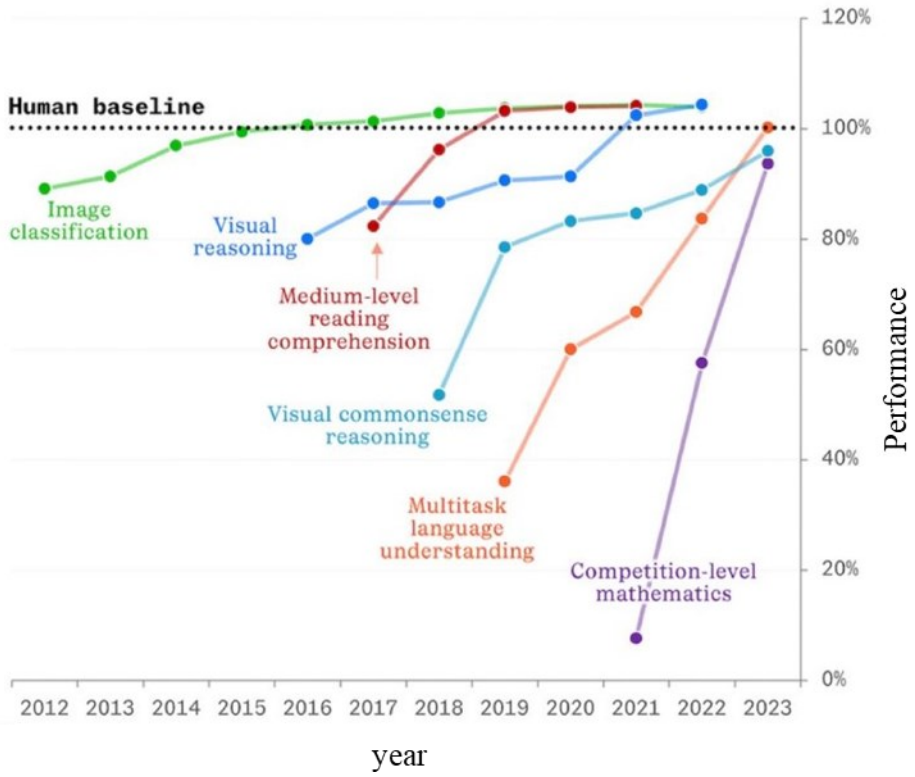


Figure 2.11 AI models are improving every year [42].

Figure 2.11 demonstrates that AI models are becoming more powerful every year and have reached or even surpassed human baseline intelligence in image clarification, visual reasoning, reading comprehension and multitask language understanding.

Machine learning has started to change the way that we do materials research, contributing to accelerated characterisation, synthesis and modelling. Figure 2.12 shows the number of publications each year, in the field of machine learning and machine learning within material science. As shown in Figure 2.12, over 90,000 papers were published in 2023. The number of papers published in machine learning has increased every year. In particular, the use of machine learning in material sciences has also seen a rapid acceleration in the last decade.

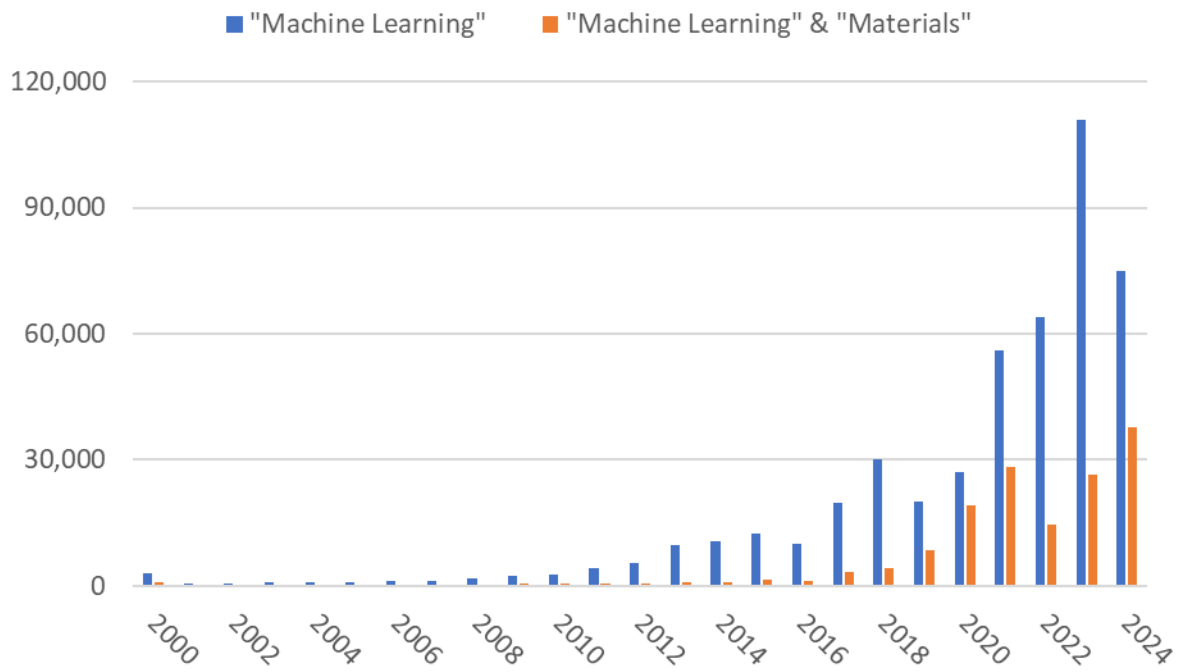


Figure 2.12 The growth of ML - The number of published papers containing the terms “Machine Learning” and “Materials” via the Google Scholar search engine [43].

2.3.1 Artificial Neural Networks (ANNs)

Neural Networks or Artificial Neural Networks (ANNs) are intelligent information treatment systems which can establish complex non-linear relationships through the application of many non-linear processing units called neurons. ANNs can include various architectures such as feedforward networks, recurrent networks and convolutional networks. Usually, the structure of an ANN is hierarchical with neurons grouped in different layers designed as an input layer, hidden layers and an output layer. Each neuron in a neural network computes an output value by applying a specific function to the input values received from the previous layer. This means that input values passed to the neurons of the input layer which are transferred to the neurons of the hidden layer until the output data are generated by the last layer (output layer). In each neuron, an activation function is applied to the input values as determined by a vector of weights and biases. The general structure of an ANN is shown in Figure 2.13.

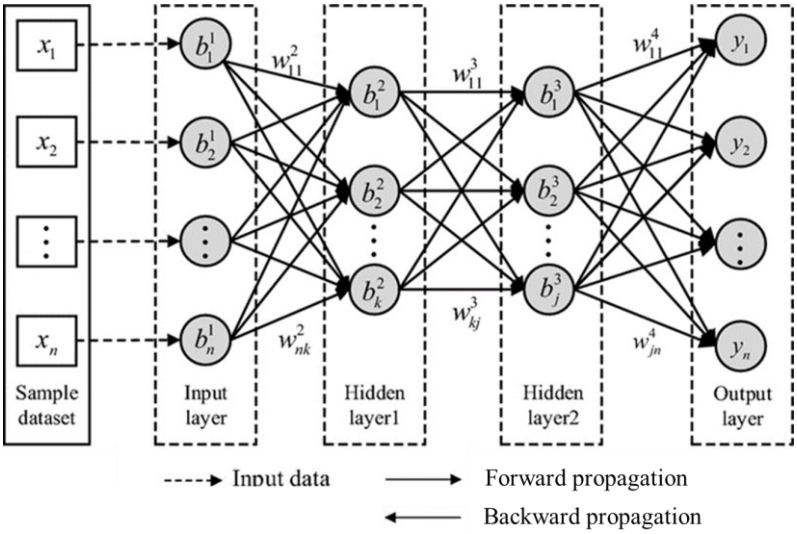


Figure 2.13 Layered structure of an Artificial Neural Network [44].

In Figure 2.13, the input layer consists of I neurons, each receiving an input of x_1, x_2, …, x_n. The hidden layer contains k neurons, each of which performs computations on the input data. The figure shows a single hidden layer, but in practice, there can be more than one hidden layer. The connections between the previous layer and current layer depend on the weights w_{ij}. This is where the weights are adjusted during training. For each hidden layer neuron, y_i is determined by a weighted sum of inputs, processed through an activation function, which is passed to the next layer. The output layer consists of n neurons, each producing an output of z_1, z_2, …, z_n. Forward propagation is where data travels from input to output and each layer processes the data and passes the results forward. Backward propagation indicated by the bottom arrow is the process of adjusting the weights to minimise the loss. During training the biases and weights are iteratively adjusted using backpropagation so that the difference between the predicted output and the actual target values or loss function in a given dataset is minimised. This method allows the network to be generalised to cope with unseen data. In summary, machine learning models often rely on a single hidden layer within their architectures [45]. In contrast, deep learning employs neural networks with multiple hidden layers in their architecture [46].

2.3.2 Recurrent Neural Networks (RNNs)

Recurrent Neural Networks (RNNs) were subsequently introduced to address the limitations of the traditional feed forward ANNs by incorporating memory for sequence data tasks as shown in Figure 2.14.

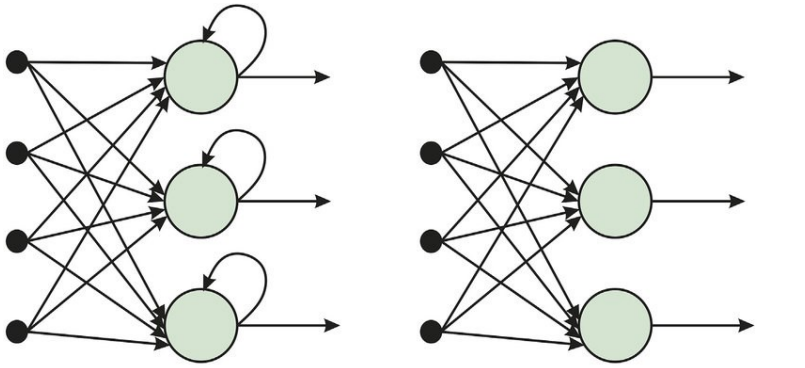


Figure 2.14 Neural network designs: (a) Recurrent Neural Network (b) Feed-Forward Neural Network.

As shown in Figure 2.14, RNNs differ from traditional Feed-Forward Neural Networks by introducing a way to maintain a memory across inputs, allowing them to better process sequential data such as text, speech or time series data. RNNs are a type of neural network that is designed for processing sequential data. It is based on calculation of the hidden state h_i which is based on the previous hidden state h_{i-1} and the current input x_i, with an activation function σ like the hyperbolic tangent or Rectified Liner Unit (ReLU) functions. At every timestep, the output is calculated from the hidden state h_i. In full, these equations are expressed as:

$$h_i = \sigma(W_h[h_{i-1}, x_i] + b_h) \tag{2.1}$$

$$y_i = \tanh(W_y \cdot h_i + b_y) \tag{2.2}$$

where $[h_{i-1}, x_i]$ denotes concatenation of the previous hidden state and the current input, W_h and W_y are the weights, and b_h and b_y are the biases. The RNN cell applied in each neuron of the layer is illustrated in Figure 2.15 which shows the flow of data or information.

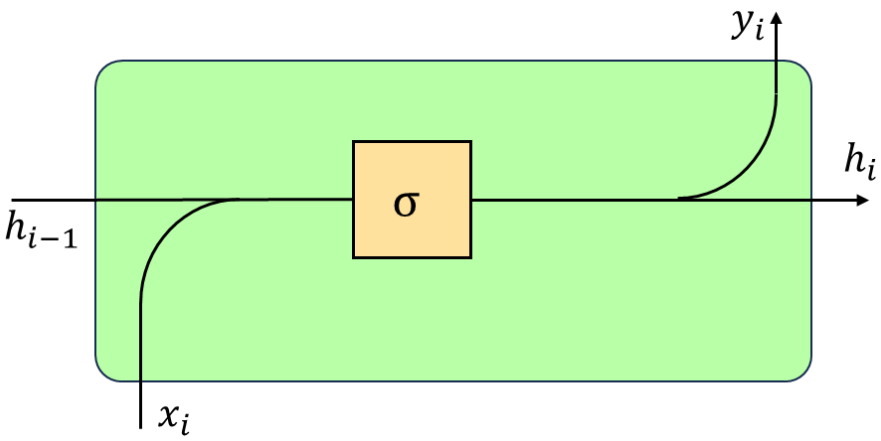


Figure 2.15 Schematic of the neural network architecture of an RNN.

2.3.3 Gated Recurrent Unit (GRU)

The Gated Recurrent Unit (GRU) is an evolution of the basic RNN. GRUs introduce update and reset gates that control how much past information is forgotten and how much new information is added. This gating mechanism allows GRUs to keep relevant information throughout the sequence and disregard irrelevant data, helping to mitigate the vanishing gradient problem common with RNNs and long sequences. The update gates z_i and forgot gates r_i are determined from the previous hidden state h_{i-1} and the current input x_i, with an activation function σ. The candidate hidden state $\tilde{h}_i$ is determined from the forgot gates r_i and previous hidden state h_{i-1}. The final hidden state is calculated from the update gates z_i, previous hidden state h_{i-1} and candidate hidden state $\tilde{h}_i$. The equations for a GRU are outlined in full as:

$$z_i = \sigma(W_z[x_i, h_{i-1}] + b_z) \tag{2.3}$$

$$r_i = \sigma(W_r[x_i, h_{i-1}] + b_r) \tag{2.4}$$

$$\tilde{h}_i = \tanh(W_r[x_i, r_i \odot h_{i-1}] + b_h) \tag{2.5}$$

$$h_i = (1 - z_i) \odot h_{i-1} + z_i * \tilde{h}_i \tag{2.6}$$

where $\odot$ is the Hadamard product meaning element-wise product, W_z, W_r and W_h are the weights and b_z, b_r and b_h are the biases of each respective gate. A schematic of the GRU cell in Figure 2.16 shows the slightly more complex flow of data and information.

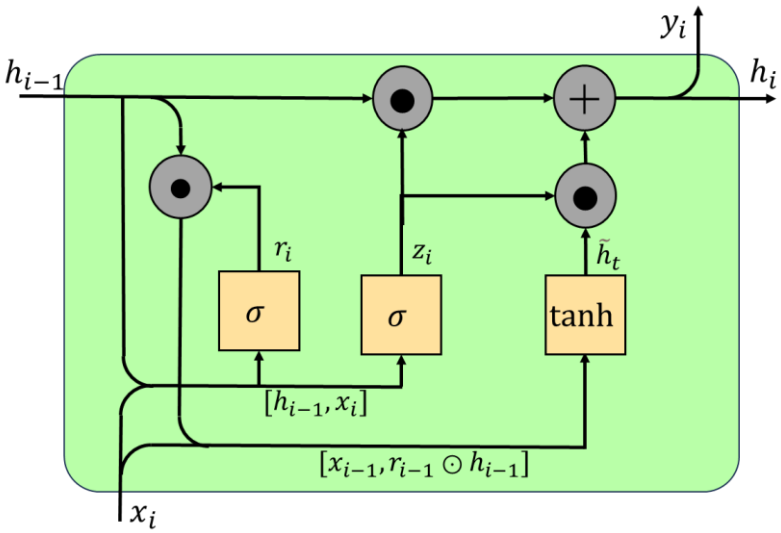


Figure 2.16 Schematic of the neural network architecture of a GRU.

As shown in Figure 2.16, the GRU consists of several key components: the update gates z_i and forgot gates r_i, the candidate hidden state $\tilde{h}_i$. The final hidden state is calculated from the update gates z_i, previous hidden state h_{i-1} and candidate hidden state $\tilde{h}_i$.

2.3.4 Long Short-Term Memory (LSTM)

Long Short-Term Memory (LSTM) [47] is an artificial neural network used in the fields of artificial intelligence and deep learning. Unlike standard feedforward neural networks used in RNN and GRU [48], LSTM neural networks have feedback connections. This characteristic makes LSTMs networks better suited for long-term prediction of data compared to RNNs and other feed forwards methods.

Figure 2.17 shows an overall schematic of the LSTM neural network which is considered to give a very effective analysis approach. The circle with internal dot symbol represents the Hadamard product, and the circle with internal plus symbol represents element-wise addition.

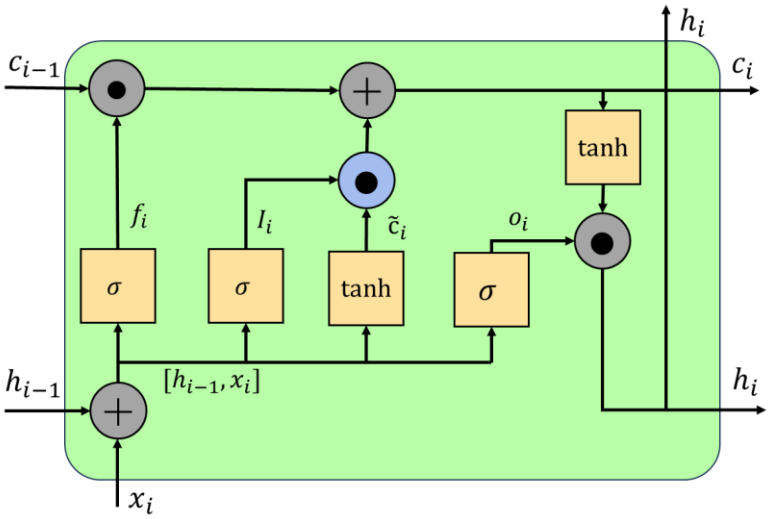


Figure 2.17 The schematic structure of the LSTM cell.

The forgot state f_i, input state I_i, output state o_i, and cell input activation $\tilde{c}_i$ are calculated from the previous hidden state h_{i-1} and the current input x_i. The cell state c_i is calculated from the forgot state f_i, pervious cell state is c_{i-1}, input state I_i and cell input activation $\tilde{c}_i$. From the output state and cell state, the final hidden state h_i is calculated. The equations for a LSTM cell can be summarised as:

$$f_i = \sigma(w_f[x_i, h_{i-1}] + b_f) \tag{2.7}$$

$$I_i = \sigma(w_I[x_i, h_{i-1}] + b_I) \tag{2.8}$$

$$o_i = \sigma(w_o[x_i, h_{i-1}] + b_o) \tag{2.9}$$

$$\tilde{c}_i = \sigma(w_c[x_i, h_{i-1}] + b_c) \tag{2.10}$$

$$c_i = f_i \odot c_{i-1} + I_i \odot f_i \tag{2.11}$$

$$h_i = o_i \odot \tanh(c_i) \tag{2.12}$$

where $[x_i, h_{i-1}]$ denotes concatenation of the current input and the previous hidden state, x_i, h_{i-1}. σ and tanh are activation functions and $\odot$ is the Hadamard product denoting the Hadamard product or piece-wise element product. The biases are given by $b = \{b_a, b_f, b_c, b_o\}$ which are the biases of input gate, forgot gate, internal state and output gate. The weights given

by $\overrightarrow{W_1} = \{w_a, w_f, w_c, w_o\}$ are weight matrices of the input gate, forgot get, internal state and output gate.

In Table 2.1, the advantages and disadvantages of different neural networks are outlined, including those for ANN, RNN, GRU and LSTM. Considering these, LSTM is selected for the current work.

Table 2.1 Advantages and disadvantages of different Neural Networks.

	Advantages	Disadvantages
ANN	• simplest to implement.	• Poor performance with long sequential data.
RNN	• Able to model sequential data [49]. • Compact architecture.	• Suffers from vanishing/exploding gradient with long sequences. • Hard to capture long term strain rate and temperature trends.
GRU	• Simpler and faster than LSTM. • Effective for capturing short-term relationships between temperature, strain rate, and strain field.	• More computationally expensive than simple RNN.
LSTM	• Solves vanishing gradient problem effectively with gated mechanisms. • Learns which data to retain or disregard giving better discovery of the long-term trends [50].	• Complex architecture with more parameters than GRU, leading to slower training and higher computational cost compared to RNNs or GRUs.

2.3.5 Adams optimiser

In deep learning, optimisation algorithms help the neural network converge effectively to the optimal solution. The Adaptive Moment Estimation ADAM solver remains the most used method. The Adam solver uses combination of root mean square propagation and stochastic

gradient descent with momentum [51, 52] to find the global minimum of the loss. Firstly, m_n & v_n are the aggregate of gradients at the n^{th} iteration and are given respectively by:

$$m_n = \beta_1 m_{n-1} - (1-\beta_1)[\frac{\delta L}{\delta w_n}] \tag{2.13}$$

$$v_n = \beta_2 v_{n-1} - (1-\beta_2)[\frac{\delta L}{\delta w_n}]^2 \tag{2.14}$$

where $\frac{\delta L}{\delta w_n}$ is the derivative of loss function with respect to the weights, β_1 & β_2 are parameters taken as 0.9 and 0.999 respectively. The aggregates m_n and v_n are normalised using the following equations:

$$\hat{m}_n = \frac{m_n}{1-{\beta_1}^n} \tag{2.15}$$

$$\hat{v}_n = \frac{v_n}{1-{\beta_2}^n} \tag{2.16}$$

This is accomplished by updating the weights of the neutral network given in the neural network using the following:

$$w_n = w_{n-1} - \eta \frac{\hat{m}_n}{\sqrt{\hat{v}_n}+\epsilon} \tag{2.17}$$

where w_n is the weights of the model at the nth iteration, η is the learning rate, and $\epsilon = 10^{-8}$ is a constant that avoids division by zero. The Adam solver has been shown to not converge for all convex objective functions. Despite this shortcoming, it continues to be used in practice due to its strong performance in practice [52].

2.3.6 Effect of hyperparameters

Hyperparameters are configuration parameters used to control the behaviour of machine learning models and optimisation algorithms during the training process. These include the number of neurons in each layer, learning rate, sequence length and choice of activation function. These parameters must be defined beforehand and can significantly affect the model performance during training. Poorly chosen parameters can lead underfitting, overfitting or failure to converge. The number neurons in each layer affect the complexity of the model. These choices are very important and affect the ability to capture patterns in the data.

The learning rate is an important hyperparameter which affects how much the loss needs to be reduced per Epoch using the Adams optimiser. As a typical guide a comparison of the effects of different learning rates are illustrated in Figure 2.18. As illustrated in Figure 2.18, there is an optimum learning rate to avoid underfitting and overfitting these data, which reduces the loss steadily. The number of epochs is another important hyperparameter, too few or too many epochs can lead to overfitting or underfitting during training

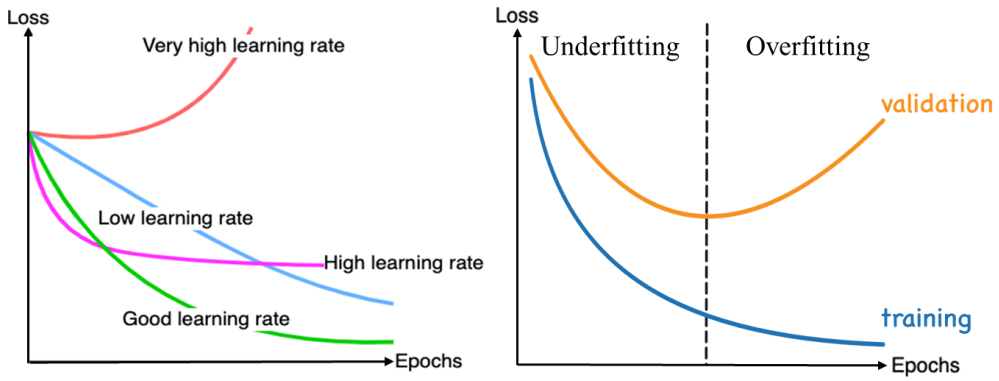


Figure 2.18 Learning rate and overfitting: (a) The effect of learning rate on the loss during training and (b) the effect of overfitting on the training and validation loss [53].

A learning rate which is too low leads to very slow convergence whilst a learning rate which is too high can lead to unstable behaviour where the weightings of the model during training are updated too dramatic, leading to unstable behaviour.

2.4 Machine Learning Applications in Materials Testing and Modelling

Machine Learning has emerged as a promising method for the analysis of experimental data, offering a more time-efficient alternative to Finite Element (FE) and other numerical techniques [54]. When equipped with accurate and extensive datasets, a data-driven ML approach can surpass traditional approaches in efficiency [55]. This is partly due to the advanced learning algorithms, such as the Adams solver, which iteratively optimise models to enhance performance [52]. More and more studies are emerging in the application of ML in materials science and engineering. A remarkable promise has been shown using ML as a method for predicting the cyclic stress-strain properties of ferrite-pearlite steels by combining synthetic microstructure generation, calibrated through low-cycle fatigue experiments, with finite element simulations [56]. Multi-layer neural networks have been used to predict mechanical properties such as the Ultimate Tensile Strength (UTS) for different alloy

compositions [57]. By incorporating both chemical compositions and specific manufacturing steps as features, a Support Vector Regressor (SVR) model was used to predict the mechanical properties of wrought aluminium alloys [58]. Machine learning has been used to efficiently predict microscale elastic strain fields within 3D microstructures of composite materials [59]. A deep learning-based algorithm was used to predict the local strain fields in a two-phase composite material subjected to uniaxial tensile load [60].

ANN models have been successfully used to predict the hot working behaviour of materials. In the study [61], the high-temperature deformation characteristics of an Fe-Ni-Co-Al-Ta-B shape memory alloy were investigated through compression testing across a wide range of temperatures (1323–1473 K) and strain rates (0.01–10 /s). Model performance was evaluated using correlation coefficient and relative percentage error metrics. Notably, the ANN model outperformed both Arrhenius-type models in efficiency and accuracy for predicting the high-temperature flow behaviour of the shape memory alloy.

As another example of applying machine learning to generate quality data and model material properties, the research in Reference [62] characterised the material properties based on microstructure. This research innovates by integrating a CNN with a novel microstructure-factored constitutive model, separating the microstructure's influence from material constituents. The CNN, trained on a single set of material constituents at a specific temperature, achieved impressive generalisability, accurately predicting the properties of various materials at different temperatures with a low mean absolute percentage error of about 3%. This illustrates the CNN architecture tailored for this task, highlighting the effective learning and prediction of stress-strain responses, a crucial aspect for advancements in materials modelling within the scope of machine learning applications.

Traditional machine learning approaches require extensive data to capture these complex characteristics, demanding substantial computational effort. Therefore, the key processes in the development of Machine Learning models for metal forming applications are acquiring high quality extensive datasets and choosing the most appropriate neural networks (e.g. RNNs, LSTM, and GRU).

2.5 Unified constitutive equations

Many unified constitutive equations are models designed to describe the complex behaviour of materials under different loading conditions and can consider the effects of strain, strain rate and temperature into a cohesive framework. These equations unify the modelling of material behaviour across different regions of deformation (e.g. elastic, plastic, and creep) within a single framework, describing the constitutive relationship evolving with microstructural evolution. Unlike traditional models, which often separate these phases, unified constitutive equations integrate them into one combined model, allowing for a more accurate and continuous prediction of material behaviour over a wider range of conditions. They have been developed for many different applications, to model the high-temperature creep in metals [63], plasticity in metal forming [64] and cyclic loading of structural components [56].

Broadly, constitutive equations can be categorised into function based unified constitutive equations and Ordinary Differential Equation (ODE)-type unified constitutive equations. The general form of a function based unified constitutive equation can be expressed as:

$$\sigma = \mathrm{f}(\varepsilon, \dot{\varepsilon}, T) \tag{2.18}$$

where σ is the flow stress, $\dot{\varepsilon}$ is the strain rate and T is temperature. These equations include the power law relationships including Norton-Hoff (N-H) viscoplastic [6, 65]. and Johnson-Cook (J-C) constitutive equations [66]. The function based unified constitutive equations have been widely used and are still being employed.

2.5.1 Holloman power law

The 'power law' relationship for plastic deformation was first introduced to model plasticity of metals, where the true stress typically increases with increasing plastic strain due to strain hardening. The conventional power law relationship for strain hardening is given by [67] :

$$\sigma = K \cdot \varepsilon^{n} \tag{2.19}$$

where σ is the true stress, K is the strength coefficient, ε is the plastic strain and n is the strain hardening exponent typically taken between $0 < n < 1$. However, the Holloman power law does not consider the effects of temperature and can only strictly be used at room temperature [68].

2.5.2 Norton-Hoff model

The Norton-Hoff (N-H) model [69] is a non-linear thermo-viscoplastic equation, proposed to model the flow stress under different deformation temperature and strain rates. This is given as [65] :

$$\sigma(\varepsilon, \dot{\varepsilon}, T) = K \cdot \exp(\beta/T) \cdot \varepsilon^n \cdot \dot{\varepsilon}^m \tag{2.20}$$

where σ is true stress, K is a constant, β is a thermal activation energy dependent material coefficient, T is the absolute temperature, ε is strain, n is strain hardening exponent, $\dot{\varepsilon}$ is the strain rate and m is the strain rate sensitivity index. n and m are temperature dependent and can be described by the following [70]:

$$n(T) = n_0 \cdot \exp(-c_n \cdot (T - T_0)) \tag{2.21}$$

$$m(T) = m_0 \cdot \exp(c_m \cdot (T - T_0)) \tag{2.22}$$

The N-H model was successfully applied to tensile tests of boron steel under hot conditons under wide range of deformation conditions and its parameters were determined by appropriately calibrating against experimental data [6].

2.5.3 Johnson-Cook model

The Johnson-Cook (J-C) model [66] was developed to model the behaviour of metal under different strain, strain rates and temperatures. The model is particularly well-known in simulations involving high strain rates such as in impact and penetration scenarios. The Johnson-Cook model is expressed as a unified constitutive equation that captures the combined effects of strain hardening, strain rate sensitivity and thermal softening on the flow stress of a material as [71]:

$$\sigma = [A + B\varepsilon^n][1 - T^*]^m[1 + C\ln(\frac{\dot{\varepsilon}}{\dot{\varepsilon}_0})] \tag{2.23}$$

where σ is the equivalent flow stress, ε is the equivalent plastic strain, $\dot{\varepsilon}$ is the plastic strain rate and T^* is the homologous temperature. The key defining material parameters are: A is the yield stress, B is the hardening modulus, n strain hardening exponent, m thermal softening

exponent, C is strain rate sensitivity coefficient and $\dot{\varepsilon}_0$ is the lower reference strain rate. The homologous temperature T^* is given by:

$$T^* = \frac{T - T_0}{T_{max} - T_0} \tag{2.24}$$

T is the deformation temperature, T_0 is a reference temperature and T_m is the reference melting temperature. These parameters A, B, n, m, T_0, T_m, C and $\dot{\varepsilon}_0$ are adjustable and need to be fitted to the experimental stress strain behaviour of the material. The Johnson-Cook model was used to accurately model the behaviour of T24 steel under the temperatures of 1323–1473 K and strain rates of 0.01 to 10 /s for isothermal tests.

2.5.4 ODE-type unified constitutive equations

Over the past few decades, more complex physically based models for metal forming have been developed. These models consider the dominant deformation mechanisms [72] and incorporate both macroscopic and microscopic phenomena involved in plastic deformation. A generalised equation set was outlined in [73], allowing consideration of a wide range of microstructural factors. ODE based unified constitutive equations can represent physically based rate-dependent unified constitutive models and can be mathematically expressed as:

$$\dot{\boldsymbol{y}} = \mathbf{f}(\boldsymbol{p}, \boldsymbol{y}, \dot{\boldsymbol{y}}) \quad (t_0 \leq t \leq t_\mathrm{f}) \tag{2.25}$$

where $\boldsymbol{y}$ is a vector of the state variables $\boldsymbol{y} = [\mathrm{y}_1, .., \mathrm{y}_{NE}]^\mathrm{T}$ (*NE* is the number of state variables), $\dot{\boldsymbol{y}}$ denotes the corresponding time derivative and $\boldsymbol{p}$ represents the independent parameters within the model, such as the temperature and strain rate. Changes in the state variables occur over time t, where t_0 is the initial time, and t_f is the final time. Consequently, the added dependence of the derivative $\dot{\boldsymbol{y}}$ in Equation (1) indicates that each derivative is not necessarily only expressible in terms of the state variables [74]. Therefore, the following formulation was adopted, given in the following component form below:

$$\begin{pmatrix} \dot{\mathrm{y}}_1 \\ \vdots \\ \dot{\mathrm{y}}_i \\ \vdots \\ \dot{\mathrm{y}}_{NE} \end{pmatrix} = \begin{pmatrix} \mathrm{f}_1(\mathrm{y}_1, .., \mathrm{y}_{NE}, \boldsymbol{p}, \dot{\mathrm{y}}_2, .., \dot{\mathrm{y}}_{NE}) \\ \vdots \\ \mathrm{f}_i(\mathrm{y}_1, .., \mathrm{y}_{NE}, \boldsymbol{p}, \dot{\mathrm{y}}_1, .., \dot{\mathrm{y}}_{i-1}, \dot{\mathrm{y}}_{i+1}, .., \dot{\mathrm{y}}_{NE}) \\ \vdots \\ \mathrm{f}_{NE}(\mathrm{y}_1, .., \mathrm{y}_{NE}, \boldsymbol{p}, \dot{\mathrm{y}}_1, .., \dot{\mathrm{y}}_{NE-1}) \end{pmatrix} \quad (t_0 \leq t \leq t_\mathrm{f}) \tag{2.26}$$

where y_i and $\dot{y}_i$ for $1 \leq i \leq NE$ represent the state-variables and their derivatives, respectively, in a set of unified constitutive equations. This formulation ensures that the system can be treated as an ODEs, where a variety of numerical methods for ODEs are available [75-77]. This provides a modelling framework to enable researchers to consider any variables in accordance with their research focus, which can include physical state variables, such as dislocation density and grain size. Many researchers [63, 78-80] have developed increasing complex ODE-type approach to model different material behaviour. These ODE-type models are often the more physically based, as they incorporate the generation and movement of dislocation and associated work hardening effect from dislocation pile-up, cross-slip and related effects. Also, these models consider grain size and grain boundary effects as well as vacancy migration at elevated temperatures. Many material constants are included within unified constitutive equations, facilitating the modelling of a wide range of material simulations and phenomena. Moreover, these material constants can vary by several orders of magnitude and have different units [81].

In metal forming, high added-value metal-formed components are required to be manufactured with known microstructure and mechanical property often optimised via materials and process modelling [72]. The use of mechanism-based unified viscoplastic constitutive equations enables the complex dynamic interaction between microstructure evolution and viscoplastic deformation in the thermal mechanical processing of metal alloys to be modelled [82, 83]. Significant efforts have been made over the last few decades to understand microstructural evolution under warm/hot metal forming conditions [84]. A number of sets of unified constitutive relationships or equations have been developed for different metal alloys, such as titanium alloys [84], aluminium alloys [85] and ultra-high-strength steels [81, 86] and for different forming applications such as hot rolling [87], hot stamping [88] and extrusion [89].

2.5.5 Unified constitutive equations for HFQ

An accurate constitutive modelling AA6082 under HFQ conditions is particularly importance in numerical simulation for industrial applications. With the elastic–viscoplastic deformation and material hardening, the following set of constitutive equations is proposed and determined for micro-alloyed air-quenched steel in warm/hot forming [90]:

$$\dot{\varepsilon}_{\mathrm{p}} = \left[\frac{\sigma - B\sqrt{\bar{\rho}} - k}{K}\right]_{+}^{n} \tag{2.27}$$

$$\dot{\bar{\rho}} = A(1-\bar{\rho})\dot{\varepsilon}_{\mathrm{p}} - C\bar{\rho}^{\gamma} \tag{2.28}$$

$$\dot{\sigma} = E\left(\dot{\varepsilon}_{\mathrm{T}} - \dot{\varepsilon}_{\mathrm{p}}\right) \tag{2.29}$$

where ε_{p} is the plastic strain, σ is the stress, and $\bar{\rho}$ is the normalised dislocation density. Here $\bar{\rho}$ is defined as: $\bar{\rho} = (\rho - \rho_{\mathrm{i}})/\rho_{\mathrm{s}}$ [63], where ρ_{i} is the initial dislocation density and ρ_{s} is the saturated dislocation density. The unified constitutive equations were used to model AA6082 under hot stamping conditions of spherical parts with a central hole employing ABAQUS Finite Element (FE) software. The agreement between experimental and model results is demonstrated in Figure 2.19 and the agreement is very good.

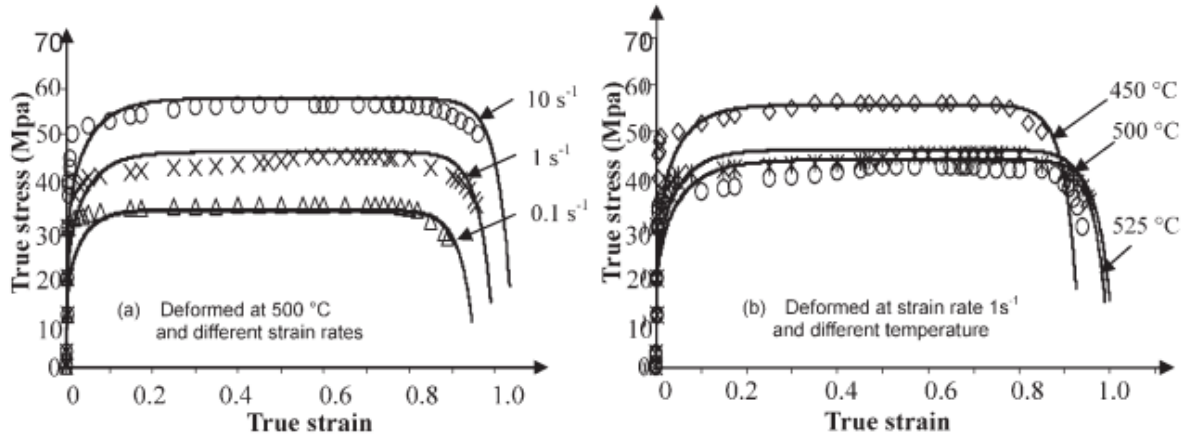


Figure 2.19 Comparison of computed (solid curves) and experimental (symbols) stress–strain relationships for AA 6082 alloy deformed at different strain rates and temperatures [91].

2.5.6 Numerical integration of constitutive equations

Most constitutive relationships and associated coupled equations, published for engineering applications, can be described by nonlinear ordinary differential equations (ODEs) for which no closed-form solutions exist for the initial conditions [92]. Therefore, several numerical integration methods have been employed to solve them [93-95]. Most practically, this is achieved using an efficient numerical solver. Two key parameters are therefore introduced: relative and absolute tolerances, which determine the accuracy of the numerical solution [96]. This numerical solving process can be challenging for certain constitutive equations. Moderate

tolerance may result in inaccurate results, whereas overly stringent tolerance may lead to excessively high computation time or failure of ODE integration, where the desired level of accuracy cannot be achieved. Numerical stiffness of an ODE system is where the system is only amenable to implicit solver without drastically reducing the stepsize. The lack of computational studies to benchmark the performance of different numerical solvers on various stiff constitutive equations means that solving these equations may be far from optimised [97]. When performing a material constant or parameter estimation in a constitutive equation, each intrinsic material parameter must be determined from experimental data [98]. Therefore, an ODE system has to be successively integrated under different simulations millions of times [86, 97]. Additionally, these mechanism-based constitutive equations, implemented into an finite element (FE) solver such as ABAQUS, can be used to predict the evolution of the mechanical and physical behaviour of a structural material during metal forming processes [99, 100]. The equations must be numerically integrated at each point of the finite element (FE) mesh for every time increment. To solve the problem efficiently, an approximate mesh size must be chosen with the minimum number of time steps (increments). During a typical FE analysis, up to 10,000 integration points and over 100-time increments are typically required, resulting in up to 10^6 numerical integrations [5, 101]. This motivates the need for efficient numerical integration of certain types of stiff constitutive equations, such as those given in the Appendix A.

Informally, an ODE is numerically stiff if implicit Runge-Kutta (RK) methods outperform explicit ones [74]. This is common in dynamic systems with varying time scales [74]. Appendix A lists three typical sets of unified viscoplastic constitutive equations for warm/hot metal forming and its related applications. These three sets of unified constitutive equations have been identified in the literature as susceptible to difficulties in efficient numerical integration owing to numerical stiffness. The ODEs describing these constitutive equations (given in Appendix A) are often multiscale and stiff, making them amenable only to implicit solvers due to their better stability properties. Therefore, the choice of numerical integration method is of particular importance. Significant research has been performed to efficiently solve stiff differential equations [102]. Owing to their simplicity, lower-order implicit numerical integration methods, such as semi-implicit methods [92], implicit Euler (IE) [74] and trapezoidal rule (TR) [103], have been frequently applied to overcome these difficulties for moderately stiff systems. Two new variants of diagonally implicit Runge-Kutta (DIRK)

methods are utilised [96, 104], which have been shown to be promising for solving stiff constitutive equations. The TR-BDF2 (backward differentiation formulae of order two, with the use of the trapezoidal rule sub-step) has been proposed as it increases the order of the method while still ensuring a stronger form of stability (L-stability) [105]. Another promising semi-implicit method is the Rosenbrock method [96] which provides an efficient method to solve nonlinear differential equations. The RADAU5 method is an advanced 5th order method belonging to the Radau IIA class [106]. The RADAU5 method, based on its collocation of Gauss-Radau points, can efficiently handle stiff differential equations.

2.6 Thermomechanical Testing for Metal Forming

To develop constitutive models, high quality experimental data are essential for the analysis of mechanisms and calibration of material constants. Thermomechanical uniaxial tensile tests are commonly conducted to understand how a material deforms under combined thermal and mechanical loading conditions. Thermomechanical tensile testing under hot stamping conditions is often conducted within the highly capable Gleeble 3800 thermal-mechanical simulator. This is because the Gleeble simulator gives a particularly good replication of complex thermal cycles involved in real world metal forming processes [3, 4]. Thermal control to the specified thermal cycle is achieved using integrated feedback control systems to ensure accurate and repeatable results. Within the Gleeble simulator, temperature control of the specimen is measured using thermocouples and induced by the Joule heating effect caused by the current flow along the specimen. Recent advancements in testing methods, including the use of Digital Image Correlation (DIC) for full field strain field measurement, XPOL and other techniques, have produced a big step forward in improving quality of strain data. DIC is applied in conjunction with mechanical testing to provide full-field strain distribution of the deformation. Figure 2.20 schematically depicts the process of material deformation under uniaxial tensile stress, leading to the formation of intergranular voids and necking, which are a start of material failure. The left side of the figure shows a flat dog boned shaped sample subjected to tensile stress σ. The right side provides a zoomed-in view of the material's microstructure in the necked region, highlighting the grains (individual crystallites) that make up the material. The intergranular voids (small circles) form along the grain boundaries due to the applied stress. These voids play a critical role in the initiation and propagation of cracks, ultimately leading to material failure.

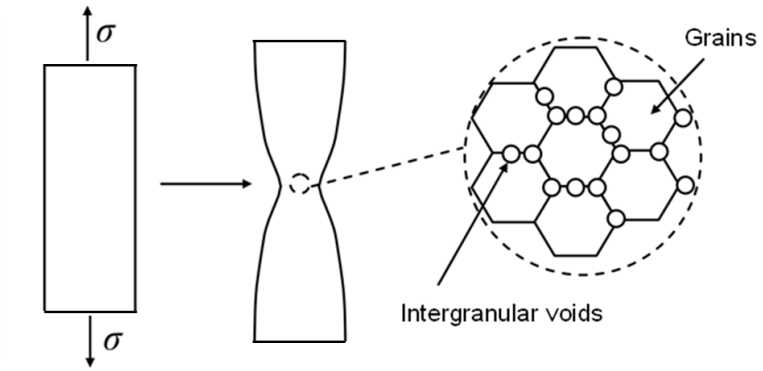


Figure 2.20 Schematic illustration of material deformation under applied stress (σ) leading to necking and the formation of intergranular voids. The magnified view shows the microstructural details, highlighting the presence of grains and intergranular voids that contribute to material failure.

In addition to uniaxial tension and compression testing, materials are often subjected to biaxial or multiaxial loading conditions. A novel test rig was developed to enable biaxial testing using the uniaxial loading in Gleeble [38]. The novel rig has been successfully employed for the determination of FLCs for boron steel and aluminium alloy under different temperatures and strain rates [107, 108].

2.6.1 Comparison of different types of strain rate control

During uniaxial testing within the Gleeble material simulator, the strain rate must be controlled to the target strain rate. Currently the only feasible way is Stroke based Strain Testing (SST) in which the stroke or displacement time relation must be defined beforehand [109]. In the conventional based SST, the displacement is controlled using the conventional equation [9]:

$$D_{\text{conv}} = l_0\left[\exp\left(\dot{\varepsilon}_{\text{Target}} \cdot t\right) - 1\right] \tag{2.30}$$

where l_0 is the central gauge length, $\dot{\varepsilon}_{\text{Target}}$ is the constant target strain rate, and t is the deformation time. This formulation is derived from the definition of true strain, under the assumption of isothermal, homogenous deformation. The equation helps to ensure that the strain rate within the specimen is controlled to the target strain rate. The conventional equation with a gauge length of 20 mm was used determine the displacement-time relation for testing and tensile tests were conducted on boron steel under a wide range of deformation conditions [9]. However, due to the temperature gradient and the tolerance of the clamping system, it has been shown that different locations along the gauge length of the sample deform at different rates [9]. It should be noted that under the conventional equation, there is no dependence on

temperature. Figure 2.21 shows the displacement versus time relationship, at three different strain rates of 0.1, 0.2 and 0.5 /s, when employing the conventional SST approach (Equation (2.30)).

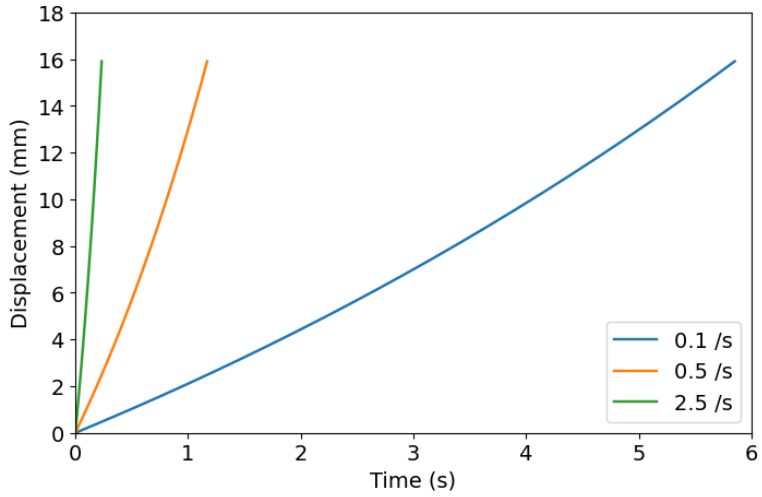


Figure 2.21 Conventional SST for 0.1, 0.2 and 0.5 /s.

The strain during Gleeble tests can be obtained using different methods, such as L-gauge, C-Gauge or DIC, which can be used for strain rate control. The L-gauge strain rate control is based on the relationship between elongation and true strain. By monitoring the specimen's elongation and adjusting the deformation rate, the target strain rate can be accurately controlled. The key equations are as follows:

$$\varepsilon_T = \ln\left(\frac{l}{l_0}\right) \tag{2.31}$$

$$\dot{\varepsilon}_T = \frac{\dot{l}(t)}{l(t)} \tag{2.32}$$

Where l_0 is the initial length, l the instantaneous length and $\dot{l}$ is the derivative. These equations are used in a feedback control system to maintain the desired strain rate during testing. The L-gauge measures the change in length directly, making it a straightforward method for controlling strain rate in tensile tests. L-gauge is a widely used method of strain measurement during mechanical testing. They provide a measurement of strain over the restrained jaw and converts this to apply a force to the specimen by stretching. Studies on tungsten samples [110], steel [111] and aluminium alloy [7] demonstrate the L-gauge wide application to different testing conditions. However, the L-gauge was found to be inaccurate at high temperature

because the strain distribution is not uniform due to the effect of temperature gradient along the specimen.

In a similar way, true strains in the longitudinal direction can also be determined from the width changes recorded by the C-gauge as given by:

$$\varepsilon_T = -2\ln\left(\frac{W}{W_0}\right) \tag{2.33}$$

$$\dot{\varepsilon}_T = -2\frac{\dot{W}(t)}{W(t)} \tag{2.34}$$

where W is the width of the specimen at the location of the C-gauge at time t and W_0 is the initial width. C-gauges can be used for strain rate control in testing; however, there is the possibility of sudden change (e.g. C-gauge falling off) which could cause damage to the machine. Additionally, C-gauges are generally attached to the geometrical centre of the specimen and the success of the test relied on the failure occurring in the geometrical centre which does not always occur.

More recently, a GPU-based DIC system for real-time strain measurements in material testing was implemented at 1.2 kHz with minimal latency [112]. It successfully replaces traditional mechanical extensometers in strain-controlled low cycle fatigue testing at room temperature. This innovation combined precise real-time control and high-speed data acquisition, crucial to achieving more accurate cyclic loading. Several studies, such as [113, 114], have similarly explored real-time DIC-based feedback control, emphasising the efficiency of the system in dynamic testing environments. However, interfacing with the Gleeble is problematic and is not currently possible with GOM 5M system.

Table 2.2 present the features of the different methods of strain rate control for use in the Gleeble. L-gauge and C-gauge are contact based strain measurements which integrate with the Gleeble own controller, predictive based displacement controlled conventional and real-time DIC based on feedback control.

Table 2.2 Comparison of different methods for strain measurement and control, highlighting their advantages and disadvantages.

Type	Method	Advantages	Disadvantages
L-gauge	Eq. (2.31)	Easy to implement	Not accurate when the strain becomes localised or non-uniform.
C-gauge	Eq. (2.33)	Can accurately control the strain rate using feedback control	Only provides accurate strain ate control if failure happens at centre. Risk of damages.
Conventional displacement control	Eq. (2.30)	Very simple formulation, can be widely used	Unable to achieve constant strain rate
Real-time DIC	Novel	Has been shown to provide feedback control in some situation.	Not currently possible with GOM 5M system.

2.7 Summary

This Chapter has provided the associated literature review and background to the PhD Thesis explaining the driving force for a move to lighter stronger alloys for transport applications. For these new lighter alloys, new forming technologies are needed such as Hot Forming Quench (HFQ) which is an integrated process for stamping of heat-treatable, high strength aluminium alloy. In order to characterise alloys for HFQ, thermomechanical testing on the Gleeble is required. However, a constant strain rate control during the tests is difficult to achieve. In this PhD dissertation, the focus has been on uniaxial deformation of aluminium alloy AA6082 and aims for a better solution. The Machine Learning techniques are described which will enable the determination of the displacement relation for each deformation condition to provide optimal strain rate control. This methodology helps improve dramatically the understanding and determination of the hardening behaviour and constitutive stress-strain data obtained from the Gleeble experiments.

3 Experimental Methodologies

3.1 Introduction

This chapter introduces the methodologies used during the mechanical testing process and subsequent data collection, which enable a complete dataset to be assembled for training of neural networks for metal forming processes.

3.2 Material and specimen design

This study focusses on heat-treatable Aluminium alloys, specifically the 6xxx series. These alloys are selected for their good weldability, corrosion resistance and formability, which makes them highly suitable for use as medium-strength structural materials. The materials used in the present study are rolled Aluminium alloy AA6082-T6 sheets. Specimens used throughout are 1.5 mm thick dog-bone specimens machined from rolled sheet material, with the length of the specimen along the rolling direction. The composition of the alloy is Al-0.87Si-0.33Fe-0.026Cu-0.51Mn-0.97Mg-0.044Cr-0.025Zn-0.016Ti (wt. %). The 6xxx series alloy, AA6082, is a precipitation-hardening medium-strength alloy which primarily uses magnesium and silicon as the major alloying elements. This is where silicon is used to increase age hardening response [115] and manganese to control the grain size [116].

3.3 Thermomechanical tensile tests

All the thermomechanical tensile experiments in this research were conducted using a Gleeble 3800 thermomechanical simulator. This well instrumented material simulator has a load capacity of 100 kN, maximum stroke rate of 2 m/s in tension and reported maximum heating rate and quenching rate of up to 10,000 °C/s. The maximum grip to grip distance is 130 mm. Specimens are mounted within the chamber between the grips, heated treated and then loaded under tension. The Gleeble has an integrated thermal management system which uses a digital controller to achieve steady state equilibrium temperature. During the tensile tests, a pair of K-type thermocouples were welded to the mid-point of the specimen for accurate temperature control to the temperature profile of the heat treatment and deformation using feedback control. The heating and quenching needed in hot forming conditions was achieved by a combination of Joule heating effects provided by the electrical current and high-pressure air to cool the specimens during quenching.

The Gleeble Material Simulator is often employed to determine the yield point behaviour, UTS and the overall stress-strain response of material uniaxial during tensile testing at a deformation temperature and constant target strain rate. Successive testing under a variety of deformation conditions has revealed there exist two uncertainties. Firstly, with regards to strain rate, a difference in experimentally obtained maximum strain rate and target strain rate values is often found, which can be attributed to the limitation in the conventional stroke-time equation see Equation (2.30). Improvement in this formulation should lead to a more steadily controlled strain rate to the UTS and also the strain rate past the UTS point where necking and failure occurs. Secondly, a temperature gradient along the parallel length of the sample with maximum temperature at the centre occurs due to the Joule or resistive heating of the gauge length and cooling of the grips. These two discrepancies make controlling the strain rate under a wide range of deformation conditions significantly challenging.

Figure 3.1 illustrates the experimental configuration used for thermomechanical tensile testing within the Gleeble Material Simulator. The layout outlines the crucial components essential for conducting controlled tensile tests under specific thermal conditions: the thermal system, the cooling system, the automatic feedback control, the strain rate control system and the strain and loading measurement.

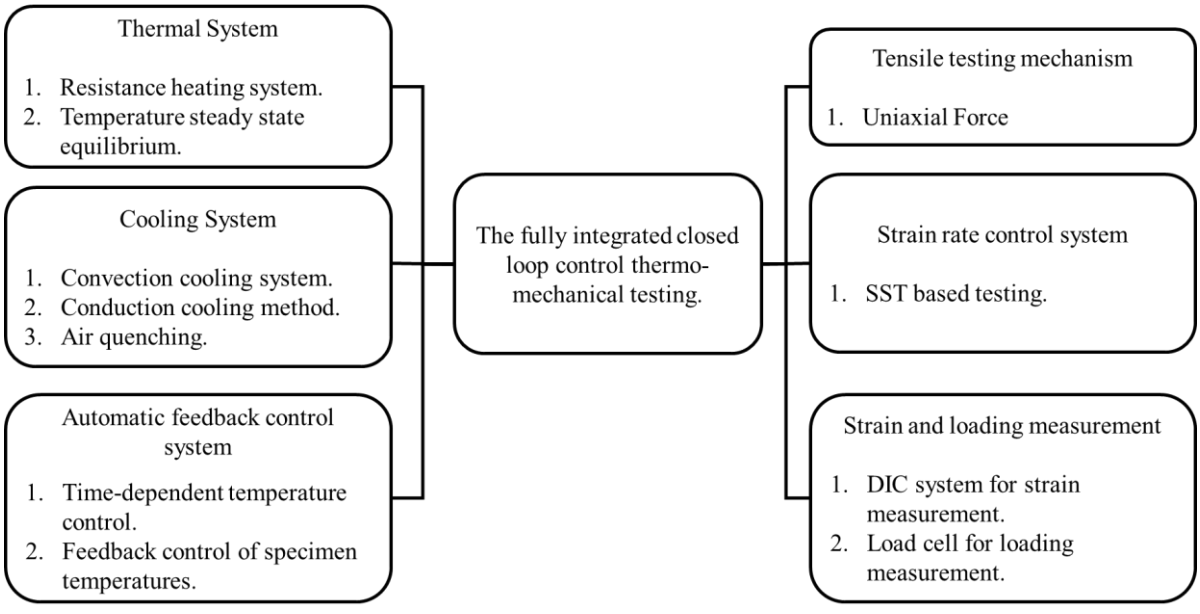
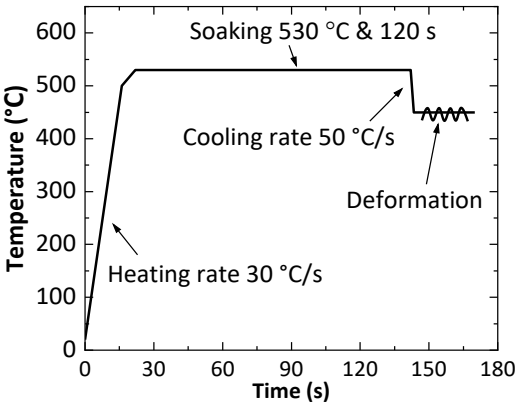


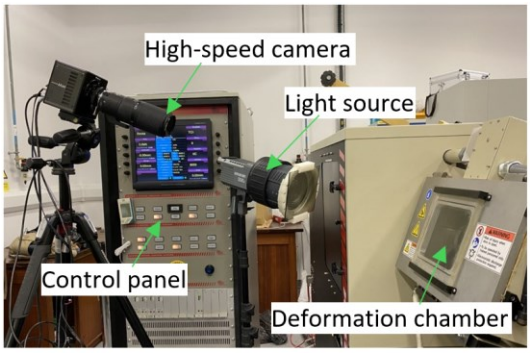
Figure 3.1 Experimental configuration for themomechanical testing.

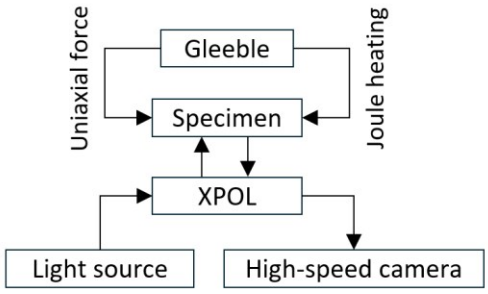
3.3.1 Experimental setup

Uniaxial tensile tests on the alloy were carried out to characterise its thermomechanical behaviour during hot stamping. To mimic industrial hot stamping conditions, the temperature cycle as shown in Figure 3.2(a) was adopted. The alloy was initially heated at 30 °C/s to 530 °C, then soaked at this temperature for 120 (Solution Heat Treatment) SHT process was completed, followed by rapid quenching at 50 °C/s to the target temperature and uniaxial tension at the target strain rate until failure. As illustrated in Figure 3.2(b), the Gleeble 3800 system was utilised to conduct the thermomechanical tests. This is primarily attributed to a feedback control thermal system embedded in the Gleeble, which enables the accurate reproduction of the complex thermal cycle. During the testing, the Gleeble provides electric current to heat each specimen by following the thermal cycle and then offers uniaxial force to stretch the specimen at a target temperature and strain rate. Figure 3.2(c) shows the specimen design for the uniaxial tensile tests, shows a flat, dog-bone-shaped metal specimen with an initial gauge length of 80 mm. The central portion of the specimen, known as the gauge length, is visibly narrower. The specimen has rectangular ends with multiple circular holes for securing it in place. The specimen was held in place by a set of special grips inserted between the water-cooled copper grips in the chamber. The grips were orientated to allow for the deformation of the specimen to be recorded with full-field DIC measurements. During the testing, a pair of thermocouples was welded at the middle of each specimen to monitor the temperature at this location and provide signals to the thermal system for the feedback control of its temperature to follow the thermal cycle as shown in Figure 3.2(c).

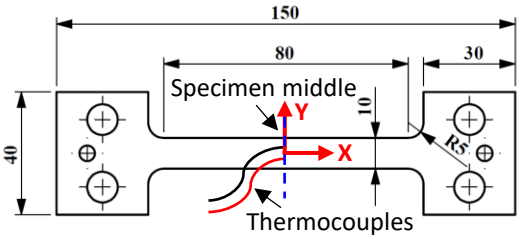


(a) Temperature cycle of aluminium alloy





(b) Gleeble machine for uniaxial tensile tests



(c) Specimen geometry and dimensions

Figure 3.2 Temperature-time profile under HFQ conditions and experimental setup.

Due to the nature of resistance heating within the Gleeble, a temperature profile exists along the gauge length. Resistive heating occurs uniformly along the gauge length of the specimen, but cooling occurs by conduction to the grips. This gives a non-uniform temperature gradient along the gauge length of the sample. The maximum temperature along the gauge length is obtained at the mid-point, which is controlled with feedback from a mid-point thermocouple to a given specified temperature. Away from the mid-point, temperature decreases along the gauge length. Engineering strain and engineering stress are defined by the following relationships:

$$\varepsilon_e = \frac{l}{l_0} - 1 \tag{3.1}$$

$$\sigma_e = \frac{F}{A_0} \tag{3.2}$$

where l is the length of the specimen, l_0 is the initial length and A_0 is the initial cross-sectional area. True strain ε_{T} and true stress σ_t describes changes in the shape/length of the material and are defined as:

$$\varepsilon = \int_{l_0}^{l} \frac{dl}{l(t)} = \ln\left(\frac{l}{l_0}\right) = \ln(1 + \varepsilon_{\mathrm{e}}) \tag{3.3}$$

$$\sigma = \frac{F}{A} = \frac{Fl}{A_0 l_0} = \sigma_e(1 + \varepsilon_{\mathrm{e}}) \tag{3.4}$$

where A is the instantaneous cross section area at time t. Strain data is obtained in each test by a series of images captured by a high-speed camera fitted with polarising filter to improve the quality of the images around the time of the localised necking. The images were processed using GOM correlate and the DIC technique with the spectral strain mapping applied.

3.3.2 Testing conditions

A variety of different test conditions (temperatures and strain rates) have been considered for AA6082, to understand further this difference between target strain rate and experimentally obtained maximum strain rate (at the centre of the specimen where the localised necking occurs). Collecting large amounts of experimental data under many different deformation conditions allow understanding how the strain field varies under different loading conditions and ultimately predict new stroke-time behaviour based on a knowledge of previous tests. This would allow the strain rate to be more accurately controlled and close to the target strain rate. The conventional equation is given by the following relationship:

$$\Delta L(t) = L_{\mathrm{V}} \cdot \left[\exp\left(\dot{\varepsilon}_{\mathrm{Target}} \cdot t\right) - 1\right] \tag{3.5}$$

Table 3.1 lists all testing conditions used for the uniaxial tensile tests on AA6082 under hot stamping conditions, including the target deformation temperatures and strain rates. These conditions were selected according to the industrial hot stamping conditions for the alloy AA6082 [117].

Table 3.1 Test programme for AA6082 under HFQ conditions for conventional approach. (√) indicating a test conducted at that deformation conditions.

		Deformation temperature (°C)		
		400	450	500
Strain rate (/s)	0.1		√	√
	0.5	√	√	√
	2.5	√	√	√

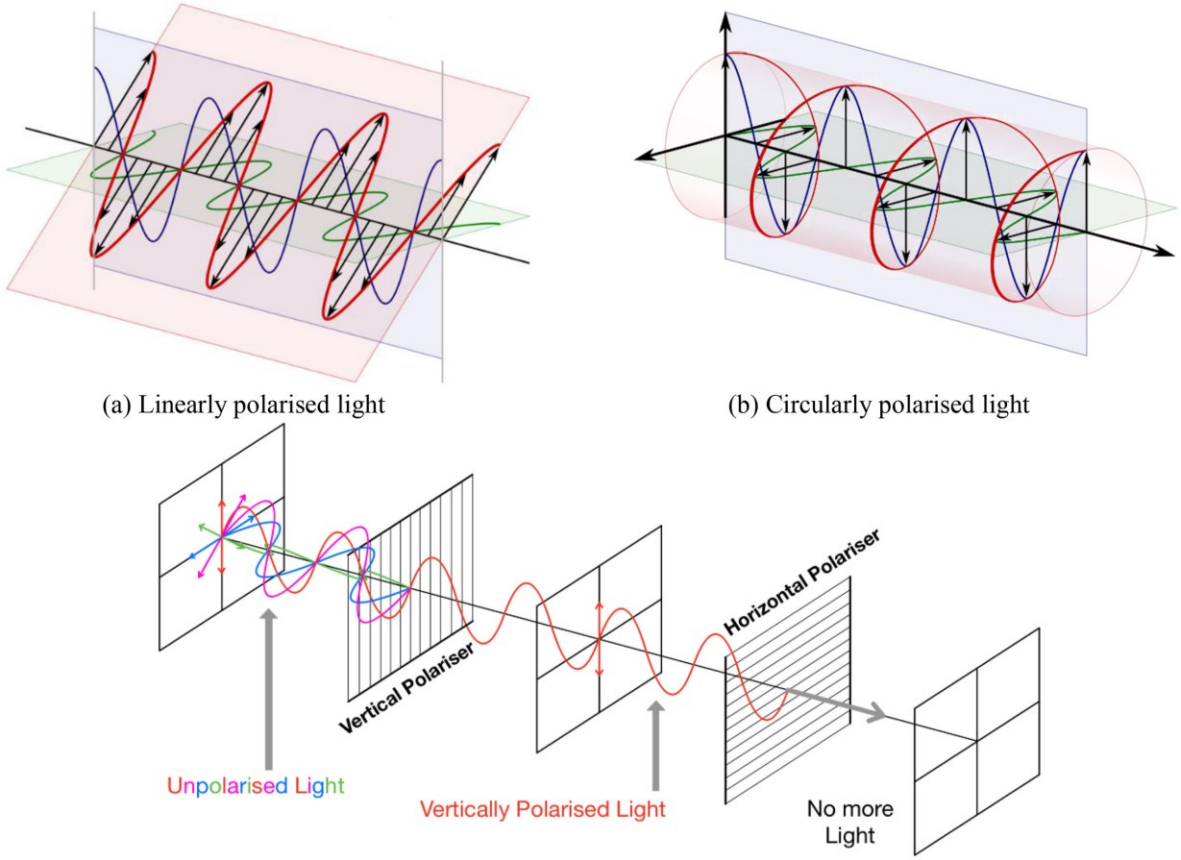
3.3.3 Digital Image Correlation (DIC)

Full-field strain measurement within the gauge area of each specimen were measured using the DIC technology. Subsequently, random speckle patterns were generated by spraying a white paint, VHT FLAMEPROOF flat white SP101 paint, known for its resistance to temperatures up to 1093 °C, to create randomly dispersed white dots on a background of thin black paint, flat black SP102 paint. The surfaces of each specimen were initially cleaned using silicon carbide abrasive papers (Grit size P800) and acetone to remove any impurity. An airbrush, operating at 30 psi pressure and held at approximately 120 mm from the specimen surface, was employed to achieve this speckle pattern. This specimen preparation allows better paint adhesion and performance at elevated temperatures [118]. The speckle pattern improves the ability of the DIC system to track surface deformation by providing distinct features that can be correlated between images taken before and after deformation. The pattern must be applied uniformly and with sufficient contrast to ensure accurate measurements. During the testing, a high-speed camera (Photron FASTCAM MINI) with a resolution of 1280 × 1024 pixels, was used to record the deformation at a fixed frame rate of 500 frames per second (fps), along with a white LED lamp (Amaran 200d LED) to illuminate the specimen. The whole gauge area was recorded during thermomechanical testing, resulting in a pixel/millimetre ratio of approximately 16. The recorded pictures were post-processed using the commercial software GOM Correlate 2018, setting facet size to 19 pixels and point distance to 16 pixels according to previous studies [117, 119] as presented in Table 3.2.

Table 3.2 Optimal setting for DIC in GOM Correlate [120].

	Point distance	Facet Size	Strain tensor neighbourhood	Interpolation size
Optimal settings	16 pixels	19 pixels	1	1

In order to eliminate the shining effects of the base material AA6082 on the recorded pictures, the cross-polarisation (XPOL) technology was used [119], with a linear polariser filter attached with the high-speed camera and another linear polariser filter attached with the lamp. Where a polarising filter was fitted to improve the quality of the images around the time of the localised necking. XPOL is utilised alongside DIC, first established for room-temperature DIC imaging [121] and extended to high-temperatures [120]. For the XPOL DIC measurements the light source is polarised before entering the camera. The lens polariser was rotated to align its polarisation axis orthogonal to the incoming light, reducing glare from the surface of the aluminium specimen. Figure 3.3(a) shows the linearly polarised light, where the electric field oscillates in a single plane, Figure 3.3(b) shows the circularly polarised light, where the electric field rotates in a helical pattern along the direction of propagation and Figure 3.3(c) shows the cross-polarisation of randomly polarised light. It should be noted when unpolarised light passes through a vertical polariser, resulting in vertically polarised light and then passes through a horizontal polariser, light is blocked entirely. This setup illustrates how cross-polarisation can block light with random polarisation.



(a) Linearly polarised light

(b) Circularly polarised light

(c) Cross polarisation of randomly polarised light

Figure 3.3 Electric and magnetic vectors of linearly and circularly polarised electromagnetic waves in the spatial domain, and the mechanism by which cross-polarisation blocks light with random polarisation angles [119].

Figure 3.4 shows the setup that was used for filtering of the unpolarised light, which is focused and polarised before hitting the specimen. Reflected light, including specular and diffusive reflections, passes through a second polariser before being captured by a camera.

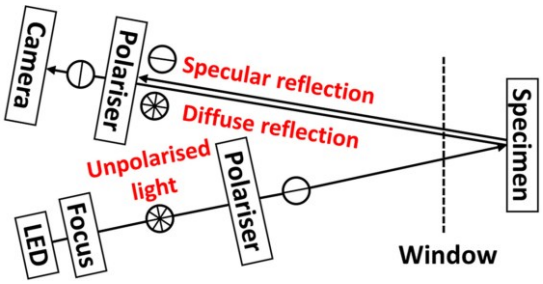


Figure 3.4 Schematic diagram of an optical setup for analysing a specimen using polarised light [119].

3.4 Summary of main findings and relation to the following Chapters

Within the Gleeble 3800 thermal-mechanical simulator experiments, a non-homogeneous strain distribution exists during deforming in hot tests because of the inevitable temperature gradient exists along the specimen. This means it is very difficult to control precisely the strain and strain rate along the specimen. Traditional methods such as employing the conventional equation (See Equation 3.5, in Chapter 3) to determine displacement control, whilst widely used, often face limitations in scalability and accuracy under varied testing conditions. The following Chapter (Chapter 4) explores the integration of the deep learning platform specifically through application of Long Short-Term Memory (LSTM) neural networks, in uniaxial tensile testing using Gleeble systems. The Machine Learning (ML) model was used to predict the strain field for a constant strain rate condition, at a given deformation temperature, and then the equation (Equation 4.11) was used to calculate the displacement-time relation that would correspond to the prediction of the strain field. By comparing the results from the conventional Stroke-based Strain Testing (SST) with the ML approach, Chapter 4 aims to demonstrate the enhanced capabilities of data-driven based models to achieve consistent, reliable strain rate control across a range of temperatures and strain rates.

4 Deep Learning Platform Approach

4.1 Introduction

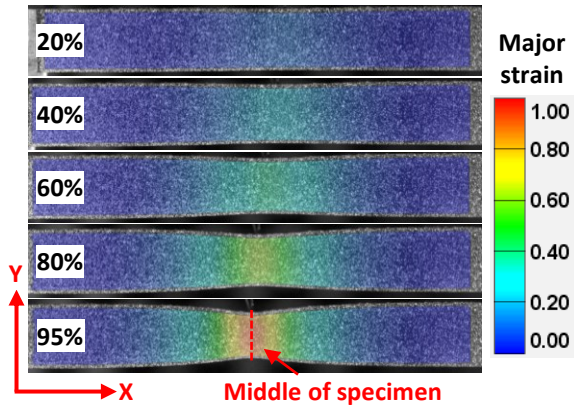
This Chapter develops a Machine Learning (ML) approach to explore the potential of using ML for the prediction and control of the strain field during thermomechanical testing on the Gleeble 3800 Thermal-Mechanical Simulator. This is for different deformation conditions which determine the displacement-time relation, associated with the test temperature and strain rate to be achieved. Previous research on this topic is covered in the Literature Review (Chapter 2). The key step forward in the research, presented in this Chapter, was to employ latest generation data acquisition techniques, employing Digital Image Correlation (DIC), to record the strain field of the sample for different temperature and strain rate conditions [3, 122]. This has been made possible by employing a high-speed camera with DIC to record the strain along the parallel section of the specimen as function of time for a tensile test specimen in the Gleeble 3800 thermomechanical simulator. By generating comprehensive datasets of the strain field, under varying deformation temperature and target strain rates, it is possible to train successfully a neural network. The trained neural network prediction of the strain field is then employed to generate a more accurate displacement-time relationship which achieves improved strain rate control. Therefore, by employing this ML approach in the Gleeble, it is possible to identify clearly the strain and strain rate hardening effects at elevated temperature and under good strain rate control conditions.

4.2 Data collection and preparation

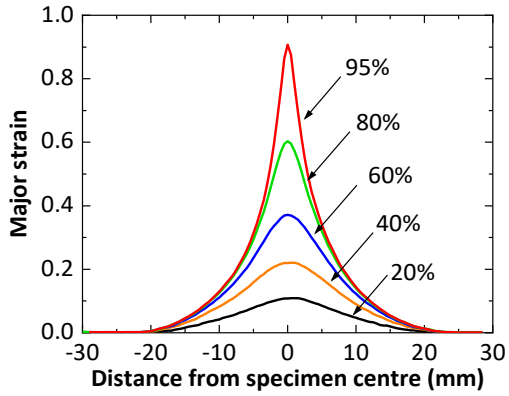
4.2.1 Data pre-processing

A high-speed camera records the deformation of a tensile specimen with a fine speckle pattern applied to the specimen. After the test, the recorded images are analysed, within GOM Correlate, utilising DIC. Full-field strain data is obtained, for each tensile test, from the series of images captured by a high-speed camera. This is when viewing the specimen in the Gleeble test chamber, at a framing rate of 500 Frames Per Second (FPS). Figure 4.2 illustrates the full strain field of a tensile test specimen, processed using DIC from captured images. The strain field is depicted in a contour plot, with varying colours representing different levels of major strain. The dark blue regions represent areas of minimal or near zero strain and the dark red

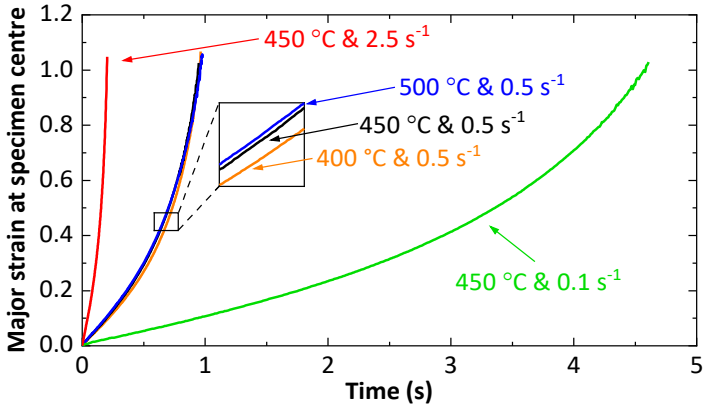
region indicate elevated strains with the maximum level of major strain of the order of 1.0. The full range of strain is given in the colour key on the right-hand side of Figure 4.1. As time increases, strain localises, and the deformation is concentrated around the centre where failure occurs. At normalised time of 1.0, the facture time, a peak strain of around 1.2 is observed. It should be emphasised that the centre where failure occurs moves to the left. This is because the right-hand end of the specimen is attached to a fixed grip and the left-hand end of the specimen is attached to a moving grip and undergoes displacement pre-defined by the Gleeble 3800 control computer.



(a) Strain fields at 450 °C & 0.5 /s



(b) Strain distributions at 450 °C & 0.5 /s



(c) Evolution of major strain at the specimen centre

Figure 4.1 Major strain fields and distributions within the gauge area at different normalised times 20%, 40%, 60%, 80% and 95%, and evolution of the major strain at the specimen centre throughout deformation under different target hot stamping conditions.

Figure 4.1 shows the scheme for the calculation of the major strain distributions along the gauge length based on the full-field strains measured using DIC. At high temperature, failure occurs near the geometrical centre because of the temperature gradient. As can be seen in Figure 4.1, deformation occurs within a central gauge length of less than 50 mm. Therefore, in

this study, only the strain distributions within a central gauge length of 50 mm only used for training and testing the ML networks. Furthermore, to enhance data stability, sections with an initial distance of 0.5 mm along the length direction were created across the specimen width. The average strain in each section was then calculated as the strain $\varepsilon(x_j, t_i)$ at that location x_j at time t_i. Consequently, there are 101 locations in total, with the specimen centre designated as x_{51}.

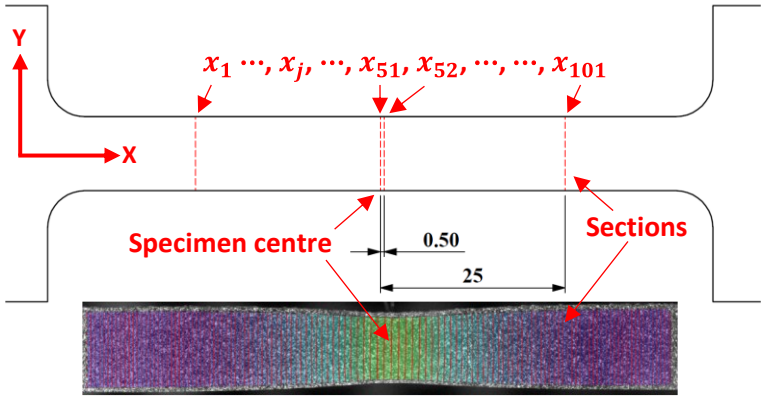


Figure 4.2: Scheme for collecting the strain distributions along the gauge length based on the strain fields measured using DIC. x_j denotes the locations along a central gauge length of 50 mm, with an initial distance of 0.5 mm from any two adjacent locations. In particular, the specimen centre was marked as x_{51}.

Above Figure 4.2 shows the strategy employed to discretise the strain field. Then, data for each deformation temperature and target strain rate information are compiled into datasets for each deformation condition. Data-smoothing is applied to each dataset using the Savitzky-Golay filter. To apply the filter, the product of the convolution coefficients and the values of the variable centred at that point Y_j:

$$\bar{Y}_j = \sum_{i=-\frac{1+m}{2}}^{\frac{1+m}{2}} C_i \cdot Y_{i+j} \tag{4.1}$$

where $\bar{Y}_j$ is the smoothed data from Savitzky-Golay filter and C_i are the convolution coefficients which depend on the number of points and polynomial degree. The Savitzky-Golay filter is effective for data smoothing in applications where preservation the original shape and features of the data is critical. The filter is applied on a window of *m* points and the convolution coefficient are calculated based degree *N* polynomial. The Savitzky-Golay filter has appropriate properties for this application. This is because the sum of convolution coefficients for smoothing is equal to one and applying the Savitzky-Golay filter leaves the area under the

function unchanged and for a polynomial order of one, then, a moving average data smoothing is obtained.

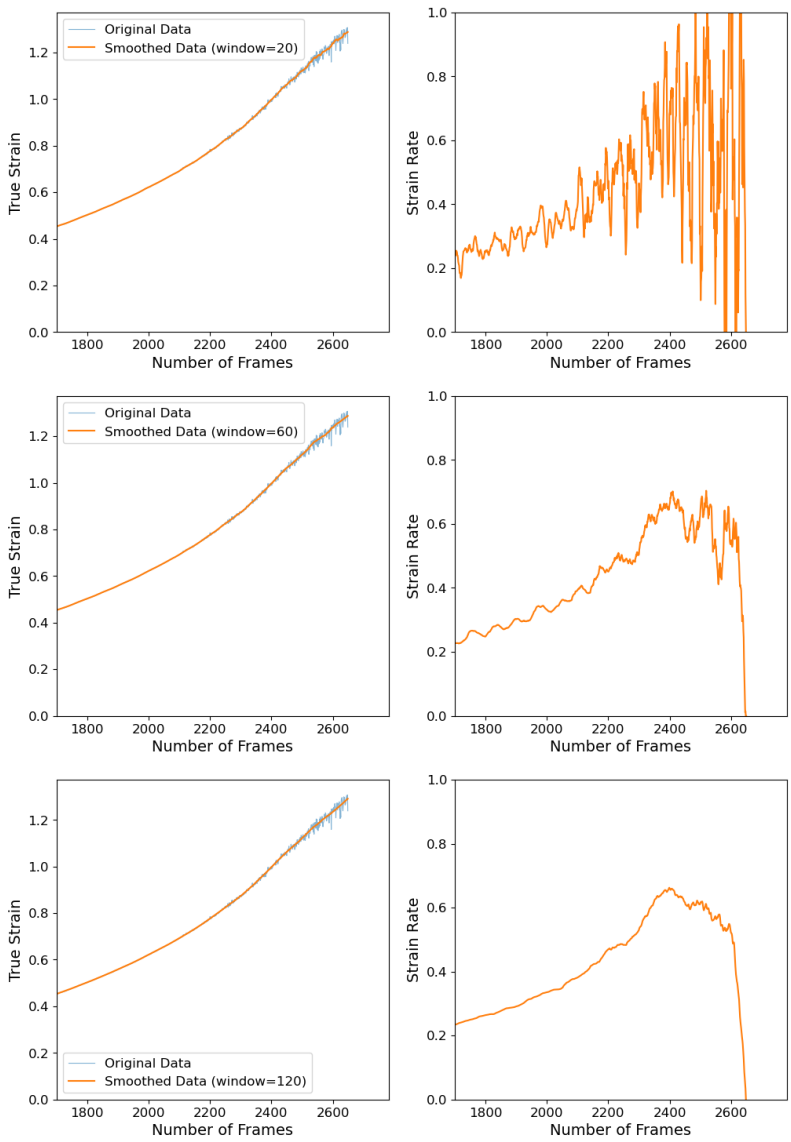


Figure 4.3: Data smoothing for a window size of 20, 60 and 120 using the Savitzky-Golay filter of polynomial order 2 on deformation conditions of temperature 450 ºC and target strain rate of 0.1 /s.

When applying the Savitzky-Golay filter, for all conditions, a polynomial order of two was selected.

4.2.2 Data characteristics

As described above, GOM Correlate and DIC are used to extract the full strain field. In Figure 4.4 the experimentally obtained strain field during deformation are shown. This is for increasing time ($t/t_f = 0.2$ to 0.95, with time, t, divided by time to failure, t_f) plotted and

displayed together, for the selected deformation temperatures and target strain rates, as defined, in Figure 4.4(a)-(f). For all these experiments, the conventional approach of Stroke-based Strain Testing (SST) is employed. Before analysing Figure 4.4, it should be pointed that there is a temperature gradient along the specimen produced water cooled grips which hold specimen in place. When this cooling, at either end of the specimen, is combined with the resistive heating along the gauge length of the specimen, this leads to a non-uniform temperature along specimen with temperature peak at the mid-point of the specimen. This leads to a non-homogenous strain distribution and subsequent necking occurring near the centre of the specimen this is shown in Figure 4.4. This means the strain localisation and subsequent necking will occur near the geometrical centre and the strain distribution shows a strong symmetry about the mid-point of the specimen and with subsequent failure occurring at the mid-point. It is important to note that as the target strain rate increases or the deformation temperature decreases. The strain distribution tends to become broader, indicating more extensive plastic deformation. Conversely, higher temperatures and lower strain rates result in sharper peaks, which indicate of a more localised deformation. Data was obtained using the conventional approach of SST (see Equation (3.5) with $L_v = 20$).

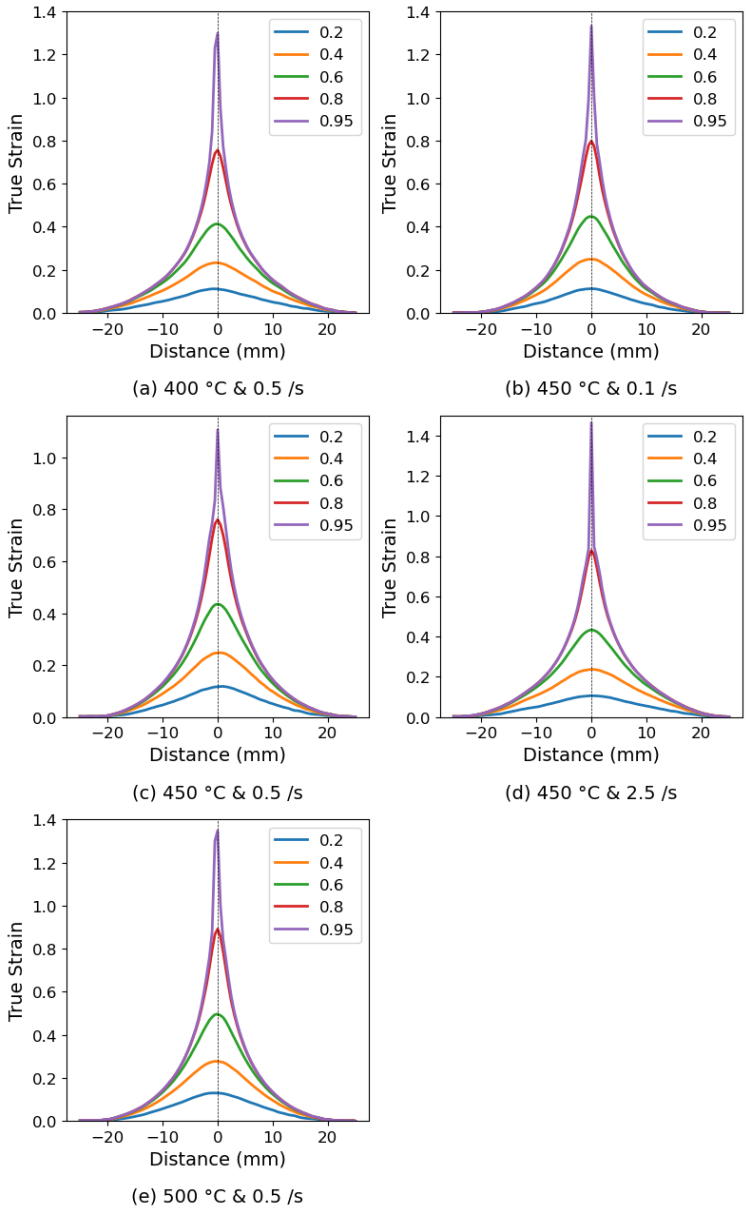


Figure 4.4: True strain distribution across the aluminium alloy specimen centred at the failure point, as captured by DIC, at $t/t_f = 0.2$, 0.4, 0.6, 0.8 and 0.95 when employing the conventional approach. Each subfigure (a) to (f) corresponds to a unique deformation condition with temperature and target strain rate defined in the bottom left.

In Table 4.1 we quantify the characteristics of the strain field at a strain level at the centre of 0.5, assessing the impact of deformation temperature and target strain rate on statistical measures. Table 4.1 outlines the mean, standard deviation, skewness, and kurtosis, under varying deformation temperatures and target strain rates under the conventional approach. These parameters provide insights into the distribution of strain in the specimen under different deformation temperatures and target strain rate.

Table 4.1 Effects of deformation temperature and target strain on standard deviation and mean of the strain field when employing the conventional approach.

Forming temp and strain rate T, $\dot{\varepsilon}_{\text{Target}}$	Mean μ	Standard Deviation σ	Kurtosis K	Skewness S
375 °C, 0.1 /s	0.235	0.133	-0.856	0.625
400 °C, 0.1 /s	0.217	0.147	-0.967	0.579
450 °C, 0.1 /s	0.227	0.139	-0.894	0.616
500 °C, 0.1 /s	0.206	0.156	-1.011	0.609
375 °C, 0.5 /s	0.260	0.127	-1.024	0.464
400 °C, 0.5 /s	0.277	0.139	-1.362	0.199
450 °C, 0.5 /s	0.244	0.135	-1.027	0.509
500 °C, 0.5 /s	0.205	0.151	-0.949	0.619
450 °C, 2.5 /s	0.257	0.128	-0.978	0.577

The standard deviation determines the spread of the data from the mean with a lower standard deviation indicating a more uniform distribution with data closer to the mean. Skewness is a measure of the asymmetry of the distribution about its mean. This skewness value can be positive, zero, or negative, depending on the direction of the skew. Kurtosis, on the other hand, assesses the 'tailedness' of the distribution to the mean. The kurtosis value can be positive, zero, or negative, depending on the shape of the data distribution, with higher values indicating a distribution with more pronounced tails. The mean μ, standard deviation σ, skewness S and kurtosis K is calculated respectively from the strain distribution as:

$$\mu = \frac{1}{N}\sum_{i=1}^{N} x_i \tag{4.2}$$

$$\sigma = \sqrt{\frac{1}{N}\sum_{i=1}^{N}(x_i - \mu)^2} \tag{4.3}$$

$$S = \frac{1}{(N-1)}\sum_{i=1}^{N}\left(\frac{x_i-\mu}{\sigma}\right)^3 \tag{4.4}$$

$$K = \frac{1}{N}\sum_{i=1}^{N}\left(\frac{x_i-\mu}{\sigma}\right)^4 \tag{4.5}$$

where N is the number of samples of data x_i.The data shows that the mean of the distribution increases at lower deformation temperatures and higher strain rates. The skewness of the distribution indicates a slight skew towards the positive 'x' direction with skewness decreasing at lower deformation temperatures and higher strain rates. The kurtosis of each distribution is negative in all cases meaning that the tails of the distribution are smaller than those of a normal distribution (which has a kurtosis of zero). The data also showed that the standard deviation was largely unchanged under changing deformation temperature and target strain rate.

In Figure 4.5(a), the effect of deformation temperature is investigated on the normalised strain rate for deformation and target strain rate conditions: 400 °C & 0.5 /s, 450 °C & 0.5 /s, 500 °C & 0.5 /s under constant target strain rate. Figure 4.5(b) shows the effect of target strain rate, on the experimentally obtained normalised maximum strain rate for the following deformation conditions: 450 °C & 0.1 /s, 450 °C & 0.5 /s, 450 °C & 2.5 /s under constant deformation temperature. A window size of 5, 25 and 120 for each target strain rates of 0.1, 0.5 and 2.5 /s was applied respectively. The normalised strain rate is plotted versus normalised time in both cases for Figure 4.5.

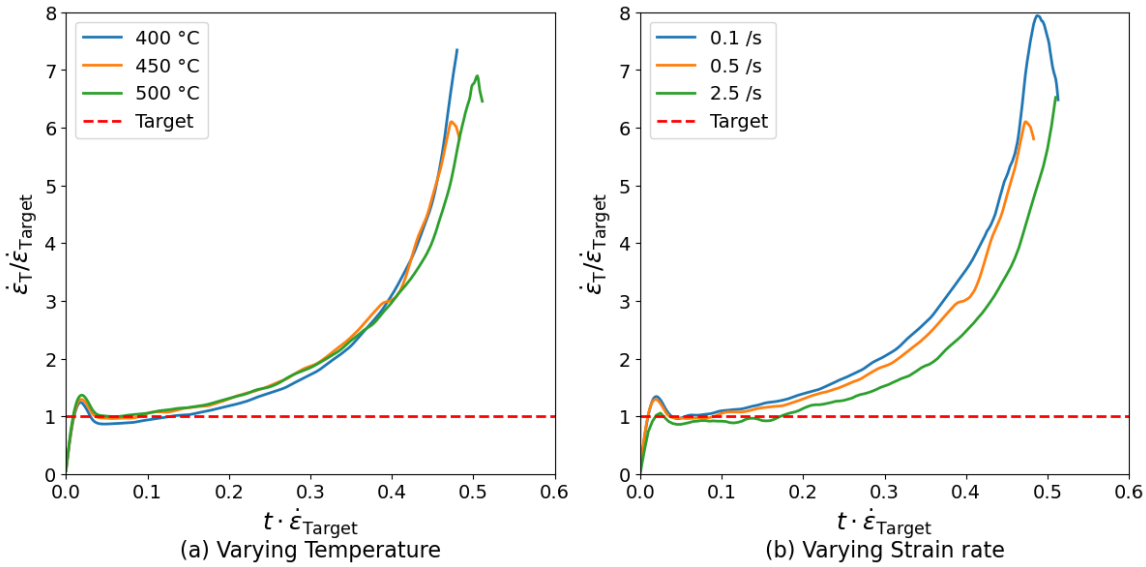


Figure 4.5 Evolution of normalised maximum strain rate at the failure location of aluminium alloy tensile specimen under varying conditions employing the conventional approach, for: (a) different temperatures of 400 °C, 450 °C and 500 °C and a target strain rate of 0.5/s, and (b) different target strain rates of 0.1, 0.5 and 2.5 /s at a constant temperature of 450 °C.

Figure 4.5(a) shows that for the same strain rate of 0.5 /s, the normalised strain rates are similar for different temperatures. This is because the displacement-time settings are the same from

Eq. (3.5). There is some deviation towards the end of test and the highest strain rate almost exceeded 8 times the target strain rate was obtained at 400 °C. Figure 4.5(b) shows that as the target strain rate decreases, the normalised maximum strain rate increases, and the material deforms more rapidly. Overall, the large discrepancy between the observed or actual strain rate and the target strain rate for this conventional equation shows that the conventional equation is unsuitable, particularly past a normalised time of 0.4.

4.2.3 Data normalisation

The inputs and outputs of the LSTM network include strain, temperature and strain rate. These variables have different units and scales. To enhance the effectiveness and efficiency of this ML model, in the present study, these variables were normalised by adopting one of the most common methods, min-max normalisation [123], which can be expressed as:

$$V' = \frac{V - V_{\min}}{V_{\max} - V_{\min}} \tag{4.6}$$

where V is the variable in inputs/outputs, $V_{\max}$ is the maximum value of V, $V_{\min}$ is the minimum value of V, and V' is the normalised variable. Table 4.2 lists both the minimum and maximum values of the variables included in inputs and outputs, which were selected according to the data characteristics in thermomechanical testing under hot stamping conditions, as presented in Section 3. The maximum value of the major strain at the specimen centre was set to 1.5. This is because according to Figure 4.4, all major strains at different temperatures and strain rates are less than 1.5. Regarding the temperature, it ranges from 300 to 530 °C under hot stamping conditions. Additionally, the strain rate under hot stamping conditions is less than 10 /s. These parameters for the min-max scaling are generally adjustable under different materials and applications.

Table 4.2: Minimum and maximum values for the normalisation for each variable in inputs and outputs.

	Min	Max
Major strain	0	1.5
Temperature (°C)	300	530
Strain rate (/s)	0	10

4.3 Learning strategies and architecture of LSTM models

State-of-the-art data-driven ML technologies are used to predict the displacement $\Delta L(t)$ for stretching specimens during thermomechanical testing. The goal is to ensure that the actual strain rate at the centre of the specimen achieves the target strain rate throughout deformation. Due to nonuniform strain distribution in the gauge area (see Figure 4.1), this is challenging. Therefore, if machine learning can accurately predict the strain distribution where the central strain rate matches the target strain rate, the exact displacement can be retrospectively determined. However, predicting the strain distribution under these conditions is difficult because of the complex dependencies on strain rates and deformation temperatures (see Figure 4.4). In conventional experimental data, the actual strain rate at the centre is often higher than the target strain rate during most of the deformation process. This discrepancy leads to errors when calculating strain distributions based on the assumption that the actual strain rate equals the target strain rate. Additionally, the evolution of strain rates at different target temperatures and strain rates follows similar trends over deformation time (see Figure 4.5), which presents significant challenges in collecting effective and representative data for training the ML models.

The novel approach uses Long-Short Term Memory (LSTM), a type of recurrent neural network (RNN) known for the capability of handling time-series data [47, 124]. The LSTM network was firstly trained and tested by utilising the experimental data with the conventional strain rate control approach with poor strain rate control. Table 4.3 lists the testing conditions of the datasets used for training and testing the LSTM network. The conditions for the training include three temperatures ranging from 400 to 500 °C, and three strain rates ranging from 0.1 to 2.5 /s. The conditions for the testing include two temperature and two strain rate conditions which are different from those used for the training.

Table 4.3 Conditions including the deformation temperatures and strain rates of the datasets used for training and testing the LSTM networks, in which the conventional approach was adopted for the strain rate control.

Number	Training	Testing
1	400 °C & 0.5 /s	400 °C & 2.5 /s
2	450 °C & 0.1 /s	500 °C & 0.1 /s
3	450 °C & 0.5 /s	500 °C & 2.5 /s
4	450 °C & 2.5 /s	
5	500 °C & 0.5 /s	

Data acquired from experimental testing was obtained with a high-speed camera at 500 FPS. For training purposes, the data in the input and output were concatenated into one complete data-frame to avoid batch training.

4.3.1 Training data structure

The number of LSTM hidden layers and choices of hyperparameters, associated with the architecture and complexity of the LSTM model. The novel approach uses Long-Short Term Memory (LSTM), a type of recurrent neural network (RNN) known for the capability of handling time-series data [47, 124]. An epoch represents a complete pass or iteration through the entire training dataset. During each epoch, the model receives the input data, makes predictions, calculates the loss, and updates its weights to improve the performance. This means the model will iterate many times over the training dataset. The learning rate is a hyperparameter that determines the step size at which the weighting parameters, associated with the model, are updated during the training process in response to the calculated loss. The window size refers to the number of previous time steps considered when making predictions for the current time step.

The chosen architecture of the LSTM neural network is outlined in Table 4.4. This network has four layers: an input layer, two hidden layer and an output layer. The input layer has three elements, including the strain $\varepsilon(x_{51}, t_i)$ at the specimen centre x_{51} at time t_i, applied strain rate $\dot{\varepsilon}(x_{51}, t_i)$ and the target deformation temperature T_{k} namely $[\varepsilon_k(x_{51}, t_i), \dot{\varepsilon}_k(x_{51}, t_i), T_{\mathrm{k}}]$. The hidden layers are a LSTM layer and a dense layer. The LSTM layer consists of 32 LSTM units/neurons and the dense layer consists of 64 nodes [125].

Table 4.4: Architecture of Neural Network giving the Shape and Parameters of each layer.

Layer	Shape	Parameters
Input	3	-
LSTM	32	4492
Dense 'linear'	64	2112
Dense 'linear'	101	6565
Total Parameters: 13169		
Window size: 1		
Learning rate: 0.001		
Epochs: 300		

The number of adjustable parameters is the total number of biases plus the number of weights for each layer. The number of parameters of an LSTM layer satisfies $4[n^2 + mn + m]$ where m is the number of inputs to the LSTM layer and n is the number of outputs from the LSTM layer. The factor of four appears because there are four gates in the LSTM cell. For dense layer where there is one gate, the number of parameters satisfies $(m + 1)n$ since there are n weights of size m and n biases. The number of layers and associated units and nodes were chosen according to the literature [126].

The input contains three elements the centre strain, centre strain rate and deformation temperature and is given by $\boldsymbol{X}_{\mathrm{k}}$ for the kth dataset. The output structure is the strain field, for each deformation condition contains totals 101 elements and is given $\boldsymbol{Y}_{\mathrm{k}}$ for the kth dataset.

$$\boldsymbol{X}_{\mathrm{k}} = \begin{bmatrix} \varepsilon_{\mathrm{k}}(x_{51}, t_1) & \dot{\varepsilon}_{\mathrm{k}}(x_{51}, t_1) & T_k \\ \vdots & \vdots & \vdots \\ \varepsilon_{\mathrm{k}}(x_{51}, t_{N_k}) & \dot{\varepsilon}_{\mathrm{k}}(x_{51}, t_{N_k}) & T_k \end{bmatrix} \tag{4.7}$$

$$\boldsymbol{Y}_{\mathrm{k}} = \begin{bmatrix} \varepsilon_{\mathrm{k}}(x_1, t_1) & \cdots & \varepsilon_{\mathrm{k}}(x_{51}, t_1) & \cdots & \varepsilon_{\mathrm{k}}(x_{101}, t_1) \\ \vdots & & \vdots & & \vdots \\ \varepsilon_{\mathrm{k}}(x_1, t_{N_k}) & \cdots & \varepsilon_{\mathrm{k}}(x_{51}, t_k) & \cdots & \varepsilon_{\mathrm{k}}(x_{101}, t_{N_k}) \end{bmatrix} \tag{4.8}$$

where $\varepsilon_{\mathrm{k}}(x_j, t_i)$ is the strain for the k^{th} dataset or deformation condition at discrete position x_j and time t_i. T_k denoted the deformation temperature of the k^{th} dataset and t_{N_k} is the number of time points within the k^{th} dataset. Subsequently the input data and output data for each condition is concatenated into one complete training dataset as $\boldsymbol{X}_{\text{input}} = \begin{bmatrix} \boldsymbol{X}_1 \\ \vdots \\ \boldsymbol{X}_{\mathrm{M}} \end{bmatrix}$ and $\boldsymbol{Y}_{\text{output}} = \begin{bmatrix} \boldsymbol{Y}_1 \\ \vdots \\ \boldsymbol{Y}_{\mathrm{M}} \end{bmatrix}$.

During the training of the LSTM networks A loss/objective function was defined. The Mean Squared Error (MSE) was chosen as the loss function due its effectiveness, ease of optimisation, and simplicity of implementation. The MSE is a convex and differentiable function, which makes it well suited to optimisation. It is expressed mathematically as:

$$L_{\mathrm{MSE}} = \frac{1}{\sum_{k=1}^{M}(N_k \cdot L)} \sum_{k=1}^{M} \left(\sum_{i=1}^{N_k} \sum_{j=1}^{L} (\varepsilon_{\mathrm{k}}(x_j, t_i) - \hat{\varepsilon}_{\mathrm{k}}(x_j, t_i))^2 \right) \tag{4.9}$$

where M is the total number of tests/datasets used for training, N_k is the total number of the time increments in the k^{th} test/dataset, L is the total number of the strain locations along the gauge length which is 101 in this study, $\varepsilon_{\mathrm{k}}(x_j, t_i)$ is the actual strain (ground truth) at location x_j, time t_i, and k^{th} test/dataset $\hat{\varepsilon}_{\mathrm{k}}(x_j, t_i)$ is the corresponding predicted strain at the same location, time and condition.

4.3.2 Deep learning platform

A schematic of the training and prediction process, as part of the deep learning platform, is shown in Figure 4.6. This is where, in Figure 4.6, the input vector $\boldsymbol{X}_{\mathrm{input}}$ (shown by the orange nodes) and the output vector $\boldsymbol{Y}_{\mathrm{output}}$ (shown by the red nodes). During the training process the ADAMs solver is used to adjust the weights and biases (shown by the green nodes).

Figure 4.6 presents the architecture of the novel data-driven ML approach developed used to calculate the displacement $\Delta L(t)$ for stretching specimens at target deformation temperatures and strain rates. Using the trained LSTM neural network, the strain field under the different deformation conditions $(T, \dot{\varepsilon}_{\mathrm{Target}})$ can be predicted. This is where, for each deformation condition, the input vector to the LSTM neural network is taken as $\boldsymbol{X}_{\mathrm{input}} = [\dot{\varepsilon}_{\mathrm{Target}} \cdot t, \dot{\varepsilon}_{\mathrm{Target}}, T]$ for deformation temperature T, constant strain rate of $\dot{\varepsilon}_{\mathrm{Target}}$ and centre strain of $\bar{\dot{\varepsilon}}_{\mathrm{Target}} \cdot t$ where t is the time points. This input structure captures the key parameters influencing the strain field of AA6082 under HFQ conditions and uniaxial conditions. Subsequently the displacement relationship under this predicted deformation can be calculated by integration.

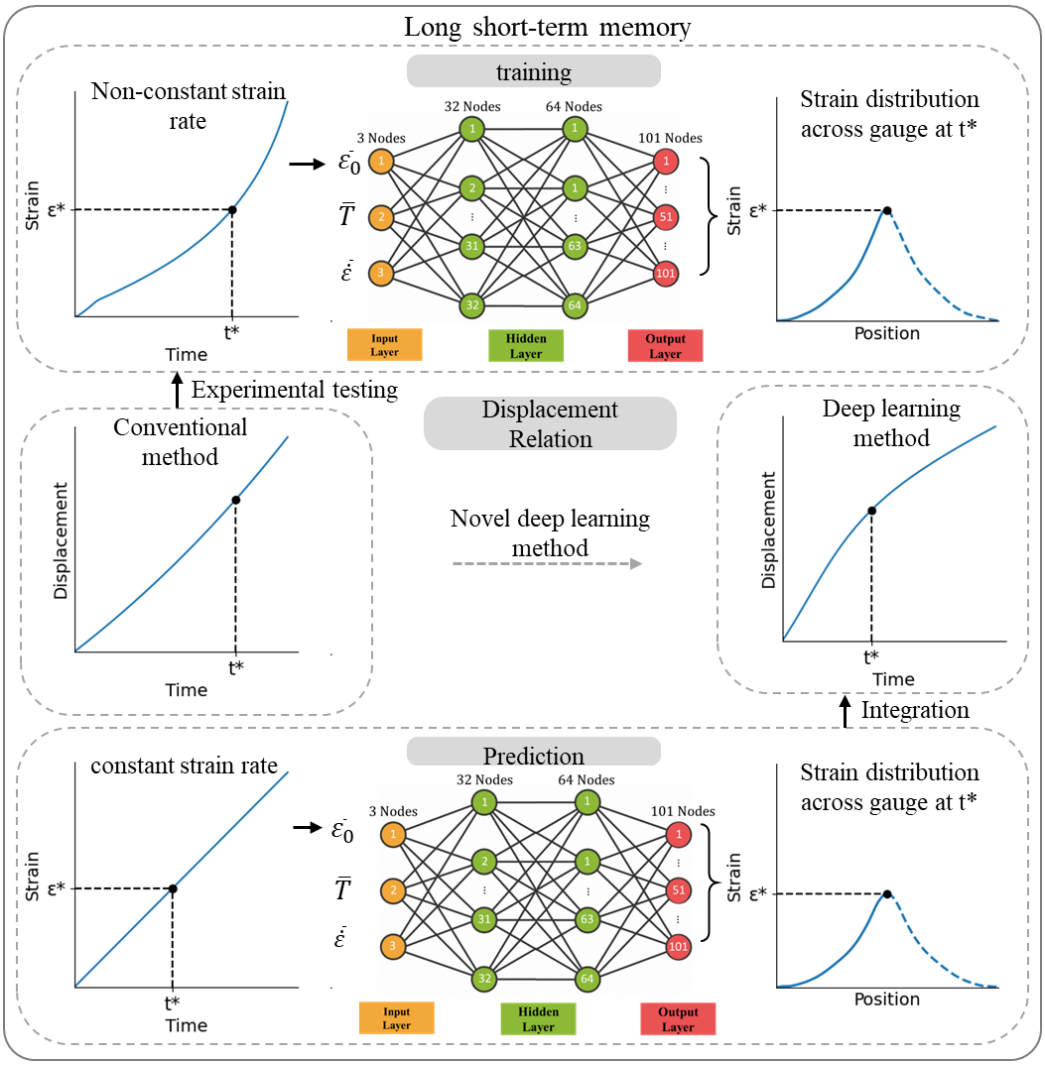
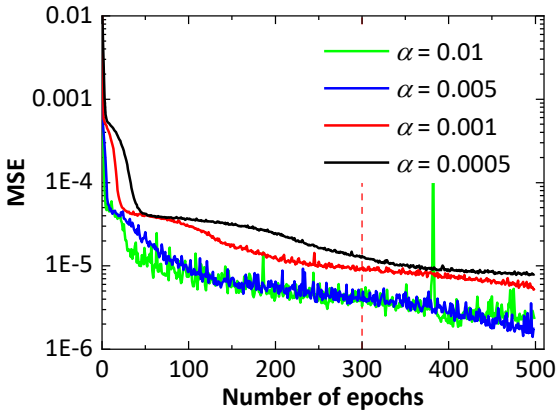


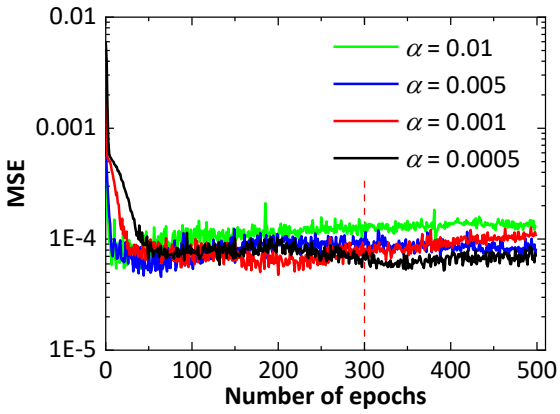
Figure 4.6 Schematic of training process and prediction process.

4.4 Effect of learning rate

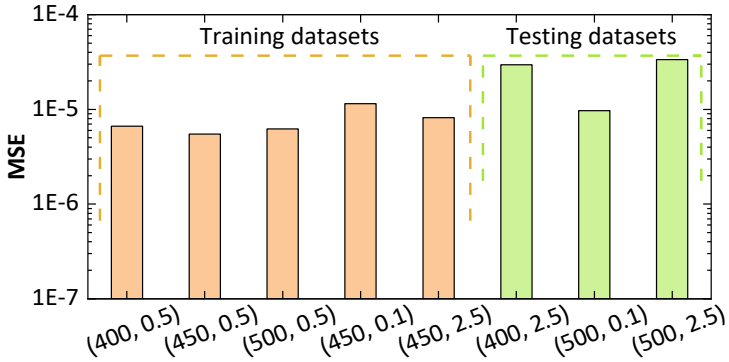
Figure 4.7 displays the evolution of the MSE values against the number of epochs at different learning rates for all training and testing datasets, respectively. As observed, at α = 0.01 or 0.005, the training loss curve shows large oscillations, indicating that these learning rates are too high. At learning rate of α = 0.0005, the training loss was found to converge too slowly. The learning rate α = 0.001 results in both training loss and testing loss decreasing and stabilising. This justifies the selection of α = 0.001. Additionally, based on the trends observed in Figure 4.7(a)-(b), the number of the epochs required to effectively minimise the loss function was determined to be 300. Figure 4.7(c) presents the MSE for each dataset used in both training and testing, measured at 300 epochs. As observed, the different datasets yield consistently low MSE values, around 5E-5, indicating the high-quality training of the LSTM networks



(a) MSE for training datasets (training loss)



(b) MSE for testing datasets (validation loss)



(c) MSE of individual datasets used for training and testing at 300 epochs

Figure 4.7: Evolution of training loss and testing loss (i.e. the MSE) against the number of epochs at different learning rates, and the MSE of individual datasets used for both training and testing.

4.5 Uniaxial test programme using ML predictions.

During uniaxial testing within the Gleeble thermomechanical material simulator, the strain rate should be controlled to the target strain rate. The conventional way is SST testing in which the displacement-time relation is defined beforehand. Currently there is no general formula that has been found to provide good agreement at all deformation conditions. However, Using the trained LSTM neural network, the strain field under the deformation conditions $(T, \dot{\varepsilon}_{\mathrm{Target}})$ can be predicted. This is where, for each deformation condition, the input vector to the LSTM neural network can be expressed as:

$$\hat{\varepsilon}(x,t) = \mathrm{NN}(\boldsymbol{X}_{\mathrm{input}}) \tag{4.10}$$

$$\Delta L(t) = \int_{-L_{\mathrm{E}}/2}^{L_{\mathrm{E}}/2} [\exp(\hat{\varepsilon}(x,t)) - 1]\mathrm{d}x \tag{4.11}$$

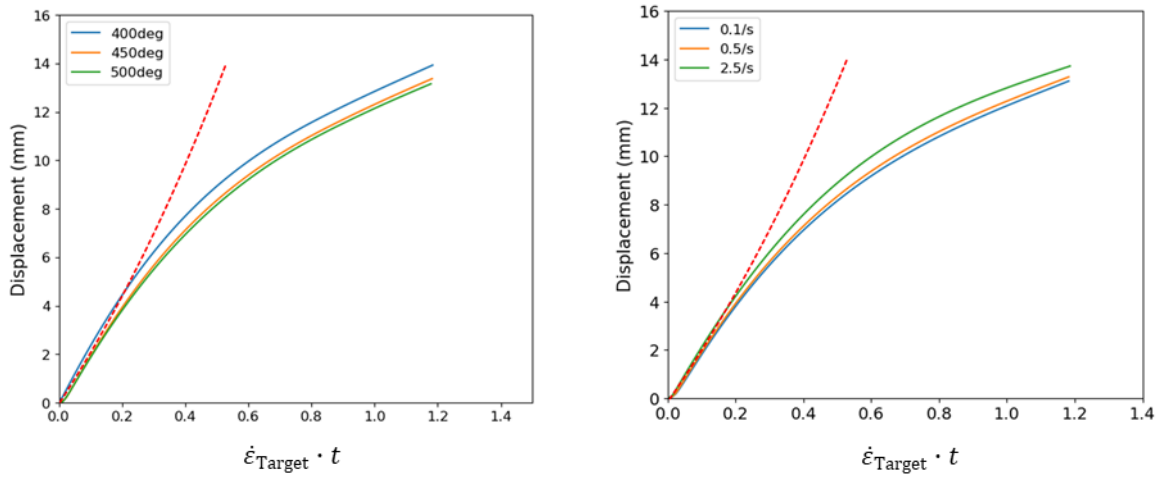
where NN is the trained neural network and $\hat{\varepsilon}(x,t)$ is the predicted strain field. This input structure captures the key parameters influencing the strain field of AA6082 under HFQ conditions and uniaxial conditions. Subsequently, Equation (4.11) is applied to calculate the displacement relationship under this predicted deformation under ideal strain rate control. Table 4.5 presents the test matrix of the uniaxial tests under different deformation conditions based on the machine learning determined displacements rather than displacements determined by the conventional relationship.

Table 4.5: Test programme for AA6082 under HFQ conditions for machine learning approach. (√) indicating a test conducted at that deformation conditions.

		Deformation temperature (°C)		
		400	450	500
Strain rate (/s)	0.1	√	√	
	0.5	√	√	√
	2.5		√	

4.6 Displacement relationships

During uniaxial testing within the Gleeble thermomechanical material simulator, the strain rate as well as temperature, must be controlled to the target strain rate. In Figure 4.8 the dashed line corresponds to the conventional equation (refer to Equation (3.5) with pre-forming gauge length of $L_v = 20$). The Machine Learning model was used to predict the strain field for each target strain rate and given deformation temperature, then, Equation (4.11) was used to calculate the displacement relation that would correspond to this prediction of the strain field.



(a) Effect on deformation temperature at 0.5 /s

(b) Effect of target strain rate at 450 °C

Figure 4.8 Displacement predicted using the novel data-driven ML (solid lines) and conventional approach (dashed), for stretching specimens under different hot stamping conditions. The horizontal axis represents the product of the target strain rate $\dot{\varepsilon}_{\text{Target}}$ and time t, namely the target strain.

All the ML predictions of displacement show similar trends, with an initial period of sharp increase followed by the displacement increasing at a near constant rate towards the end of the deformation. As time progresses, the difference between the machine learning model and the conventional equation increases significantly. The ML method is considered preferable as it produces a better representation of the localisation of strain and the constitutive properties for the material. Figure 4.8(a) illustrates for the ML prediction that a rise in the deformation temperature results in a decrease in displacement at a given time point, whilst the conventional formulation of displacement does not depend on deformation temperature. Figure 4.8(b) shows for the ML predictions, that higher strain rates correspond to a more rapid increase in displacement and at lower strain the difference between the conventional equation and the ML predictions is more pronounced.

4.7 Discussion of main findings

This study successfully demonstrates the integration of Gleeble thermomechanical material simulator, with data-driven material modelling, using LSTM neural networks under hot stamping conditions. By accurately predicting strain distributions across various deformation temperatures and strain rates, the optimal displacement time relations can be found. Therefore, this novel approach not only mitigates the inaccuracies attributed in the conventional SST but also can achieve far superior strain rates control. It is considered that this data-driven approach is currently the most effective tool for controlling strain rate in Thermomechanical testing.

5 Experimental Results for Materials Characterisation

5.1 Introduction

In this chapter, the detailed results from the experiments outlined in Chapter 3 are presented and analysed to assess the material properties and formability of the aluminium alloy, AA6082, under HFQ conditions. The effects of strain rate and temperature on the flow stress response are discussed based on the uniaxial tensile test results. By comparing the results from the conventional SST (Stroke-based Strain Testing) with the ML-based approach, this chapter aims to demonstrate the enhanced capabilities of data-driven models to achieve consistent, reliable strain rate control across a range of temperatures and strain rates. In addition, the data were used to fit the commonly used Norton-Hoff model, Johnson-Cook model and an ODE-type unified constitutive model. This Chapter showcases how ML can transform material testing, leading to more accurate data, and better understanding of material constitutive properties and behaviour.

5.2 Force and displacement relations

For tensile testing with SST, the displacement-time relationship needs be pre-defined, which is the key input for strain rate control, for the Gleeble 3800 thermal-mechanical simulator. The displacement versus time relations have been presented in Figure 4.8 for the two different methodologies, namely the Machine Learning (ML) and Conventional (Conv) approach with pre-forming gauge length of $l_0 = 20$ mm. Figure 5.1 shows the force-time responses for different deformation conditions for the two methodologies. In Figure 5.1(a), the force versus time response is shown for deformation conditions of 400, 450 and 500 °C at a strain rate of 0.5 /s. In Figure 5.1(b), the force versus time scaled by the target strain rate is shown for deformation temperature of 450 °C and strain rates of 0.1, 0.5, and 2.5 /s. The horizontal axis is time multiplied by the target strain rate so that all the curves will have similar range in horizontal axis. All the curves have similar trend. Initially both methodologies coincide, where an immediate rise in force followed by a peak and a subsequent decrease. However, the results from ML method show last longer time than the conventional ones, which will be discussed in more detail in Section 5.4. Additionally, the ML method appears to demonstrate a smoother transition post-peak and a more gradual decline in force with respect to time compared to the conventional approach, which exhibits more variations post peak.

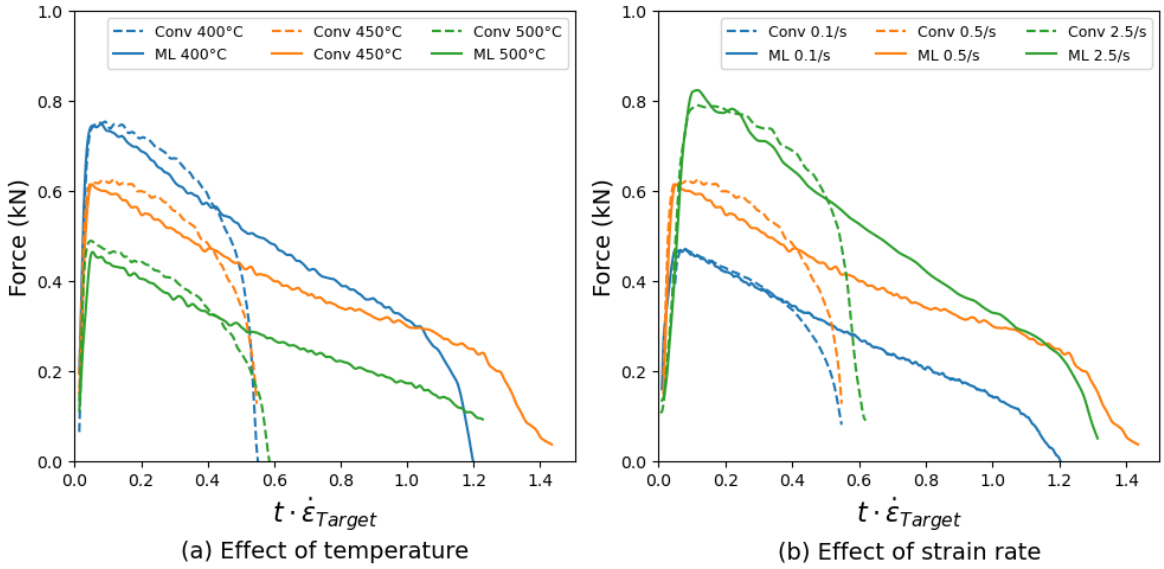


Figure 5.1 Comparison of the evolution of tensile force of aluminium alloy specimen for the conventional (dashed lines) and ML (solid lines) based on SST approaches, with sub-figures: (a) and (b), corresponding respectively to different temperature conditions (at the strain rate of 0.5 /s) and different strain rate conditions (at the temperature of 450 °C).

Figure 5.2 shows a series of force versus stroke or displacement curves for material testing at specified temperatures and strain rates. In Figure 5.2(a) the force versus displacement response is shown under constant target strain rate for the following deformation conditions 400 °C & 0.5 /s, 450 °C & 0.5 /s & 500 °C & 0.5 /s, whilst Figure 5.2(b) shows the force versus displacement response under constant deformation temperature for deformation condtions 450 °C & 0.1 /s, 450 °C & 0.5 /s, and 450 °C & 2.5 /s. The ML model generally shows a similar trend as with the conventional method, but the two cases deviate more notably as the stroke increases. This deviation suggests a difference in the applied strain and strain rate response between the predictive models, particularly at higher degrees of deformation.

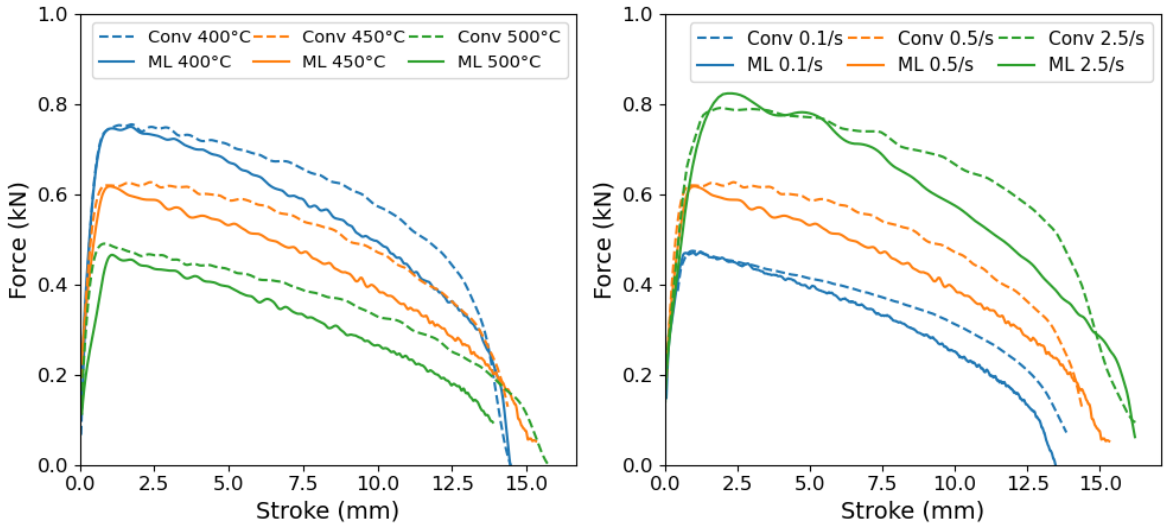
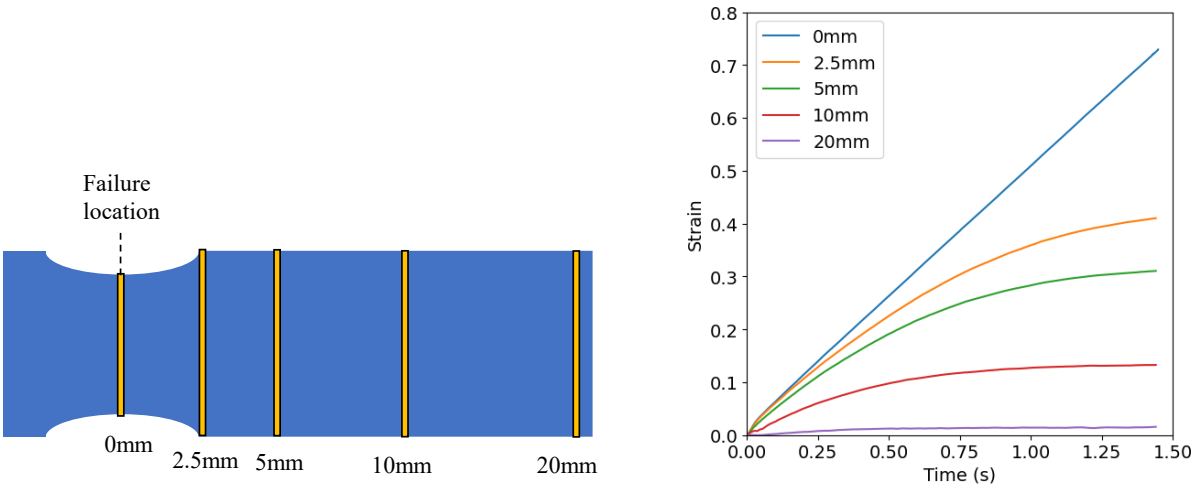


Figure 5.2 Comparison of the force versus displacement of an aluminium alloy tensile specimen for the conventional and ML based SST approach, with sub-figures: (a) and (b) corresponding respectively to different temperature conditions (at the strain rate of 0.5 /s) and different strain rates (at the temperature of 450 °C).

5.3 Strain distribution and evolution

A temperature gradient exists within the test piece, which leads to a non-homogeneity of strain along the test piece even before necking occurs. This means that the deformation is more localised than it would be under a homogeneous deformation with constant temperature. Figure 5.3 shows a schematic how the data are collected from the specimen. Using DIC and applying sections are shown at 0, 2.5, 5, 10 and 20 mm from the failure point in Figure 5.3(a). For each section the arithmetic average of strain is calculated from the point that lie on that cross section within the GOM Correlate inspect tool [127] as illustrated by the yellow lines in Figure 5.3(a). The deformation for condition 450 °C & 0.5 /s is shown in Figure 5.3(b). As can be seen, the further away from the fracture location, the lower the average strain. The difference increases more with the progress of testing.



(a) Schematic of section positions (b) Average strain at selected positions

Figure 5.3 Different positions (0, 2.5, 5, 10 and 20 mm from the fracture location) and the calculated average strain from the corresponding sections.

The ML predicted displacement-time results were employed to perform Gleeble uniaxial tensile tests. Figure 5.4 shows the strain field from the experimental tests, including 400 °C & 0.5 /s, 450 °C & 0.1 /s, 450 °C & 0.5 /s, 450 °C & 2.5 /s, and 500 °C & 0.5 /s. In each case, the plots are shown at increasing normalised times of 0.2, 0.4, 0.6, 0.8 and 0.95. The strain starts at a broader distribution at the beginning of deformation, but the strain peak becomes sharper and more localised as the time increases. Figure 5.4 demonstrates the impact of deformation temperature and target strain rate on the distribution of true strain across the specimens. Similar to the characteristic behaviour observed in the cases using conventional control, the strain distribution shows a strong symmetry about the centre. Increasing the target strain rate or decreasing the deformation temperature led to a broader strain distribution, indicating that the distribution becomes slightly more uniform.

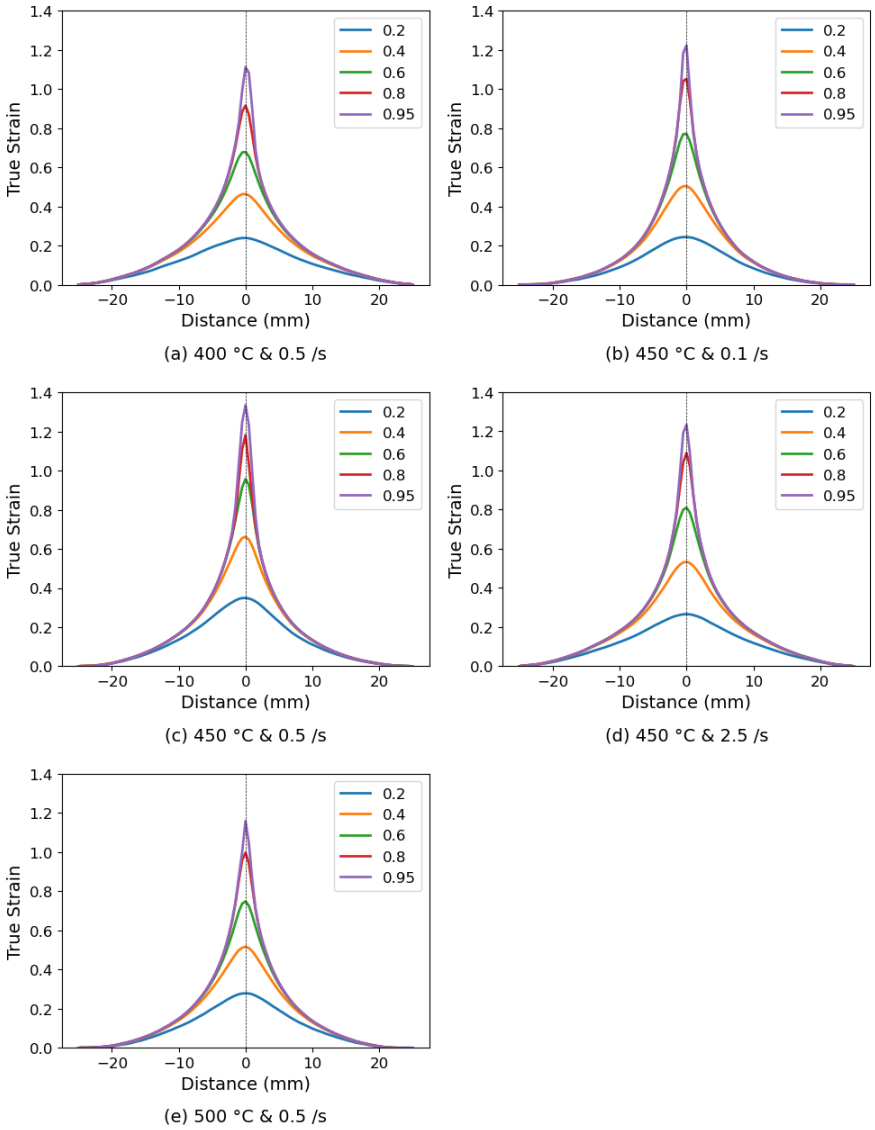


Figure 5.4 True strain distribution across the aluminium alloy specimen centred at the failure point, as captured by DIC, at t/t_f = 0.2, 0.4, 0.6, 0.8 and 0.95 under the ML based approach. Each sub-figure, (a) to (e), corresponds to a different temperature and strain rate combination.

Figure 5.4 demonstrates the impact of deformation temperature and target strain rate on the distribution of true strain across a material specimen. As the target strain rate increases or the deformation temperature decreases, the strain distribution tends to become broader, indicating more uniform plastic deformation. Conversely, higher temperatures and lower strain rates result in sharper peaks, which could indicate a more localised deformation.

In Table 5.1, the characteristics of the strain field at a strain of 0.5 are quantified, assessing the impact of deformation temperature and target strain rate on key statistical measures. The table details the effects on the maximum strain, range, mean, standard deviation, skewness, and

kurtosis, under varying conditions of forming temperature and strain rate. These parameters provide insights into the distribution of strain in the specimen under different deformation temperatures and target strain rate. The mean μ, standard deviation SD, skewness $SKEW$ and kurtosis K are calculated respectively from the strain distribution as:

$$\mu = \frac{1}{N}\sum_{i=1}^{N} x_i \tag{5.1}$$

$$SD = \sqrt{\frac{1}{N}\sum_{i=1}^{N}(x_i - \mu)^2} \tag{5.2}$$

$$SKEW = \frac{1}{(N-1)}\sum_{i=1}^{N}\left(\frac{x_i-\mu}{SD}\right)^3 \tag{5.3}$$

$$K = \frac{1}{N}\sum_{i=1}^{N}\left(\frac{x_i-\mu}{SD}\right)^4 \tag{5.4}$$

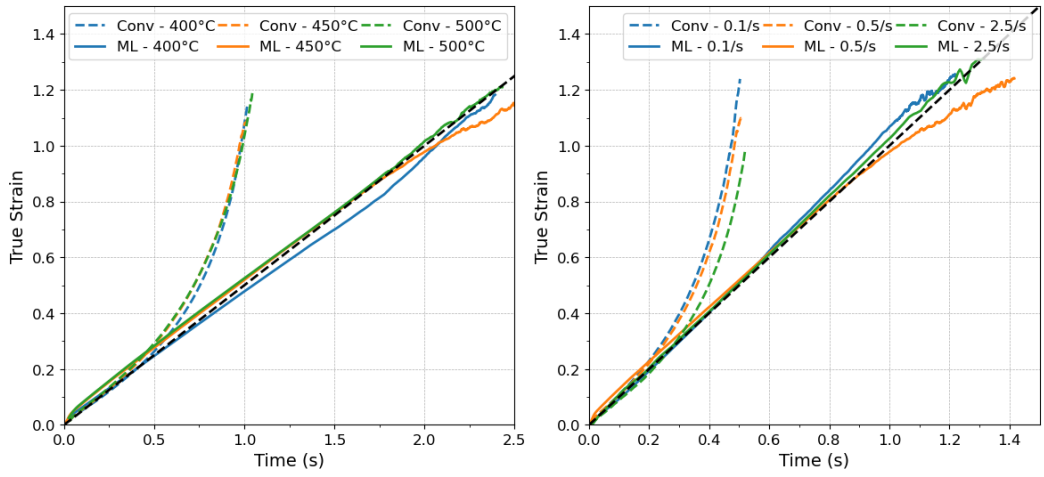
Table 5.1 effects of deformation temperature and target strain on standard deviation and mean of the strain field, at strain of 0.5.

Forming temp and strain rate $T, \dot{\varepsilon}_{\text{Target}}$	Mean μ	Standard Deviation SD	Skewness $SKEW$	Kurtosis K
400 °C, 0.5 /s	0.20	0.15	0.65	-0.87
450 °C, 0.1 /s	0.17	0.16	0.76	-0.71
450 °C, 0.5 /s	0.18	0.15	0.65	-0.81
450 °C, 2.5 /s	0.20	0.15	0.66	-0.81
500 °C, 0.5 /s	0.18	0.15	0.76	-0.70

The standard deviation characterises the spread of the data from the mean. The skewness is a measure of the asymmetry of the distribution about its mean. Skewness determines the asymmetry of the distribution around its mean. The skewness value can be positive, zero, or negative, depending on the skew of the data. A positive or negative skewness indicates a skew towards the positive direction or negative direction respectively and a skewness of zero indicates no skewness in the data. Kurtosis, on the other hand, assesses the 'tailedness' of the distribution to the mean. The kurtosis value can be positive, zero, or negative, depending on

the shape of the data distribution. The positive values indicate a distribution with less pronounced tails and a steeper peak, and the negative values indicate a 'flatter' distribution with more pronounced tails than a normal distribution. The data shows that the mean of the strain distribution increases at lower deformation temperatures and higher strain rates. The skewness of the distribution indicates a slight skew towards the positive 'x' direction with skewness decreasing at lower deformation temperatures and higher strain rates. The kurtosis of each distribution is negative in all cases meaning that the tails of the distribution are smaller than those of a normal distribution (which has a kurtosis of zero). The data also showed that the standard deviation was largely unchanged under various deformation temperature and target strain rate employed in this study and varied for all deformation conditions between 0.15 and 0.16.

Figure 5.5 presents the experimentally obtained maximum strain, i.e. at the centre section where the failure was located for both the conventional and ML SST approach, compared with the target strain-time curves (dotted red lines). The strain versus time responses under a constant target strain rate of 0.5 /s for deformation temperatures of 400 °C, 450 °C and 500 °C are shown in Figure 5.5(a). Likewise, Figure 5.5(b) shows the strain evolutions under a constant deformation temperature of 450 °C and different strain rates of 0.1 /s, 0.5 /s, and 2.5 /s. Each curve shows a strain evolution corresponding to a different considered deformation condition of temperature and target strain rate.



(a) Effect of temperature

(b) Effect of strain rate

Figure 5.5 Comparison of the evolutions of the maximum strain at the failure location of tensile specimen for the conventional and ML based SST approach with the target strain-time line (dashed, black), with sub-figures: (a) and (b) correspond respectively to different temperature conditions (at the strain rate of 0.5 /s) and different strain rates (at the temperature of 450 °C).

In all cases, the results using ML model predictions of displacement achieve good agreement with the target value. This is particularly clear at low strain, and a small divergence can be found in some cases at later stage (e.g. in Figure 5.5(b)). Additionally, there is little difference for the results using ML approach for different testing conditions. The results demonstrate that the ML model shows the ability to handle varying temperatures and strain rates, suggesting that the ML model has learnt the temperature and strain rate related trends effectively. For conventional method, however, the strain increases as the test proceeds, initially closer to the target strain, but increasing sharply at later stage. For the conventional approach, there is some difference in the results for different temperature or strain rate and the strain localises and increases more rapidly at lower deformation temperature and lower target strain rates.

To evaluate more quantitatively evaluate the error in strain from the target value across the two approaches, Mean Absolute Percentage Error (MAPE) was calculated using the following equation:

$$\mathrm{MAPE} = \frac{1}{N_j}\sum_{i=1}^{N_j}\frac{|\varepsilon_{51}(t_i)-\varepsilon_{\mathrm{Target}}(t_i)|}{\varepsilon_{\mathrm{Target}}(t_i)} \tag{5.5}$$

where ε_{51} is the centre strain, $\varepsilon_{\mathrm{Target}}(t) = t \cdot \dot{\varepsilon}_{\mathrm{Target}}$ is the target strain with constant strain rate of $\dot{\varepsilon}_{\mathrm{Target}}$, and N_j is the number of frames in the j^{th} condition. Table 5.2 presents the MAPE values for strain from conventional and ML SST based approaches for the considered testing conditions. Overall, the ML model demonstrates a consistently far better performance across all considered deformation conditions compared to the conventional equation. The ML method consistently shows dramatically superior accuracy for the target strain, with the ML approach giving MAPE reductions ranging from 68.8% to 93.4% compared to the conventional method.

Table 5.2 MAPE between the target strain and achieved true strain for both the ML and Conv based SST.

MAPE	400°C&0.5/s	450°C&0.1/s	450°C&0.5/s	450°C&2.5/s	500°C&0.5/s
Conv	0.38	0.36	0.34	0.39	0.38
ML	0.048	0.031	0.11	0.026	0.044
Reduction	87.5%	91.2%	68.8%	93.4%	88.2%

5.4 Strain rate evolution

Strain rate was processed from the strain results using a Savitzky–Golay filter with polynomial order of two and appropriate window size for suitable smoothing [128]. Figure 5.6 shows the true strain rate versus normalised time under different deformation conditions. In Figure 5.6, the dashed red lines indicate the different constant target strain rates that were intended to achieve. As can be seen, the obtained strain rates from ML model prediction show almost constant values, which closely match the target strain rates. It is noted that some deviation occurs towards the end of test, possibly due to the necking effect. In contrast, the strain rates in the conventional approach are not constant and the discrepancy is sharply increased (exponentially) from about 0.4 normalised time. The maximum actual strain rates reached about 5-7 times the target strain rate, which clearly is not satisfactory for intended constant strain rate tests.

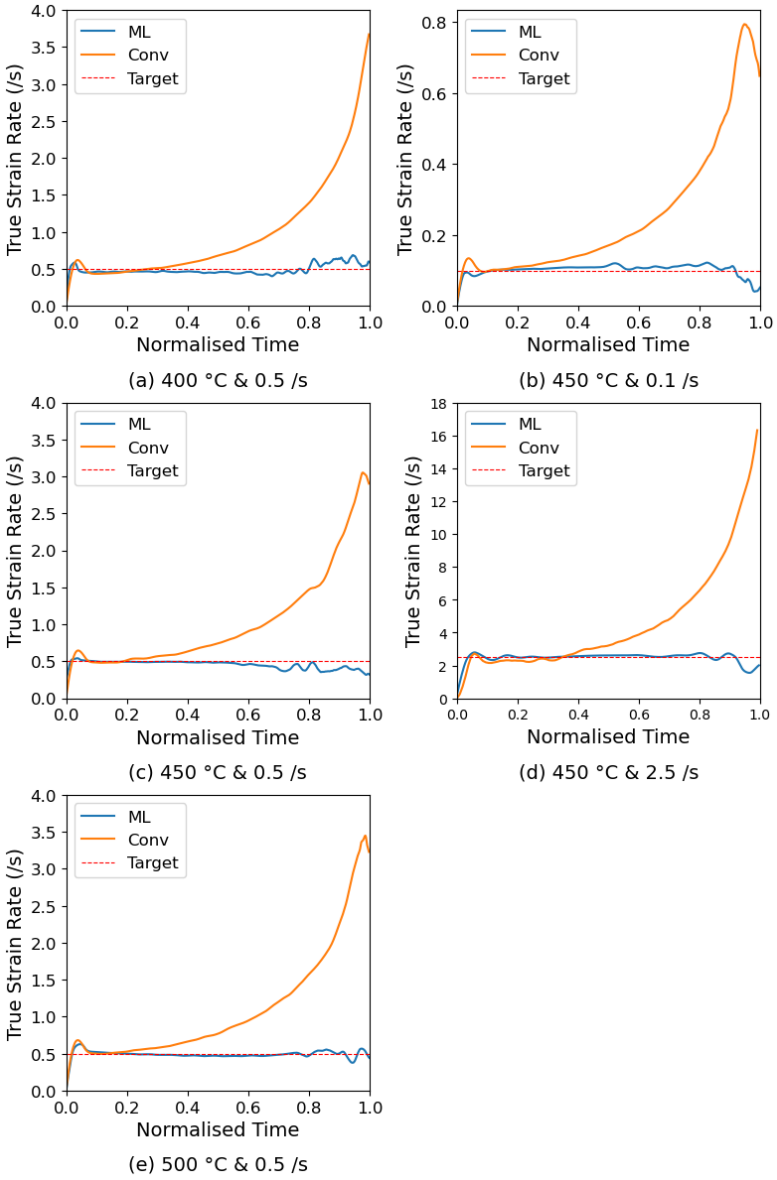


Figure 5.6 Comparison of the evolution of normalised maximum strain rate at the failure location of aluminium alloy tensile specimen for the conventional and ML SST approach, against the target strain-time plot, with sub-figures: (a) to (e) corresponding to a different temperature and strain rate condition.

To evaluate quantitatively evaluate the differences in strain rate from the target value, MAPE is calculated for each approach, using the following equation:

$$\text{MAPE} = \frac{1}{N_j}\sum_{i=1}^{N_j}\frac{|\dot{\varepsilon}_{51}(t_i) - \dot{\varepsilon}_{\text{Target}}|}{\dot{\varepsilon}_{\text{Target}}} \tag{5.6}$$

Table 5.3 compares the MAPE results of strain rate between the conventional and ML methods for the considered deformation conditions. The maximum MAPE for ML based approach is 0.11 or 11%, while that for the conventional approach is over 100% and the maximum is 138%.

The ML based SST shows reductions of MAPE ranging between 91.3% to 94.1%, demonstrating the great improvement and the contribution that the ML approach can make to achieve constant strain rate control for Gleeble thermomechanical testing.

Table 5.3 MAPE between the target strain rate and achieved true strain rate for both the Conv and ML based SST.

MAPE	400°C&0.5/s	450°C&0.1/s	450°C&0.5/s	450°C&2.5/s	500°C&0.5/s
Conv	1.36	1.38	1.25	1.21	1.31
ML	0.091	0.082	0.11	0.089	0.082
Reduction	93.3 %	94.1 %	91.4 %	92.7 %	93.7 %

Figure 5.7 demonstrates the impact of deformation temperature and target strain rate on the distribution of strain rate across the specimens, showing the strain rate fields from the experimental tests under 400 °C & 0.5 /s, 450 °C & 0.5 /s, 500 °C & 0.5 /s, 450 °C & 0.1 /s and 450 °C & 2.5 /s. In each case, the plots are shown at increasing normalised times of 0.3 0.5, 0.7 and 0.9. The figure shows no significant impact of deformation temperature and target strain rate on the distribution of true strain rate across the specimens. Like the characteristics of the strain field distribution, the strain rate also has a reasonably symmetrical distribution, with the maximum value at the centre of the failure location. At the centre of the failure location, the strain rate is very closely controlled to the target strain rate indicated by the dashed line. However, as distance from the failure location increases, the achieved strain rate reduces significantly.

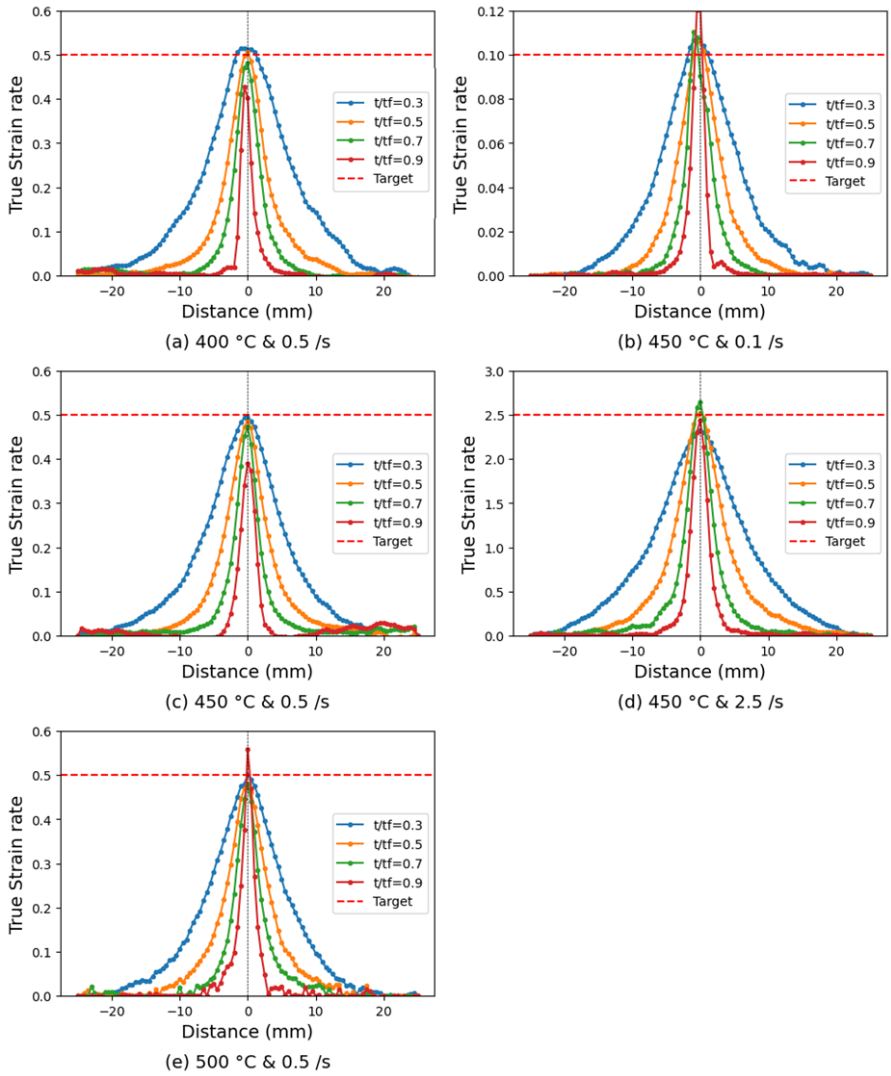
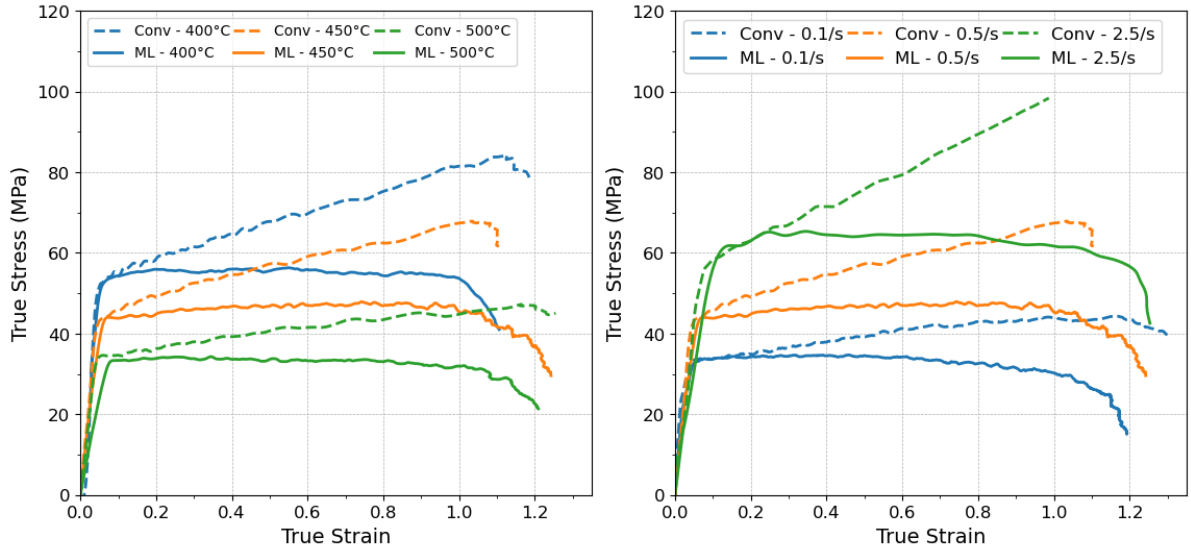


Figure 5.7 Strain rate distribution across the aluminium alloy specimen centred at the failure point, as captured by DIC, at t/t_f = 0.3, 0.5, 0.7, and 0.9 under the ML based SST approach.

5.5 Stress-strain behaviour

Figure 5.8 shows the true stress-true strain curves of AA6082 under different HFQ conditions. This is with Figure 5.8(a) for deformation temperatures of 400 °C, 450 °C, and 500 °C under the constant target strain rate of 0.5 /s and Figure 5.8(b) for the strain rate of 0.1 /s, 0.5 /s, and 2.5 /s under the constant deformation temperature of 450 °C. Each figure consists of the true stress-strain curves with the strain rate control from both the ML model and the conventional method. In both approaches, the material's flow stresses decrease with increasing deformation temperature and decreasing target strain rate. This is related to the strain rate hardening behaviour and thermal softening behaviour. The most striking effect is the difference between the flow stresses from the two approaches. There is a strong dependence on the approaches, to

such an effect that the shape of the flow stress curves has been changed. The ML model shows limited strain hardening while the conventional method exhibits a strong hardening behaviour for testing conditions. The latter can be attributed to the strain rate increase during the tests. As shown in Figure 5.6, the strain rate in conventional method increases continually, eventually exceeding the target strain rate by up to 600%. Therefore, the hardening behaviour exhibited by the conventional method is largely attributed to the strain rate increasing. A hardening of between 20-50 MPa during plasticity was exhibited for the conventional based method of strain rate control and a hardening of less than 10 MPa was exhibited for the ML based method of strain rate control. For a deformation temperature of 400 °C and target strain rate of 0.5 /s the hardening percentage reduction between the two methods was over 400%.



(a) Effect of temperature

(b) Effect of strain rate

Figure 5.8 Comparison of true stress-strain curves obtained from the average over the cross section at the failure location, for the Conventional and ML SST approaches, for (a) different temperatures at a constant strain rate of 0.5 /s and (b) different strain rates under a constant temperature of 450 °C.

True stress-strain curves are critical to understand the evolution of material strength during deformation. They are also important for calibrating material constants for constitutive modelling which plays more and more importance in research and practice. Inaccurate material data will lead to inaccurate model and its prediction, which could have serious effect in application. As shown above, the proposed data-driven deep learning tensile testing significantly improves the strain rate control and has the potential to produce reliable material data, leading to improved safety and efficiency in various industries. The architecture used in

this study relies on the analysis of the conventional data characteristics, where the strain distribution shows minimal dependence on both testing temperature and strain rate. The methodology introduced in this study allows future work to be carried out, expanding the applicability of this approach to a broader range of materials and complex loading conditions.

5.6 Effect of strain rate on stresses and ductility

Figure 5.9 shows the flow stresses at different strain levels under a constant deformation temperature of 450 °C at different target strain rates for both the conventional and ML based approaches. The symbols represent the measured values, and the lines are fitted trend lines. The fitting is done based on the following power law relationship describing strain rate hardening:

$$\sigma = K'\dot{\varepsilon}^m \tag{5.7}$$

where σ and $\dot{\varepsilon}$ are respectively the stress and the strain rate, K' is a constant and m is strain rate sensitivity factor. A linear fit is achieved between logarithm flow stress and logarithm target strain rate. Owing to the logarithmic axes, the intercept at y-axis gives $\log(K')$ and the gradient give the strain rate sensitivity factor m. Fitting is performed using the least squares method [129] to optimise the coefficients.

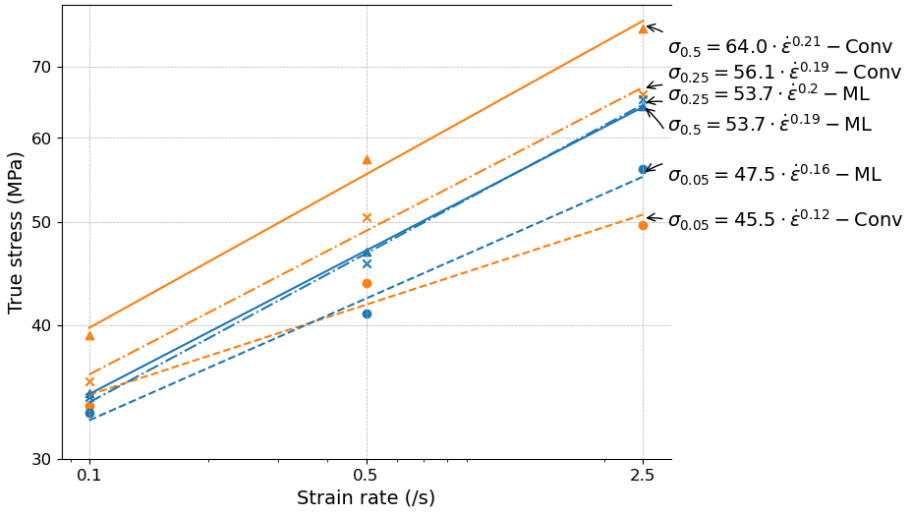


Figure 5.9 Flow stresses at different specific strain levels for the deformation temperature of 450 °C and different target strain rates with the ML and conventional approaches, showing a good linear fitting and the fitted equation. σ_ε denotes the true stress at a strain level of ε, i.e. 0.05, 0.25 and 0.5.

For the ML approach, K' and m vary between 47.5 – 53.7 MPa and 0.16 - 0.20 respectively. However, a much larger variation is seen in K' and m between 45.5 – 64.0 MPa and 0.12 – 0.21 respectively for the conventional approach. The results show that the line of best linear fit has much better agreement to datapoints for the machine learning based approach. This could be attributed to the small difference between the target strain rate and practically achieved strain rate for the ML based approach. For example, the maximum MAPE in strain rate for ML approach is only 11%, whilst the conventional approach had a MAPE of over 100%, indicating a large error introduced, particularly later in the deformation.

Theoretically, for a material at a certain temperature, K' and m should be constant. However, because Equation (5.7) does not include the effects of strain hardening, K' increases with increasing level of plasticity. To account for the different amounts of strain and strain rate hardening, the Johnson-Cook or N-H model or other unified constitutive equations can be considered, which incorporate strain, strain rate hardening and thermal softening effects and other effects into one unified equation.

Figure 5.10 shows the percentage elongation measured within GOM correlate at failure over a gauge length of 20 mm at a constant deformation temperature of 450 ^{o}C and different target strain rates for the conventional and ML based approaches. All elongation results are within 60-70%. For ML based approach, the elongation increases slightly with increasing target strain rate, while the conventional approach shows a peak at intermediate strain rate of 0.5 /s. A similar trend, with increasing ductility at lower strain rates and decreasing ductility at higher strain rates, has been reported by other researchers [130].

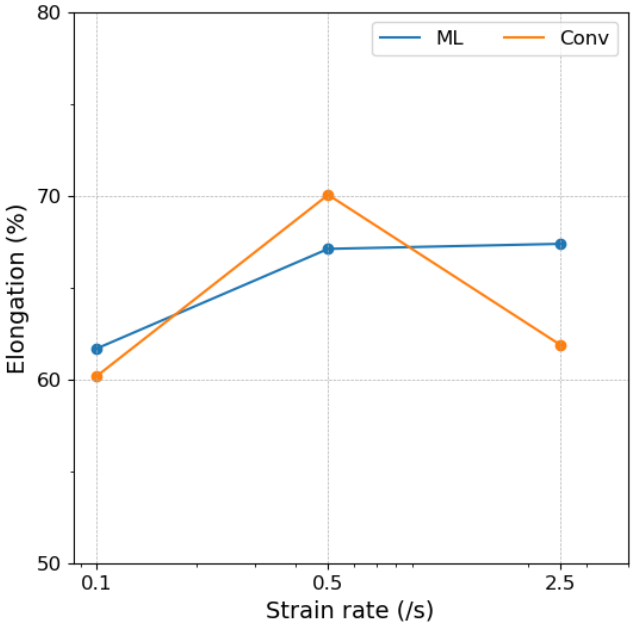


Figure 5.10 Percentage elongation at different target strain rates for constant deformation temperature of 450 ºC over the ML and conventional approaches.

It is reported that at elevated temperatures the ductility is highly strain rate sensitive. The strain rate affects ductility due to dynamic recovery and recrystallisation, sliding and rotation of grain boundary, etc [26]. These complex microstructural phenomena may have contributed to the observed initial increase followed by a decrease in elongation in Figure 5.10.

5.7 Effect of temperature on stresses and ductility

Figure 5.11 illustrates the true stress response of the material at varying temperatures for three different strain amounts (ε of 0.05, 0.25, and 0.5), tested through both conventional and ML method. As the temperature increases from 400°C to 500°C, there is a noticeable decrease in the true stress across all strain values for both methods, as shown in Figure 5.8(a). This decrease is known to be attributed to enhanced thermal vibrations within the microstructure, which

increase diffusion and dislocation mobility, thus reducing the flow stress necessary to overcome activation barriers [131].

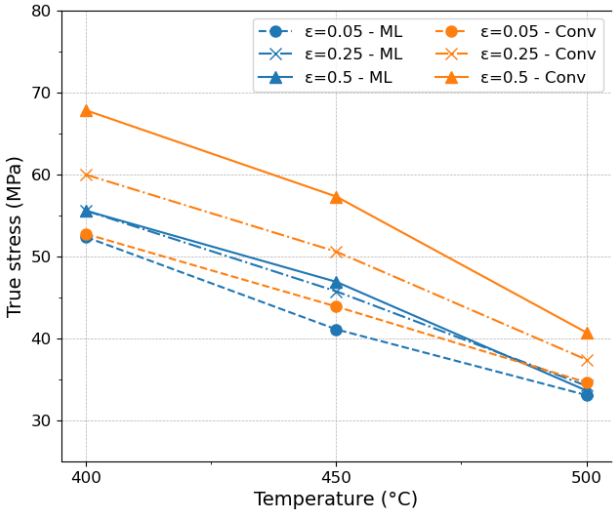


Figure 5.11 Flow stresses at different specific strain levels under different deformation temperature for a constant target strain rate of 0.5/s using the ML and Conventional approaches.

The machine learning approach exhibits a tighter data spread compared to the conventional method, particularly noticeable at higher strains. This can again be attributed to the superior strain rate control through the ML method, which produces a more uniform stress response. Over the tested temperature range of 100 °C, the ML approach at a strain level of 0.5 shows a lower flow stress by approximately 10-20 MPa compared to the conventional method.

Similarly, in Figure 5.12, the logarithmic stress is plotted against inverse temperature at various strain levels at different deformation temperatures of 400 °C, 450 °C and 500 °C. At constant strain level and strain rate, the stress can be calculated with the Norton-Hoff (N-H) equation [132]:

$$\sigma = K'' \exp\left(\frac{Q}{R_g T}\right) \tag{5.8}$$

where K'' can incorporate strain and strain rate hardening effects, Q is the activation energy, T is the absolute temperature, and R_g is the ideal gas constant. A linear fit is achieved between logarithm flow stress and inverse temperature in Kelvin. Owing to the logarithmic axis, the

intercept at the y-axis gives $\log(K'')$ and the gradient gives Q/R_g. Fitting is performed using the least squares method [129] to optimise the linear fit to each set of three datapoints.

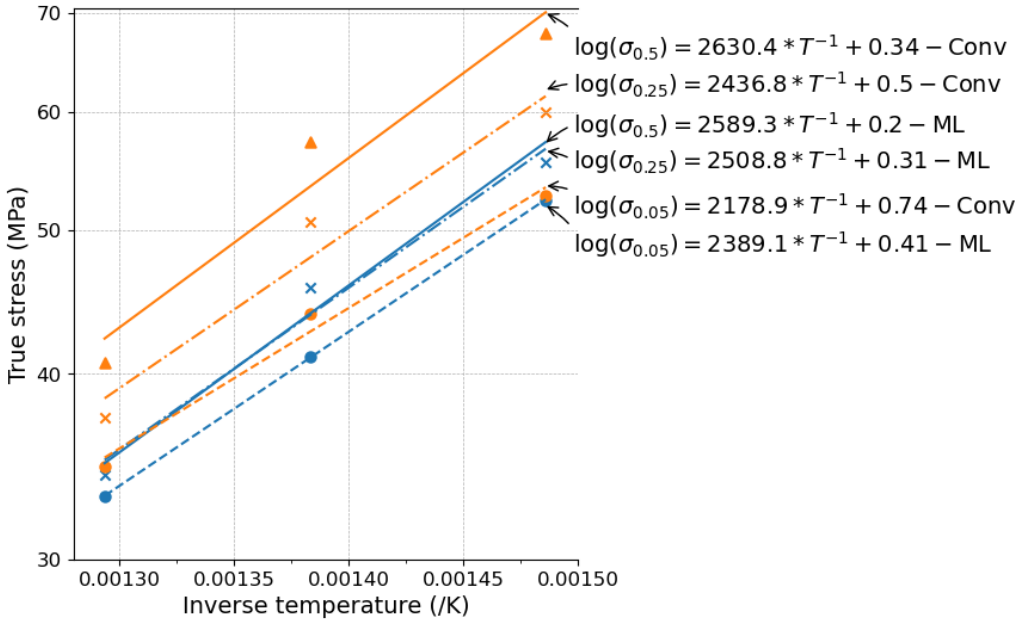


Figure 5.12 Flow stress versus inverse temperature for a constant target strain rate of 0.5 /s from the ML and Conventional approaches. This is with σ_ε denoting the true stress at a particular strain level of ε, i.e. 0.05, 0.25 and 0.5.

Figure 5.12 indicates the suitable of the N-H equation to the stress strain behaviour where very close to linear fit was obtained between the datapoints using logarithmic y-axis. It should be noted that better linear fit is obtained for the machine learning approach, in comparison to the conventional approach where a slightly divergence is found especially at lower temperatures. The fitted Q values are 18.1, 20.3, and 21.9 kJ/mol respectively for ML approach at strains of 0.05, 0.25 and 0.5; and 19.9, 20.9, and 21.5 kJ/mol respectively for Conventional approach at 0.05, 0.25, and 0.5. The improved consistency is due to more constant strain rate control during testing using ML-based approach.

Figure 5.13 shows the percentage elongation at failure over a gauge length of 20 mm centred at the failure location at a target strain rate of 0.5 /s under different deformation temperatures. A trend of slightly increasing ductility with elevated temperatures is found over the considered deformation temperature range of 400 - 500 °C in both approaches.

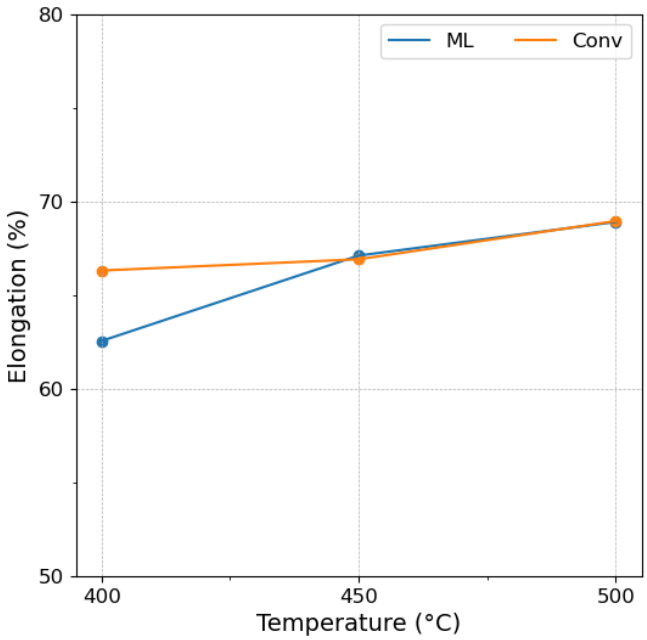


Figure 5.13 Elongation for 20 mm gauge length at different temperatures, for the ML and conventional approaches, for a target strain rate of 0.5 /s.

At higher deformation temperatures, the increase in ductility during a hot tensile test is generally attributed to the enhanced sliding and rotation of grain boundary and microstructural recovery [133]. These mechanisms contribute to the test pieces' ability to undergo large plastic deformation without fracture, resulting in the increased ductility at higher temperatures.

The thermomechanical data for AA6082 is summarised in Table 5.4 for all testing conditions in this study for the ML based approach. The effect of temperature and strain rate on the stress and elongation have been analysed and discussed above. In the following, the strain ratio β and Lankford coefficient R will be elaborated.

Table 5.4 Summary of the mechanical properties of the AA6082 test piece under the different considered deformation condition for the ML approach.

Deformation temp and strain rate $T, \dot{\varepsilon}_{\text{Target}}$	Stress $\sigma_{0.05}$ (MPa)	Stress $\sigma_{0.5}$ (MPa)	Elongation over 20 mm gauge (%)	Strain ratio β	Lankford coefficient R
400 °C, 0.5 /s	52.3	55.5	65.3	-0.38	0.61
450 °C, 0.1 /s	33.1	34.5	61.7	-0.39	0.63
450 °C, 0.5 /s	41.1	46.9	67.5	-0.36	0.57
450 °C, 2.5 /s	56.0	64.2	67.4	-0.35	0.54
500 °C, 0.5 /s	33.1	33.6	68.6	-0.38	0.61

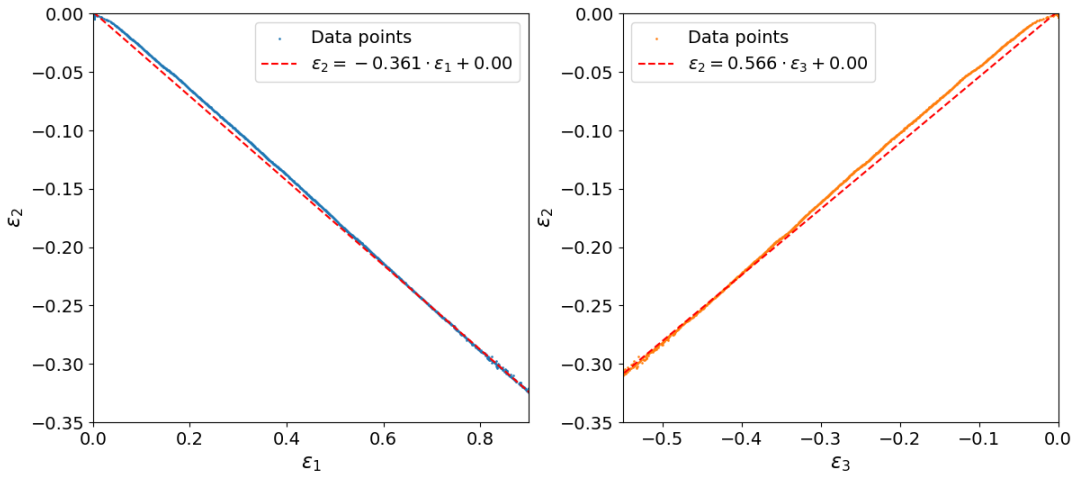
In Table 5.4, the results of strain ratio and Lankford coefficient are determined from the following equations:

$$\beta = \frac{d\varepsilon_2}{d\varepsilon_1} \tag{5.9}$$

$$R = \frac{d\varepsilon_2}{d\varepsilon_3} \tag{5.10}$$

where ε_1 is the longitudinal strain in the tensile direction obtained from the average over the section at the failure location, ε_2 is the transverse strain along the width of the specimen and ε_3 is the thickness strain along the thickness direction. It should be noted that ε_3 is assumed to satisfy the equation $\varepsilon_1 + \varepsilon_2 + \varepsilon_3 = 0$ under the assumption of volume conservation where the volume strain is zero. These two parameters help to assess the degree of anisotropy introduced by the rolling. Numerically, the strain ratio β and Lankford coefficient R are determined by determining a linear fit between the strains in different direction $[\varepsilon_1, \varepsilon_2]$ and $[\varepsilon_3, \varepsilon_2]$ respectively. This means that the fitted gradient gives β and R. This is illustrated in Figure 5.14 for deformation temperature of 450 °C and the target strain rate of 0.5 /s. In both Figure 5.15(a) and (b), a very good linear fit is obtained to the experimental average strain data over each cross section in the different directions, suggesting that very little variation with time and deformation. Fitting is made using the least squares method [129] to optimise the coefficients. From Table 5.4, it can be seen that both the strain ratio and the Lankford coefficient are very

similar for all the test temperatures and strain rates, indicating consistent testing loading path and material normal anisotropy.



(a) Strain ratio (b) Lankford coefficient

Figure 5.14 Linear fit between the strains along the different directions at deformation temperature of 450 °C and target strain rate of 0.5 /s for the ML approach, for the determination of strain ratio and Lankford coefficient.

From the above, it is considered that the data-driven method approach, employing Long Short-Term Memory (LSTM) neural networks, is very effective in predicting the strain development and strain rate. This allows for more accurate determination of thermomechanical properties of sheet metals in metal forming applications and more reliable material models which will be discussed in the following section. These more appropriate thermomechanical constitutive properties will also provide for more realistic simulation of metal forming processes using Finite Element, e.g. ABAQUS, as well as other analysis/simulation software.

Further research is needed to explore the scalability of the ML approach to different materials, much higher strain rates and more complex loading conditions. Future studies could also examine the integration of real-time data acquisition systems in thermomechanical experiments to adjust dynamically the applied displacement, further enhancing the testing process more generally.

5.8 Viscoplastic constitutive models

Material models are widely used in predicting material behaviour under different conditions that have not been experimentally tested. In this section, the commonly adopted Norton-Hoff

model, Johnson-Cook model and an ordinary differential equation-type unified constitutive model have been selected and the data obtained above using both the conventional and machine learning approaches have been employed to determine the material constants. The results show significant differences of the model parameters from these two approaches, demonstrating the importance of reliable material data.

5.8.1 Norton-Hoff model

For a viscoplastic solid, often an appropriate method is to employ the Norton-Hoff (N-H) model [6, 65]. The model can be expressed as follows:

$$\sigma(\varepsilon, \dot{\varepsilon}, T) = K \cdot \exp(\beta/T) \cdot \varepsilon^n \cdot \dot{\varepsilon}^m \tag{5.11}$$

where σ is true stress, ε is strain, $\dot{\varepsilon}$ is the strain rate, T is the absolute temperature, K is a constant, β is a thermal activation energy dependent material coefficient, n is strain hardening exponent, and m is the strain rate sensitivity index. n and m are temperature dependent and can be described by the following [70]:

$$n(T) = n_0 \cdot \exp(-c_n \cdot (T - T_0)) \tag{5.12}$$

$$m(T) = m_0 \cdot \exp(c_m \cdot (T - T_0)) \tag{5.13}$$

Where n_0, m_0, c_n, c_m, and T_0 are constants.

One of the most difficult tasks encountered in developing viscoplastic constitutive equations is accurately determining the material constants from experimental data, valid over a range of temperatures and strain rates. The N-H viscoplastic constitutive equations give a function relationship between flow stress plastic strain, strain rate and temperature. The equation set has a total of 8 material constants: K, β, n_0, c_n, m_0, c_m, T_0**.** The experimental data sets for both the conventional approach and ML approach were used to determine the material constants arising in the constitutive equations. Numerical fitting of the parameters within the N-H model to the experimental data is performed using a nonlinear least squares fitting using the Levenberg-Marquardt algorithm [134, 135]. Multiple initial guesses for the parameters were tested to minimise the risk of the optimisation being trapped in local minima, ensuring confidence in the obtained global optimal solution.

Figure 5.15 and Figure 5.16 show the fitted N-H model results of the stress-strain relation in comparison with the experimental results respectively for the conventional and machine learning based approaches. The determined material constants are given in Table 5.5. As shown in Figure 5.15 and Figure 5.16, both determined models demonstrate a good agreement between the model predictions and experimental results (symbols) for three different strain rates at a deformation temperature of 450 °C and different deformation temperatures for a strain rate of 0.5 /s respectively. This observation indicate that both sets of data can be fitted with the N-H model. However, because of the large divergence between the target strain rate and applied strain rate in the conventional method of strain rate control, the hardening behaviour and stress strain behaviour are different, leading to large differences in the numerically determined material constants between the models for the conventional and ML results. The differences between the constants are calculated in percentage and presented in Table 5.5, with the largest difference reaching 64% for n_0 which determines the strain hardening exponent, indicating the severe overestimation of hardening from the conventional approach.

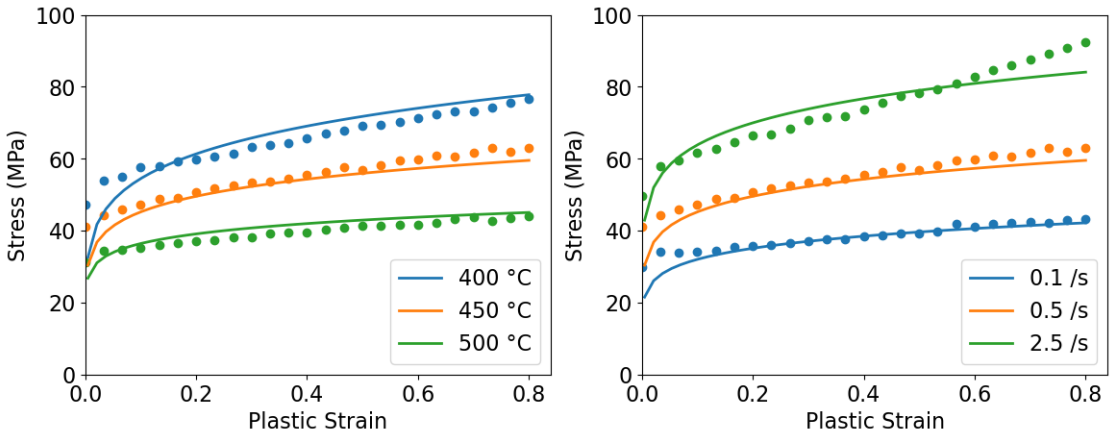


Figure 5.15 Stress-strain relationships for the conventional method with: (a) different temperature and (b) different strain rate.

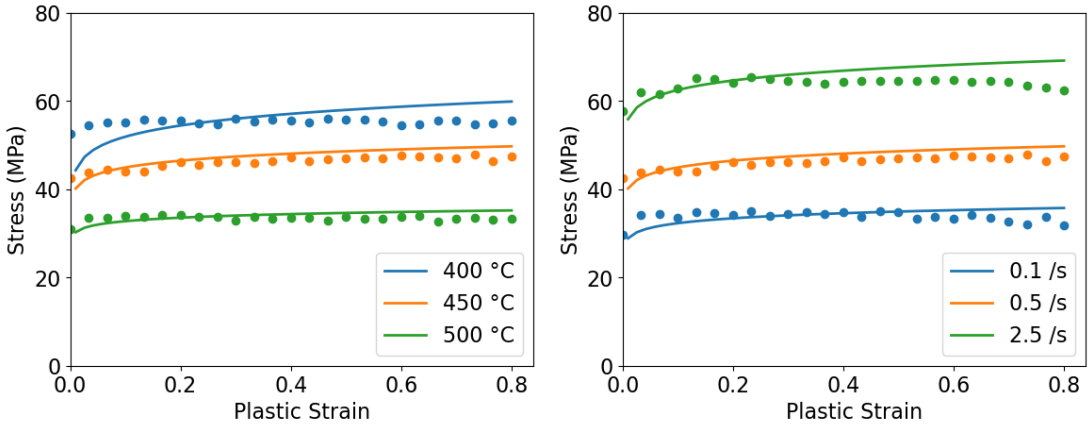


Figure 5.16 Stress-strain relationships for the ML approach with: (a) different temperature and (b) different strain rate.

Table 5.5 Fitted parameters of the N-H model based on ML and conventional displacement time relationships.

Parameter / SST method	K (MPa)	β (K)	n_0 -	c_n (/K)	m_0 -	c_m (/K)	T_0 (K)
conv	13.2	0.35	0.0051	0.024	0.011	757.9	261.8
ML	15.5	0.19	0.0069	0.0032	0.021	954.9	252.0
PD %	-14.6%	83.2%	-25.3%	644.0%	-44.6%	-20.6%	3.9%

5.8.2 Johnson-Cook model

The Johnson-Cook constitutive models are a form of viscoplastic constitutive equations which give a function relationship between flow stress plastic strain, strain rate and temperature. Johnson and Cook [136] proposed these constitutive relationships in the 1980s and they have found wide application. They exhibit a simple form and cover the physical effects of strain hardening, strain rate hardening and temperature softening as follows [71]:

$$\sigma(\varepsilon, \dot{\varepsilon}, T) = [A + B\varepsilon^n][1 - T^*]^m[1 + C\ln(\frac{\dot{\varepsilon}}{\dot{\varepsilon}_0})] \tag{5.14}$$

$$T^* = \frac{T - T_0}{T_{max} - T_0} \tag{5.15}$$

where T^* is the homologous temperature. The Johnson-Cook equation set has a total of 8 material constants: A, B, n, C, m, $\dot{\varepsilon}_0$, T_m and T_0, which need be determined from the experimental stress strain behaviour of the material. In the J-C Johnson-Cook equation, A is the initial stress, B is the hardening constant, n is dimensionless hardening exponent, C and m are dimensionless model parameters related to strain rate hardening and thermal softening, and T_0 and T_m are the reference temperature and material melting temperature.

The stress-strain data obtained from Gleeble tests using both the conventional and ML-based approaches for displacement control are used to calibrate the material constants for the Johnson-Cook model. The determined constants are listed in Table 5.6. Figure 5.17 and Figure 5.18 shows the comparison of the modelled stress-strain curves against the experimental data for the conventional and machine learning based results. Both models demonstrate a good agreement between the model predictions and experimental results (symbols) for three different strain rates at a deformation temperature of 450 °C, and different deformation temperatures for a strain rate of 0.5 /s respectively. However, similar to the N-H model situation, because of the large divergence between the target strain rate and actually achieved strain rate in the conventional method of strain rate control, the determined material constants for the two approached differ significantly. Again, the largest difference of 791% occurs for strain hardening exponent.

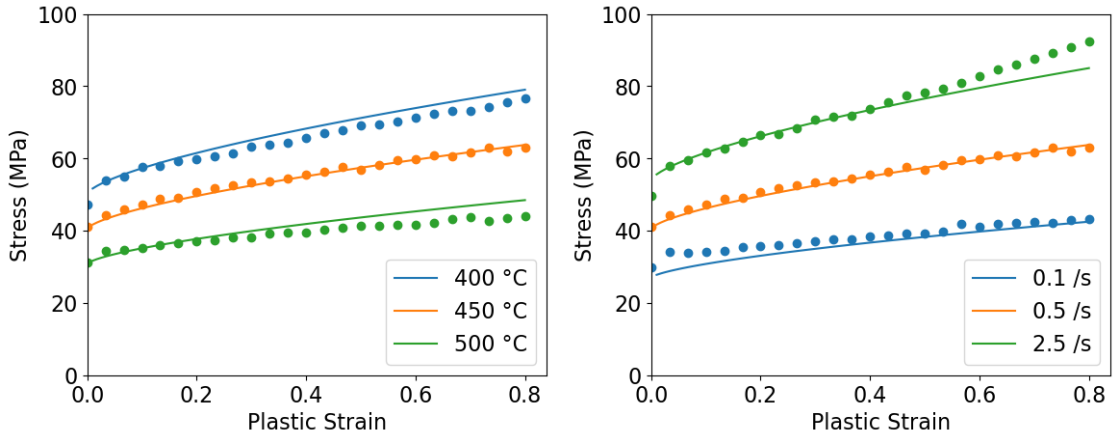


Figure 5.17 Stress-strain relationships for the conventional method with: (a) different temperature and (b) different strain rate.

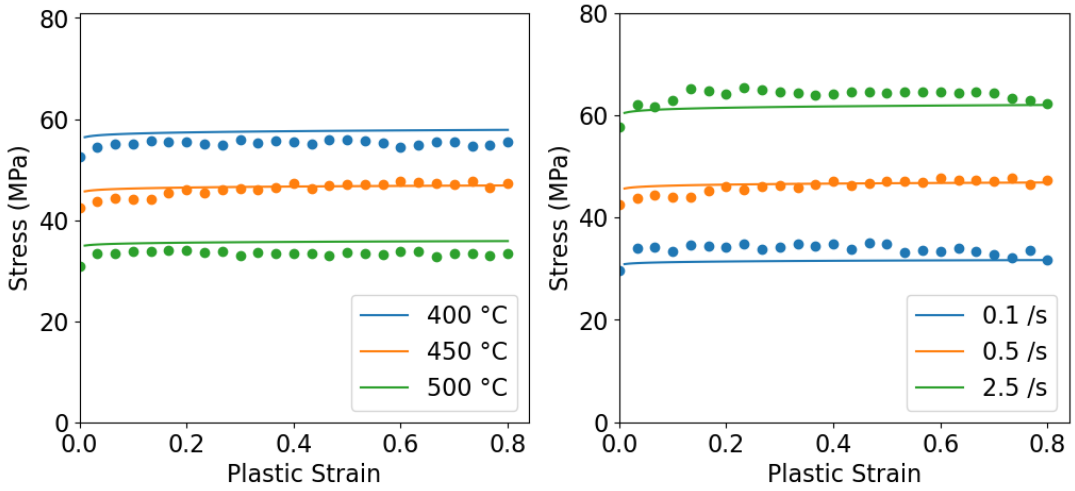


Figure 5.18: Stress-strain relationships for the ML approach with: (a) different temperature and (b) different strain rate.

Table 5.6: Fitted parameters of the JC model for ML and Conventional displacement time relationships.

Parameter / SST method	A (MPa)	B (MPa)	n -	C -	$\dot{\varepsilon}_0$ (/s)	m -	T_m (°C)	T_0 (°C)
conv	48.03	32.09	0.67	0.33	0.08	1.00	261.40	261.4
ML	55.61	5.51	0.08	0.30	0.09	1.00	662.88	249.9
% Difference	-13.6%	482.4%	791.2%	11.1%	-11.1%	0.0%	60.6%	4.3%

5.8.3 Ordinary Differential Equation (ODE)-type unified constitutive model

In addition to the above classic models, more advanced constitutive material modelling employs Ordinary Differential Equation (ODE)-type equations to consider not only the strain-strain behaviour but also some microstructural features to provide a unified model. One such model has been reviewed in Chapter 2 for describing hot deformation behaviour of metals and is summarised here [90]:

$$\dot{\varepsilon}_{\mathrm{p}} = \left[\frac{\sigma - B\sqrt{\bar{\rho}} - k}{K}\right]_{+}^{n} \tag{5.16}$$

$$\dot{\bar{\rho}} = A(1-\bar{\rho})\dot{\varepsilon}_{\mathrm{p}} - C\bar{\rho}^{\gamma} \tag{5.17}$$

$$\dot{\sigma} = E\left(\dot{\varepsilon}_{\mathrm{T}} - \dot{\varepsilon}_{\mathrm{p}}\right) \tag{5.18}$$

where ε_{p} is the plastic strain, σ is the stress, and $\bar{\rho}$ is the normalised dislocation density. Here $\bar{\rho}$ is defined as: $\bar{\rho} = (\rho - \rho_{\mathrm{i}})/\rho_{\mathrm{s}}$ [63], where ρ_{i} is the initial dislocation density and ρ_{s} is the saturated dislocation density. Some of the material constants are temperature dependent and have the following relations:

$$k = k_0 \exp\left(\frac{Q_k}{RT}\right) \tag{5.19}$$

$$K = K_0 \exp\left(\frac{Q_K}{RT}\right) \tag{5.20}$$

$$B = B_0 \exp\left(\frac{Q_B}{RT}\right) \tag{5.21}$$

$$C = C_0 \exp\left(-\frac{Q_C}{RT}\right) \tag{5.22}$$

$$E = E_0 \exp\left(\frac{Q_E}{RT}\right) \tag{5.23}$$

In total, there are 13 material constants that need to be fitted based on the constitutive equation: $k_0, Q_k, K_0, Q_K, B_0, Q_B, C_0, Q_C, E_0, Q_E, n, \gamma$ and A.

For the constitutive relationships described above, accurately determining the material constants from experimental data for appropriate temperatures and strain rates is a key task in characterising the model. The viscoplastic constitutive equations consist of a set of non-linear ordinary differential equations. For an ODE-type unified viscoplastic constitutive equations, numerical integration is needed to solve the equations. The experimental data set obtained earlier in this chapter were used to determine the material constants arising in the unified constitutive equations.

The procedures for determining the parameters of the model or material constants can be summarised into three steps:

1. Fit the ODE model to experimental data at a deformation temperature of 450°C, using different target strain rates (0.1 /s, 0.5 /s and 2.5 /s). This determines the strain rate-dependent parameters while keeping temperature constant.

2. Fit the model to data at a fixed target strain rate of 0.5 /s and different deformation temperatures (400°C, 450°C, and 500°C) to determine the temperature-dependent parameters. The strain rate-dependent parameters are kept constant from Step 1.
3. Use the temperature dependent equations for constants to calculate the coefficients and activation energies for the temperature dependencies, based on the values obtained from Steps 1 and 2.

Table 5.7 presents the fitted parameters of the above ODE type Equation Set for the stress - strain curves for both the machine learning and conventional methods of strain rate control. Figure 5.19 and Figure 5.20 show the comparison of experimental and modelling results respectively for the conventional and machine learning based results. Both figures demonstrate a good agreement between the model predictions and experimental results (symbols) for three different strain rates at a deformation temperature of 450 °C, and different deformation temperatures for a strain rate of 0.5 /s respectively. Clearly, as discussed before, the conventional strain rate control method produces an increasing strain rate as the test progresses, leading to overestimation of the strain hardening and different hardening behaviour from the machine learning method.

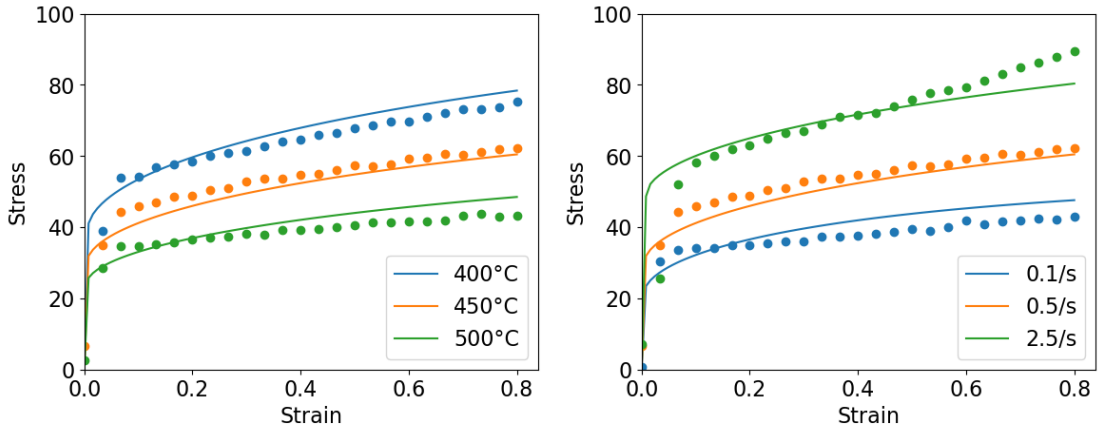


Figure 5.19 Stress-strain relationships for the conventional method with: (a) different temperature and (b) different strain rate.

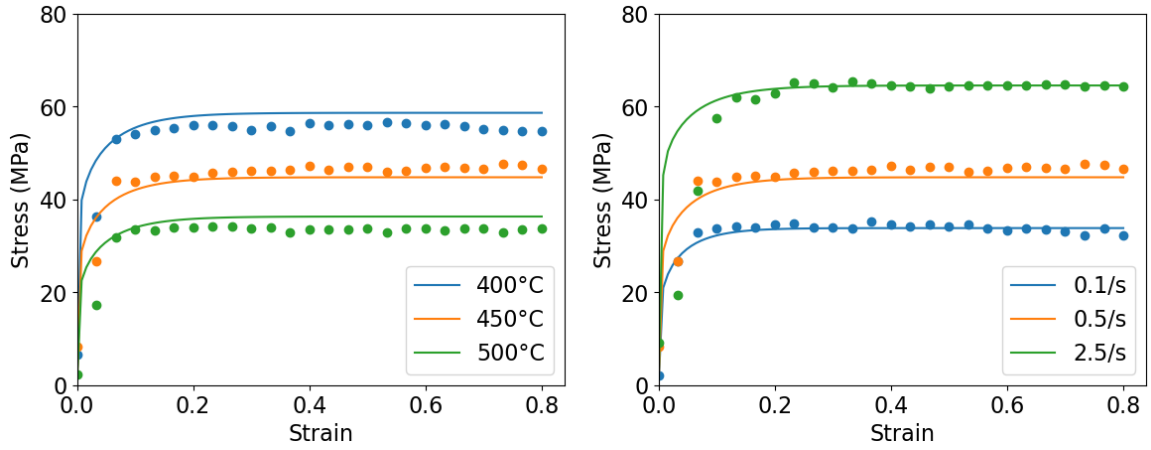


Figure 5.20 Stress-strain relationships for the ML approach with: (a) different temperature and (b) different strain rate.

Table 5.7 Fitted parameters of the ODE type Equation Set 1 model for ML and conventional displacement time relationships.

value / SST method	Q_k (J/mol)	Q_K (J/mol)	Q_B (J/mol)	Q_C (J/mol)	Q_E (J/mol)	A -	γ_0 -	n -
	k_0 (MPa)	K_0 (MPa)	B_0 (MPa)	C_0 (/s)	E_0 (MPa)			
conv	11900	28500	19400	11300	11800	0.321	1.00	2.10
	2.46	0.162	2.51	0.53	782			
ML	5240	39400	12100	5430	12700	14.2	1.00	2.01
	3.48	0.0283	2.99	1.15	554			

It should be noted that, the fitted parameters within Table 5.7 for the conventional and ML approaches, in some cases, show very large variation. This indicates that the strain rate control plays a significant role in the value of the fitted parameters. Additionally, because the equations assume constant applied strain rate and for the conventional approach the strain rate exceed the target value significantly, the fitted parameter are in error. The machine learning approach avoid this by achieving near constant strain rate, indicating that the parameters reflect better the physical meaning of the different parameters of the model.

Comparing all the three models, it is found that the ODE-type unified constitutive equations can present better fitting to the experimental results. Although more material constants are used and fitting is more complex, the unified constitutive model can more accurately predict the material flow stress behaviour.

Figure 5.21 shows two bar charts comparing the Mean Absolute Percentage Error (MAPE) between the experimental data for three models NH (blue), JC (orange), and ODE (green) across five conditions of different temperature and strain rate. Figure 5.21(a) shows the MAPE of the conventional approach, whilst Figure 5.21(b) show the MAPE of the machine learning approach and the experimental data. For the ML approach, the ODE model on average has the lowest MAPE and at deformation temperature of 450 °C and target strain rate of 2.5 /s less than 2% MAPE. The NH, JC and the ODE based model performs well, especially in the machine learning approach, where the MAPE errors remain below 7%.

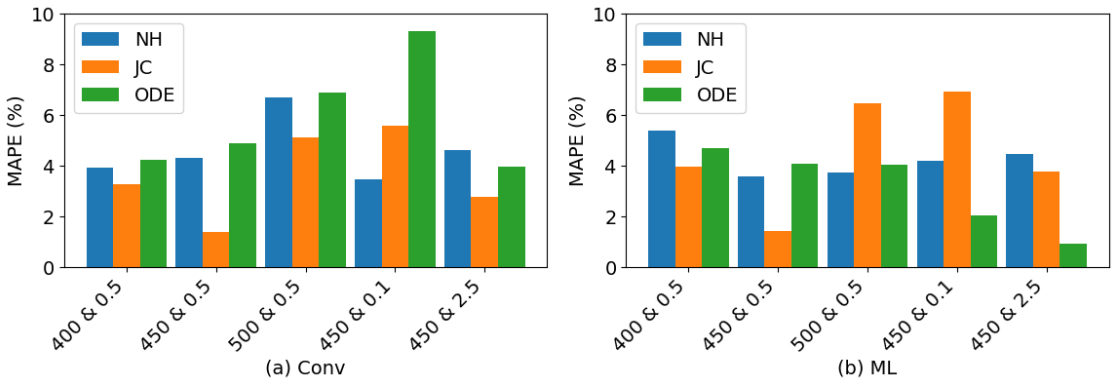


Figure 5.21 Comparison of Mean Absolute Percentage Error (MAPE) between experimental data and different models (NH, JC, ODE) across varying conditions of temperatures and strain rates. With: (a) Conventional approach and (b) ML approach.

5.9 Summary of main findings

In this Chapter, the thermomechanical uniaxial tensile test results of aluminium alloy AA6082 under HFQ conditions are presented and analysed. The tests were carried out using both the conventional and the machine learning approach using the novel data-driven deep learning method described in Chapter 4. The test temperature used were 400, 450 and 500 °C and the target strain rates were 0.1, 0.5 and 2.5 /s. The main findings can be summarised as below:

- By accurately predicting strain distributions across various deformation temperatures and strain rates, the ML-based approach successfully demonstrates its effectiveness for strain rate control for Gleeble uniaxial tensile testing.

- The novel approach mitigates the inaccuracies in the conventional Stroke-based Strain Testing (SST) and achieves a Mean Absolute Percentage Error (MAPE) for strain rate less than 11%, while the MAPE for the conventional approach can be as high as 138%. The ML based SST results in a reduction in MAPE ranging between 91.3% to 94.1%.
- The overall trend of flow stress is the same for the two approaches, i.e. increasing with decreasing temperature and increasing strain rate. The new approach allows more accurate determination of the material thermomechanical properties at various temperatures and strain rates. The strain rate using the conventional method can increase up to seven times the target strain rate as the test progresses, therefore leading to unreal strain hardening, while the experimental flow stress of AA6082 obtained using ML-approach shows much weaker hardening behaviour. The difference in flow stress can be as high as over 40 MPa.
- An analysis has been presented of the suitability of various constitutive models, including function-based constitutive equations, the Norton-Hoff (N-H) model, the Johnson-Cook model as well as an ODE-type unified constitutive equations. These models are essential for predicting how materials respond to stress, strain, temperature, and strain rate changes during deformation processes.
- The fitting of these models was made using stress-strain curves from the deformation of aluminium alloy AA6082 under uniaxial conditions across a wide range of deformation conditions. All three models have been calibrated against experimental stress-strain curves obtained using both the conventional and ML-based approaches, which show a good agreement.
- The study also emphasised the problems associated from determining accurate material constants accurately from experimental data strain with non-constant strain rate (present in Conventional approach). Where the applied strain rate often diverges from the target strain rate, leading to inaccuracies. The integration of machine learning into the testing process would ensure constant strain rate control and therefore avoid the above dilemma, ultimately improving the accuracy of the model.
- Finally, this Chapter underscored the potential of combining advanced constitutive modelling with machine learning techniques to achieve more robust and precise understanding of material behaviour. This approach is crucial for optimising manufacturing processes and advancing material design.

6 Numerical Benchmarking for Constitutive Equations

6.1 Introduction

The lack of computational studies to benchmark the performance of different numerical solvers on various stiff constitutive equations means that solving these equations may be far from optimised [97]. This motivates the need for efficient numerical integration of certain types of stiff constitutive equations, such as those given in the Appendix A.

The ODEs describing these constitutive equations (e.g. Appendix A) are often multiscale and stiff, making them amenable only to implicit solvers due to their better stability properties. Therefore, the choice of numerical integration method is of particular importance. Significant research has been performed to efficiently solve stiff differential equations [102]. Owing to their simplicity, lower-order implicit numerical integration methods, such as semi-implicit methods [92], implicit Euler (IE) [74] and trapezoidal rule (TR) [103], have been frequently applied to overcome these difficulties for moderately stiff systems. Two new variants of diagonally implicit Runge-Kutta (DIRK) methods are utilised [96, 104], which have been shown to be promising for solving stiff constitutive equations. The TR-BDF2 (backward differentiation formulae of order two, with the use of the trapezoidal rule sub-step) has been proposed as it increases the order of the method while still ensuring a stronger form of stability (L-stability) [105]. Another promising semi-implicit method is the Rosenbrock method [96] which provides an efficient method to solve nonlinear differential equations (Rosenbrock 2-3, or R23). The RADAU5 method is an advanced 5^{th} order method belonging to the Radau IIA class [106].

In this chapter, numerical benchmarking is performed on several promising numerical integration methods for applications in viscoplastic/creep-ageing constitutive equations. Specifically, this study focuses on providing a comparison of the following implicit methods, IE, TR, TR-BDF2, R23, and RADAU5, in solving three sets of viscoplastic/creep-ageing constitutive equations. A key focus of this research is to identify whether a unified constitutive equation model, described as an ODE, is numerically stiff. Moreover, a novel stiffness index is proposed based on the ratio of the largest and smallest negative real parts of the eigenvalues of the Jacobian and the dynamically controlled step size, allowing an accurate and unitless evaluation of the degree of stiffness.

6.1.1 Numerical stiffness assessment

The stiffness of ODEs is important for systems defined as initial-value problems (IVPs). There is no universally accepted definition of stiffness, causing difficulty in assessment. For stiff ODEs, certain implicit methods, particularly backward differentiation methods, tend to be more efficient than explicit methods [74]. Most stiff systems are only amenable to implicit methods, and the resulting nonlinear differential equations must be solved by a root-finding method such as a fixed-point iteration and Newton's method [96]. In this case, the Jacobian is given by the $NE \times NE$ matrix, which is used to converge to the solution of these nonlinear differential equations:

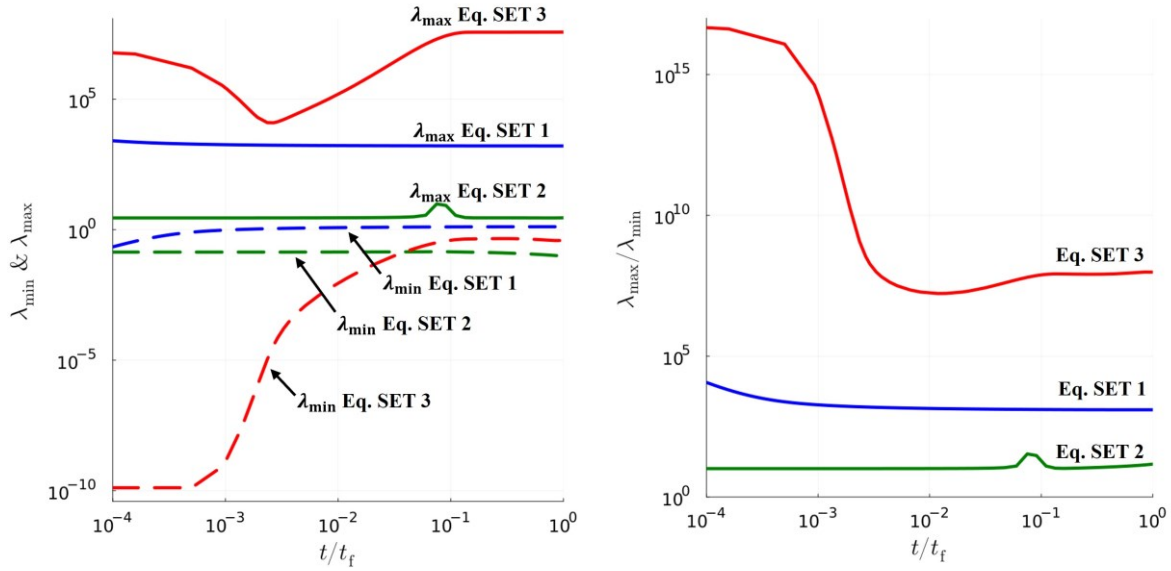
$$\boldsymbol{J} = \begin{pmatrix} \frac{\partial \mathrm{f}_1}{\partial y_1} & \cdots & \frac{\partial \mathrm{f}_1}{\partial y_{NE}} \\ \vdots & \ddots & \vdots \\ \frac{\partial \mathrm{f}_{NE}}{\partial y_1} & \cdots & \frac{\partial \mathrm{f}_{NE}}{\partial y_{NE}} \end{pmatrix} \tag{6.1}$$

The Jacobian matrix can be obtained using a finite difference method (refer to [92] with $\alpha = 10^{-2}$). To understand the stiffness within the ODE systems, using Equation (6.2), we can examine the set of eigenvalues of the Jacobian matrix $\boldsymbol{J}$, $\lambda = \{\lambda_i : i = 1, \dots, NE\}$. Explicitly, the eigenvalues are obtained from the NE degree polynomial:

$$|\boldsymbol{J} - \lambda \boldsymbol{I}| = 0 \tag{6.2}$$

where $\boldsymbol{I}$ is the identity matrix. Newton's method [77] can be used to solve Equation (6.2). A stiff system occurs when some components of the solution decay more rapidly than others [137]. This is often the case when one eigenvalue with a large negative real part exists in the system or, more accurately, when large variations exist between the maximum and minimum eigenvalues. Figure 6.1 shows the range obtained from the largest and smallest eigenvalues of the negative real part, $\lambda_{\min}$ and $\lambda_{\max}$, for all three considered unified constitutive equations (SET 1, SET 2, and SET 3, as given in Appendix A). Where $\lambda_{\min} = \min\big(\mathrm{Re}(-\boldsymbol{\lambda})\big)$ and $\lambda_{\max} = \max\big(\mathrm{Re}(-\boldsymbol{\lambda})\big)$. Equation SET 1 is for hot forming of micro-alloyed air-quenched steel at 1100 K, SET 2 is for creep-ageing of aluminium alloy AA2050-T34 at 428 K, and SET 3 is for continuous dynamic recrystallisation (CDRX) during hot deformation of aluminium alloy at 693 K. These equations are often employed in metal forming to model a wide range of different simulations and have been identified as numerically stiff in the literature [63, 90, 138]. For

each equation set, $\lambda_{\min}$ and $\lambda_{\max}$ are plotted against t/t_f such that they are on the same normalised time scale, with the solid lines representing the maximum eigenvalue $\lambda_{\max}$ obtained over the solution trajectory and the dashed lines representing the minimum eigenvalue $\lambda_{\min}$ for the constitutive equation SETs 1-3. It should be noted that $\lambda_{\min}$ and $\lambda_{\max}$ remain approximately constant for SET 1 and SET 2 and hence, the range of eigenvalues for each of the equation sets is constant. Owing to the additional microstructural and metallurgical features incorporated into SET 3, a much larger range existed for the set of eigenvalues. This means that for SET 3, a large variation between $\lambda_{\min}$ and $\lambda_{\max}$ exists along the solution trajectory, which decreases over time.



(a) $\lambda_{\min}$ & $\lambda_{\max}$ versus normalised time (b) $\lambda_{\max}/\lambda_{\min}$ versus normalised time

Figure 6.1 Maximum (solid curves) and minimum (dashed curves) eigenvalues and their ratios for: equation SET 1 at a strain rate of $\dot{\varepsilon}_{\mathrm{T}} = 0.1$ /s for $0 \leq t \leq 5$ s at 1100 K, equation SET 2 at a stress level of $\sigma = 180$ MPa for $0 \leq t \leq 18$ hr at 428 K, and equation SET 3 at a strain rate of $\dot{\varepsilon}_{\mathrm{T}} = 0.1$ /s for $0 \leq t \leq 5$ s at 693 K.

A new definition of numerical stiffness is proposed in this study. In Table 6.1, this new definition is outlined with two existing numerical stiffness definitions, and the features and disadvantages of these definitions are compared. This comparative analysis is intended to facilitate their implementation in assessing the numerical stiffness of ODE systems, such as the constitutive models formulated in Equation (2.25). It should be noted that the definition of stiffness does not extend to singular points within the ODE system. Singular points, where the derivatives fail to be well-defined, do not enable straightforward computation of the Jacobian

matrix or its eigenvalues [64]. Therefore, the method developed in this study can be applied to any general system of ODEs that describe different metal forming processes, provided no singular points exists.

Table 6.1 Different definitions of numerical stiffness criteria.

Definition of stiffness	Features	Disadvantages
$S_1 = \frac{\lambda_{\max}}{\lambda_{\min}}$ (6.3)	Hairer [74] considered the ratio of the negative real part of the set of eigenvalues.	The time span during the numerical integration is not considered.
$S_2 = \frac{\lambda_{\max}}{\lambda_{\min}}(t_f - t_0)$ (6.4)	Many authors (e.g. [139]) introduced an additional factor of the time span as this has an important role.	For viscoplastic constitutive equations, there is a significant effect of strain rate on the order of the stiffness index.
$S_3 = \frac{\lambda_{\max}}{\lambda_{\min}}\frac{(t_f - t_0)}{\Delta t}$ (6.5)	The current step size is used to provide a unitless second factor. The ratio of the time span to the current step size, is used as an indicator to identify when the step size becomes unacceptable and stability requirements constrain the step size.	Stiffness definition is based on the step size which is controlled dynamically within a numerical method.

Each stiffness definition listed in Table 6.1 can be implemented in numerical methods so that the numerical stiffness can be evaluated over the solution trajectory for every time increment. In the present study, the step size for stiffness index S_3 was determined using the step size control algorithm [92]. This algorithm controls step size, which enables a numerical method to navigate numerical instability and provides efficient numerical integration.

6.2 Implicit methods for stiff ODEs

A variety of explicit integration methods are available for non-stiff problems. These methods are known to provide accurate and computationally efficient numerical solutions for these systems [74]. In contrast, if the stability of an explicit method requires an unacceptably small step size, the problem is stiff, and an implicit method must be used. The following subsections introduce several promising implicit methods for solving stiff ODEs.

6.2.1 Implicit Euler (IE)

The most widely used implicit method is the IE method:

$$\boldsymbol{y}_{k+1} = \boldsymbol{y}_k + \Delta t \cdot \mathbf{f}_{k+1} \tag{6.6}$$

where $\mathbf{f}_{k+1}$ denotes the derivative evaluated at t_{k+1}, and Δt is the step size for the current step. This first-order implicit method is well suited to stiff problems due to its stability [95].

More advanced numerical integration methods have been developed [92, 96]. Among these methods, significant efforts have been made to control the step size more efficiently [74]. Step size control algorithms are crucial for helping numerical methods navigate numerical instability and provide efficient numerical integration [92]. If Δt produces a local truncation error e, then the new step size is estimated in accordance with a tolerance of Tol and an appropriate norm [140]:

$$\Delta t^{\text{new}} = \Delta t \cdot \left\| \frac{Tol}{\boldsymbol{e}} \right\|^{\frac{1}{p+1}} \tag{6.7}$$

where p is the order of the method and $Tol = Tol_{\text{abs}} + Tol_{\text{rel}} \cdot \max(|y_k|, |y_{k-1}|)$; Tol_{abs} is the absolute tolerance and Tol_{rel} is the relative tolerance [74], both of which are user-defined. It should be noted that Equation (6.7) can be implemented in any embedded method to dynamically control step size.

6.2.2 Runge-Kutta (RK) methods

RK methods achieve higher accuracy by retaining the one-step form but sacrificing linearity. In general, the one-step nature makes it easy to dynamically change the step size but makes it difficult to estimate the local error. The *s*-staged RK methods for autonomous systems are given by [141]:

$$\boldsymbol{y}_{k+1} = \boldsymbol{y}_k + \Delta t \sum_{i=1}^{s} b_i \boldsymbol{K}_i \tag{6.8}$$

$$\boldsymbol{K}_i = \mathrm{f}(\boldsymbol{y}_k + \sum_{j=1}^{s} a_{ij} \boldsymbol{K}_j),\ i = 1, \ldots, s \tag{6.9}$$

where a_{ij} and b_i are the real parameters that determine both the order and type of the implicit RK method for an autonomous system. Additionally, $\boldsymbol{K}_i$ are the intermediate stages for each

application of the RK method. The RK method is explicit if $a_{ij} = 0$ $(j \geq i)$ and implicit otherwise. Each RK method has uniquely determined parameters $(\boldsymbol{A}, \boldsymbol{b}, \boldsymbol{c})$, where $\boldsymbol{A}$ is a $s \times s$ matrix given by $\boldsymbol{A} = (a_{ij})$, vector $\boldsymbol{b}^{\mathbf{T}} = (b_1 \quad ... \quad b_s)$ and likewise with $c_i = \sum_{j=1}^{s} a_{ij}$; these values are commonly presented in a Butcher Tableau, as shown in Table 6.2.

Table 6.2 Butcher Tableau used to determine the RK method.

$\boldsymbol{c}$	$\boldsymbol{A}$
	$\boldsymbol{b}^{\mathrm{T}}$

An RK method is of order p, if p is the largest integer satisfying:

$$\boldsymbol{y}_{k+1} - \boldsymbol{y}(t_k + \Delta t) = \mathcal{O}(\Delta t^{p+1}) \text{ for } \Delta t \to 0 \tag{6.10}$$

where $\boldsymbol{y}_{k+1}$ is the numerical solution obtained using the RK method, $\boldsymbol{y}(t_k + \Delta t)$ denotes the exact solution, and big $\mathcal{O}$ denotes the order of the approximation. The implementation of the RK method with error control is mostly performed by considering a pair of RK methods of different orders. Explicit RK pairs of increasing order were proposed in [74], where pairs of orders (4,5) and (7,8) were constructed; these embedded RK pairs are known to be more accurate numerical solutions for non-stiff systems. The main advantage of implicit RK methods is evident from the analysis of the stability function, in which stronger properties are obtained for use in stiff systems. To study the stability properties of RK methods, the following test equation is applied:

$$\dot{\boldsymbol{y}} = \lambda \cdot \boldsymbol{y}, \ \boldsymbol{y}(t_0) = \boldsymbol{y}_0, \ \lambda \in \mathbb{C} \tag{6.11}$$

where $\mathbb{C}$ denotes the set of complex numbers. This yields a stability function $\mathrm{R}(z)$ that satisfies $\boldsymbol{y}_{k+1} = \mathrm{R}(z) \cdot \boldsymbol{y}_k$, where $z = \lambda \cdot \Delta t$. When applied to the *s*-staged RK method (see Equation (6.8)), the following rational polynomial is obtained [95]:

$$\mathrm{R}(z) = \frac{\det(\boldsymbol{I} - z \cdot \boldsymbol{A} + z \cdot \mathbf{1}_s \cdot \boldsymbol{b}^{\mathrm{T}})}{\det(\boldsymbol{I} - z \cdot \boldsymbol{A})} \tag{6.12}$$

where $\det$ denotes the determinant of the matrix, and $(\boldsymbol{A}, \boldsymbol{b}, \boldsymbol{c})$ are the real parameters that determine the *s*-staged RK method, and $\mathbf{1}_s$ is a vector of ones. It should be noted that the stability function $\mathrm{R}(z)$ is given by the quotient of two polynomials of degree s if the method

has s stages. Explicit RK methods have a strictly lower triangular matrix $\boldsymbol{A}$, meaning that $\det(\boldsymbol{I} - z\boldsymbol{A}) = 1$ and thus, the stability function is simply given by a polynomial. Explicit RK methods are generally unsuitable for stiff systems, because the region of absolute stability is smaller and bounded [95]. A method is A-stable if $|\mathrm{R}(z)| < 1$, for all the points in the set $\mathbb{C}^- = \{z \in \mathbb{C} : \mathrm{Re}(z) < 0\}$. A numerical method is L-stable if $\lim_{|z|\to\infty} \mathrm{R}(z) = 0$, and L-stability is a stronger form of stability related to the asymptotic behaviour of the stability function. Numerical methods satisfying this asymptotic relation are best suited for solving stiff ODEs [74].

Diagonally implicit Runge-Kutta (DIRK) methods are a type of implicit Runge-Kutta method used to calculate the solution at each time step. The key feature of the DIRK method, which enhances its computational efficiency compared with other implicit RK methods, is its lower triangular property ($a_{ij} = 0$ for $i < j$), as indicated in Table 6.3. This matrix being lower triangular means that at each increment $\boldsymbol{K}_i$ must be solved sequentially as opposed to simultaneously for $i = 1, \ldots, s$ and therefore, only one *NE*-dimensional nonlinear system needs to be solved. Therefore, the complexity at each step of a DIRK method is reduced from $\mathcal{O}\left(\frac{(s\cdot NE)^3}{3}\right)$ to $\mathcal{O}\left(\frac{s\cdot(NE)^3}{3}\right)$ operations compared with its equivalent implicit RK method.

Table 6.3 Butler Tableau for a DIRK method.

c_1	a_{11}	0	0	0
c_2	a_{21}	a_{22}	0	0
$\vdots$	$\vdots$	$\vdots$	$\ddots$	0
c_s	a_{s1}	a_{s2}	...	a_{ss}
	b_1	b_2	...	b_s

If all the diagonal entries of $\boldsymbol{A}$ are equal ($a_{ii} = \gamma$ for i =1, …, s), then the DIRK method is called the singly diagonally implicit Runge-Kutta (SDIRK) method [76].

6.2.3 Trapezoidal Rule-Backwards Differentiation Formulae 2 (TR-BDF2)

The TR-BDF2, first introduced in [105], is defined as a one-step method that is formed by combining TR in the first sub-step with the use of BDF2 in the second sub-step given below:

$$\boldsymbol{y}_{k+\gamma} = \boldsymbol{y}_k + \gamma \frac{\Delta t}{2}\left(\mathbf{f}_k + \mathbf{f}_{k+\gamma}\right) \tag{6.13}$$

$$\boldsymbol{y}_{k+1} = \frac{1}{\gamma(2-\gamma)}\boldsymbol{y}_{k+\gamma} - \frac{(1-\gamma)^2}{\gamma(2-\gamma)}\boldsymbol{y}_k + \frac{1-\gamma}{2-\gamma}\Delta t \cdot \mathbf{f}_{k+1} \tag{6.14}$$

where $\gamma \in (0, 1)$ is a parameter that determines the stability and characteristics of the method. The value of $\gamma = 2 - \sqrt{2}$ as derived in [105], ensures $\frac{\gamma}{2} = \frac{1-\gamma}{2-\gamma}$. When imposing this condition, both stages of the TR-BDF2 method have equal Jacobian matrix. For this particular value, the TR-BDF2 method is considered a DIRK [76], along with the Butcher tableau presented in Table 6.4.

Table 6.4 Butcher tableau for the TR-BDF2 formulated as a DIRK.

0	0	0	0
γ	$\frac{\gamma}{2}$	$\frac{\gamma}{2}$	0
1	$\frac{1}{2(2-\gamma)}$	$\frac{1}{2(2-\gamma)}$	$\frac{1-\gamma}{2-\gamma}$
	$\frac{1}{2(2-\gamma)}$	$\frac{1}{2(2-\gamma)}$	$\frac{1-\gamma}{2-\gamma}$

This method has been found to be particularly promising for stiff ODEs owing to its strong stability and improved order of accuracy achieved by the use of higher-order BDF [103]. As the TR-BDF2 is an implicit method, the resulting nonlinear differential equations must be solved at each step. Practically, because of the instability of fixed-point solvers, the root-finding problem $\mathbf{G}(\boldsymbol{y}_{k+1}) = 0$ is solved using an iterative Newton's method [105] $\boldsymbol{y}_{k+1}^{(n+1)} = \boldsymbol{y}_{k+1}^{(n)} - \mathbf{G}'\left(\boldsymbol{y}_{k+1}^{(n)}\right)^{-1} \cdot \mathbf{G}\left(\boldsymbol{y}_{k+1}^{(n)}\right)$ such that $\boldsymbol{y}_{k+1}^{(n)} \to \boldsymbol{y}_{k+1}$, where $\mathbf{G}'$ denotes the derivate. For each step of the TR-BDF2 method, the root-finding problem is solved as:

$$\boldsymbol{y}_{k+\gamma}^{(n+1)} = \boldsymbol{y}_{k+\gamma}^{(n)} - \left[\boldsymbol{I} - \frac{\gamma}{2}\Delta t \cdot \boldsymbol{J}\right]^{-1} \cdot \mathbf{G}_1\left(\boldsymbol{y}_{k+\gamma}^{(n)}\right), \qquad \boldsymbol{y}_{k+\gamma}^{(0)} = \boldsymbol{y}_k \tag{6.15}$$

$$\boldsymbol{y}_{k+1}^{(n+1)} = \boldsymbol{y}_{k+1}^{(n)} - \left[\boldsymbol{I} - \frac{1-\gamma}{2-\gamma}\Delta t \cdot \boldsymbol{J}\right]^{-1} \cdot \mathbf{G}_2\left(\boldsymbol{y}_{k+1}^{(n)}\right), \quad \boldsymbol{y}_{k+1}^{(0)} = \boldsymbol{y}_k \tag{6.16}$$

where $\boldsymbol{I}$ is the identity matrix and $\boldsymbol{J}$ is the Jacobian matrix determined by Equation (6.1), $\mathbf{G}_1\left(\boldsymbol{y}_{k+\gamma}^{(n)}\right)$ and $\mathbf{G}_2\left(\boldsymbol{y}_{k+1}^{(n)}\right)$ are the residuals for each nonlinear difference equation in Eqs. (6.15) and (6.16), respectively, in the Newton's iterations. The truncation error was estimated using a cubic Hermite interpolant [75]. By applying Eqs. (6.15) and (6.16), the local truncation error can be approximated as:

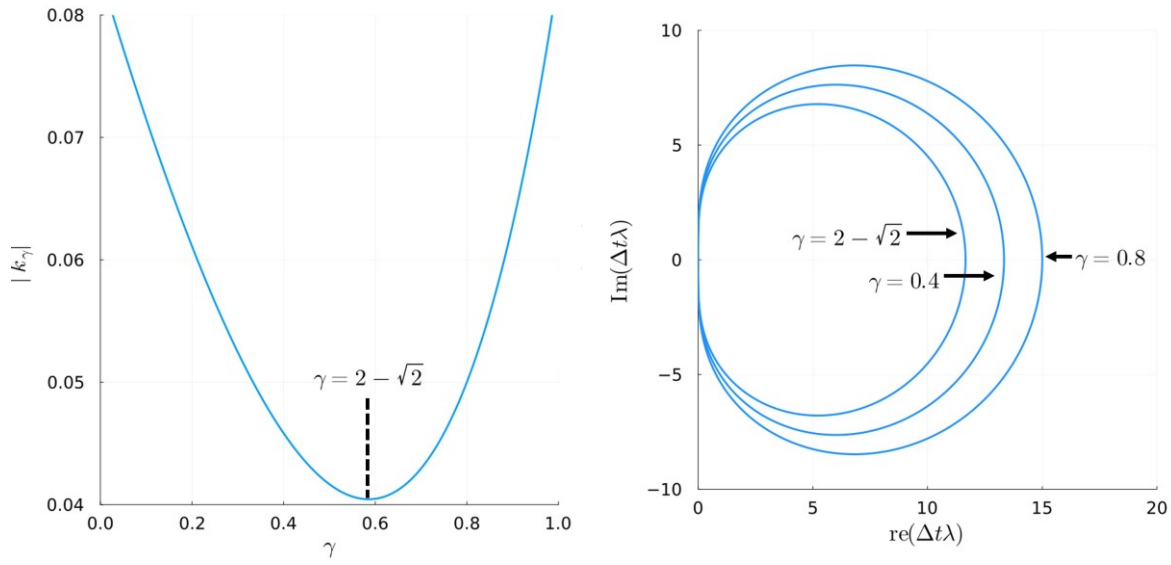
$$\boldsymbol{e} \approx 2k_\gamma \Delta t \left(\frac{1}{\gamma} \cdot \mathbf{f}_k - \frac{1}{\gamma(1-\gamma)} \cdot \mathbf{f}_{k+\gamma} + \frac{1}{(1-\gamma)} \cdot \mathbf{f}_{k+1}\right) \tag{6.17}$$

where $k_\gamma = \frac{-3\gamma^2+4\gamma-2}{12(2-\gamma)}$ with parameter γ in the range of $(0, 1)$. This provides a third order accurate assessment of the local truncation error at each time step. The formulation of the TR-BDF2 as a DIRK class of methods enables the computation of the region of absolute stability using Equation (6.12), and the real parameters $(\boldsymbol{A}, \boldsymbol{b}, \boldsymbol{c})$ are determined using the Butcher tableau presented in Table 6.3. This yields a rational polynomial for the stability function for the TR-BDF2 method:

$$\mathrm{R}(z) = \frac{\det(\boldsymbol{I} - z\cdot\boldsymbol{A} + z\cdot\mathbf{1}_s\cdot\boldsymbol{b}^{\mathrm{T}})}{\det(\boldsymbol{I} - z\cdot\boldsymbol{A})} = \frac{2\gamma-2-(2-2\gamma+\gamma^2)z}{\gamma(\gamma-1)z^2+(2-\gamma^2)z+2\gamma-4} \tag{6.18}$$

where $z = \lambda \cdot \Delta t$, $\boldsymbol{b} = \left(\frac{1}{2(2-\gamma)}, \frac{1}{2(2-\gamma)}, \frac{1-\gamma}{2-\gamma}\right)^{\mathrm{T}}$, $\mathbf{1}_s = (1, \ldots, 1)^{\mathrm{T}}$ and $\boldsymbol{A} = \begin{pmatrix} 0 & 0 & 0 \\ \frac{\gamma}{2} & \frac{\gamma}{2} & 0 \\ \frac{1}{2(2-\gamma)} & \frac{1}{2(2-\gamma)} & \frac{1-\gamma}{2-\gamma} \end{pmatrix}$. The effects of this parameter γ in the range of $0 < \gamma < 1$ on $|k_\gamma|$ and hence the truncation error, are shown in Figure 6.2(a). As can be seen, $|k_\gamma|$ has a minimum value when $\gamma = 2 - \sqrt{2}$. Considering the stability function $\mathrm{R}(z)$, for the TR-BDF2, given in Equation (6.18) if z is a real number and $0 < \gamma < 1$ then $|\mathrm{R}(z)| < 1$ if and only if $z < 0$ or $z > \mathrm{Q}(\gamma)$, where the quotient $\mathrm{Q}(\gamma) = \frac{2(2-\gamma)}{\gamma(1-\gamma)}$ gives the edge of the region of absolute stability for $z = \Delta t \cdot \lambda$. The minimum values can be found by the differential, $\mathrm{Q}'(\gamma) = 0$ with $\mathrm{Q}'(\gamma) = \frac{2(\gamma^2-4\gamma+2)}{\gamma^2(1-\gamma^2)}$ which vanishes at $\gamma = 2 - \sqrt{2}$. This implies that Q has a local minimum at this point, and the absolute stability for $z = \Delta t \cdot \lambda$ is maximised when $\gamma = 2 - \sqrt{2}$. In Figure 6.2(b), for the TR-BDF2 method, the size of the region of absolute stability, as determined by

Equation (6.18) for three different choices of γ is investigated for $|\mathrm{R}(z)| < 1$ where an Argand diagram is used to show the edge of the stability region on the complex plane.



(a) Effect of γ on $|k_\gamma|$ (b) Effect of γ on the absolute stability regions

Figure 6.2 The factor $|k_\gamma|$ within the local truncation error and the region of absolute stability for the TR-BDF2 method. The latter is shown within the Argand diagram in which $\mathrm{Re}(\Delta t \cdot \lambda)$ and $\mathrm{Im}(\Delta t \cdot \lambda)$ denote the real and imaginary part, respectively, of a complex number $\Delta t \cdot \lambda$.

From the above, it can be stated that the region of absolute stability for the TR-BDF2 region is maximised when $\gamma = 2 - \sqrt{2}$, and L-stability is guaranteed because $\lim_{|z|\to\infty} \mathrm{R}(z) = 0$ (see Equation (6.18)). The local truncation error is also minimised because $|k_\gamma|$ obtains a minimum at this point. In addition, the Jacobians used to converge to the solutions of each nonlinear differential equation are equal when $\gamma = 2 - \sqrt{2}$. These advantages presented above mean that the TR-BDF2 method provides an efficient and reliable numerical integration of high-dimensional stiff unified constitutive systems.

6.2.4 Rosenbrock 2-3 (R-23) method

The most widely implemented Rosenbrock method is the R23 method which provides an embedded local truncation error by combining two methods of order two and three [96]. This method is formulated as:

$$\boldsymbol{K}_1 = \boldsymbol{W}^{-1} \cdot \mathbf{f}_k \tag{6.19}$$

$$\boldsymbol{K}_2 = \boldsymbol{W}^{-1} \cdot [\mathbf{f}_{k+0.5} - \boldsymbol{K}_1] + \boldsymbol{K}_1 \tag{6.20}$$

$$\boldsymbol{y}_{k+1} = \boldsymbol{y}_k + \Delta t \cdot \boldsymbol{K}_2 \tag{6.21}$$

$$\boldsymbol{K}_3 = \boldsymbol{W}^{-1} \cdot [\mathbf{f}_{k+1} - c_{32}(\boldsymbol{K}_2 - \mathbf{f}_{k+0.5})) - 2(\boldsymbol{K}_1 - \mathbf{f}_k)] \tag{6.22}$$

where the matrix $\boldsymbol{W} = \boldsymbol{I} - a\Delta t\boldsymbol{J}$ which is assumed to be invertible, is used to approximate the solution, $\boldsymbol{J}$ is the numerical Jacobian matrix obtained using Equation (5.5), $a = \frac{1}{2+\sqrt{2}}$, $c_{32} = 6 + \sqrt{2}$ and $\dot{\boldsymbol{y}}_{k+0.5} = \dot{\boldsymbol{y}}\,(\boldsymbol{y}_k + 0.5\Delta t \cdot \boldsymbol{K}_1)$. The leading order local truncation error within the R23 pair is estimated as the difference between the second and third order numerical solution, and it is given as:

$$\boldsymbol{e} \approx \tfrac{\Delta t}{6}(\boldsymbol{K}_1 - 2\boldsymbol{K}_2 + \boldsymbol{K}_3) \tag{6.23}$$

The stability function for the R23 methods satisfies the relation $\boldsymbol{y}_{k+1} = \mathrm{R}(z) \cdot \boldsymbol{y}_k$, where $\mathrm{R}(z)$ satisfies Equation (6.12), with $z = \lambda \cdot \Delta t$, $\boldsymbol{b} = (0 \quad 0.5)$, $\mathbf{1}_s = (1 \quad 1)^{\mathrm{T}}$ and $\boldsymbol{A} = \boldsymbol{a} + \boldsymbol{\gamma}$ where $\boldsymbol{a} = \begin{pmatrix} 0 & 0 \\ 0.5 & 0 \end{pmatrix}$ and $\boldsymbol{\gamma} = \begin{pmatrix} a & 0 \\ -a & a \end{pmatrix}$. Using these quantities, the Butcher tableau for this DIRK method can be constructed using Table 6.4. Using this relation, it should be noted that improved stability within the Rosenbrock method is not obtained by increasing the accuracy of the numerical Jacobians. Consequently, in practice, there is no reason to compute a new numerical Jacobian at each step. Often, it is sufficient to update $\boldsymbol{J}$ on occasion.

6.2.5 RADAU5 method

Hairer's Radau IIA method [106] is based on collocation at the Gauss-Radau points, a technique widely acknowledged for its stability in numerical integration. This approach allows the method to provide high-accuracy solutions for stiff ODEs. The RADAU5 method is an embedded 3-stage method of order five (Radau IIA), which is accessible through the Butcher tableau, as shown in Table 6.5**.** The full explicit equation can be determined from the Butcher tableau and Equation (6.8).

Table 6.5 Butcher tableau for the RADAU5 formulated as a Radau IIA.

$\frac{4-\sqrt{6}}{10}$	$\frac{88-7\sqrt{6}}{360}$	$\frac{296-169\sqrt{6}}{1800}$	$\frac{-2+3\sqrt{6}}{225}$
$\frac{4+\sqrt{6}}{10}$	$\frac{296+169\sqrt{6}}{1800}$	$\frac{88+7\sqrt{6}}{360}$	$\frac{-2-3\sqrt{6}}{225}$
1	$\frac{16-\sqrt{6}}{36}$	$\frac{16+\sqrt{6}}{36}$	$\frac{1}{9}$
	$\frac{16-\sqrt{6}}{36}$	$\frac{16+\sqrt{6}}{36}$	$\frac{1}{9}$

6.3 Comparison of stability regions of RK methods

The stability of those implicit methods mentioned above can be determined by considering the test equation (Equation (6.11)), which yields the stability function satisfying $\boldsymbol{y}_{k+1} = \mathrm{R}(z) \cdot \boldsymbol{y}_k$, where $z = \lambda \cdot \Delta t$. The stability function of each RK method is presented in Table 6.6, which allows for a comparison of the sizes of the regions of absolute stability.

Table 6.6 Stability function for the implicit methods by applying the test equation Equation (6.11).

Numerical method	Type of method	Order	Stability function
Implicit Euler (IE)	Linear	1	$\mathrm{R}(z) = \frac{1}{1-z}$
Trapezoidal Rule (TR)	RK	2	$\mathrm{R}(z) = \frac{1+z/2}{1-z/2}$
TR-BDF2 (see Equation 6.14)	DIRK	2	$\mathrm{R}(z) = \frac{2\gamma-2-(2-2\gamma+\gamma^2)z}{\gamma(\gamma-1)z^2+(2-\gamma^2)z+2\gamma-4}$
R23 (see Equation 6.21)	Rosenbrock method	2	$\mathrm{R}(z) = \frac{1+(1-2a)z}{(1-az)^2}$
RADAU5 (see Table 6.5)	Radau IIA	5	$\mathrm{R}(z) = \frac{1+\frac{2}{5}z+\frac{1}{10}z^2}{1-\frac{3}{5}z+\frac{2}{20}z^2-\frac{1}{60}z^3}$

Note $\gamma = 2-\sqrt{2}$ and $a = \frac{1}{2+\sqrt{2}}$ are adopted subsequently.

The absolute stability region for the considered RK methods is the domain in the complex plane given by:

$$D \coloneqq \{z \in \mathbb{C} : |\mathrm{R}(z)| \leq 1\} \tag{6.24}$$

Figure 6.3 shows an Argand diagram, with $\mathrm{Re}(\Delta t \cdot \lambda)$ and $\mathrm{Im}(\Delta t \cdot \lambda)$ denoting the real and imaginary parts, respectively, of a complex number $\Delta t \cdot \lambda$. The solid lines show the edge of the region of absolute stability, and the dashed arrows indicate the stability regions. For each numerical method, the stability was computed using Equation (6.12). All implicit methods are A-stable because the stability region contains $\mathbb{C}^{-}$. Additionally, the IE, R23, TR-BDF2, and RADAU5 methods are L-stable, satisfying the limit condition $\lim_{|z|\to\infty} \mathrm{R}(z) = 0$. While the IE method has the largest region of absolute stability, its limitation lies in being first-order accurate, resulting in a slower convergence rate compared to the higher-order implicit methods.

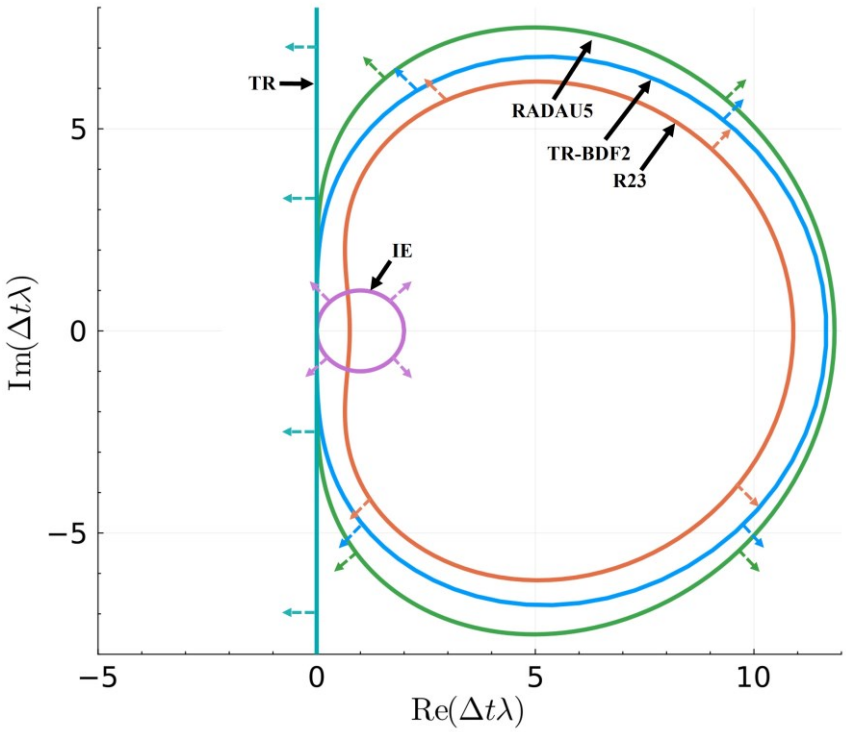


Figure 6.3 Regions of absolute stability D for each numerical method, IE, TR, TR-BDF2, R23 and RADAU5. $Re(\Delta t \cdot \lambda)$ and $Im(\Delta t \cdot \lambda)$ denote the real and imaginary part, respectively, of a complex number $\Delta t \cdot \lambda$.

6.4 Numerical computations of stiff ODEs using implicit methods

All three sets of unified constitutive equations (SET 1, SET 2, and SET 3 as given in Appendix A) were analysed to demonstrate the behaviour of the numerical stiffness criteria, listed in

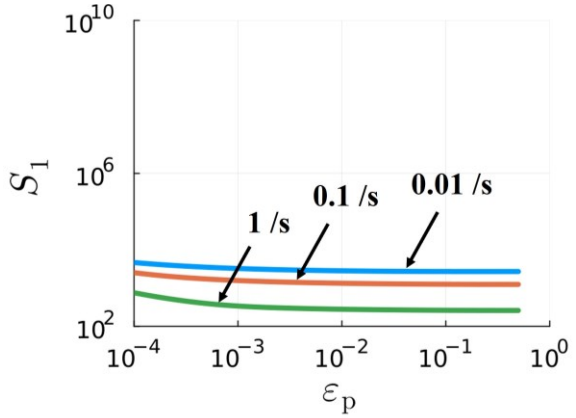
Table 6.1, when evaluated over the solution trajectory. Additionally, these sets of constitutive equations were numerically computed to assess the effectiveness of the five implicit methods, IE, TR, TR-BDF2, R23, and RADAU5, on each stiff system. In all the test cases, the nonlinear systems associated with these five implicit methods were solved using quasi-Newton iterations. All computations were performed on a single Intel Core™ i5 (3.5 GHz) processor with 8GB RAM. The error-workload curves were generated to provide the expected relative workload for each numerical method for the given equation SETs 1-3. The truncation error denoted $\|\boldsymbol{e}\|$ where $\boldsymbol{e}$ is a vector is obtained during each integration and measured using the l^{∞} absolute error norm [142] as:

$$\|\boldsymbol{e}\| = \sum_{k=1}^{N_t} \|\boldsymbol{y}_k - \tilde{\boldsymbol{y}}_k\|_{\infty} / N_t \tag{6.25}$$

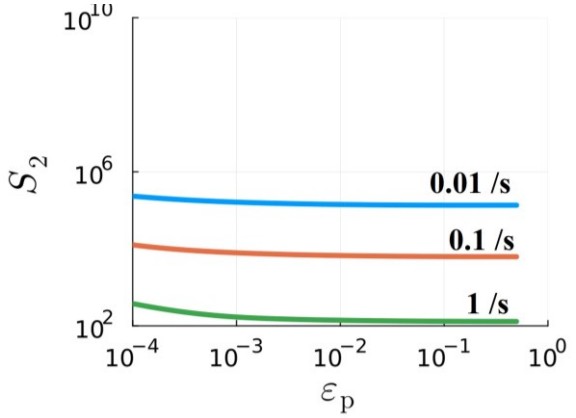
where N_t is the number of time steps required during the integration, $\boldsymbol{y}_k$ is the solution at the k^{th} step, and $\tilde{\boldsymbol{y}}_k$ is the reference solution used at the same time step. The reference solution can be obtained using an ODE solver, such as [96, 143], with absolute and relative error tolerances of $Tol_{\text{abs}} = Tol_{\text{rel}} = 10^{-12}$ such that the reference solution reflects the exact solution

6.4.1 Numerical computations of stiff equation SET 1

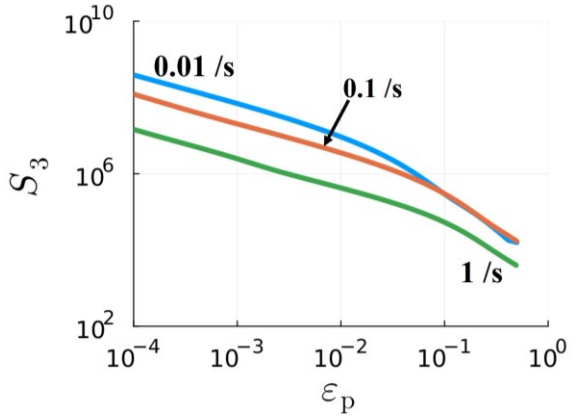
Equation SET 1 models the elastic–viscoplastic deformation and material hardening behaviour of micro-alloyed air-quenched steel in warm/hot forming [90] (see Equation A.1-A.3). Equation SET 1 was solved based on the material constants listed in Table A.1for $0 \leq t \leq \frac{0.5}{\dot{\varepsilon}_{\text{T}}}$ s with s being the unit seconds and $\dot{\varepsilon}_{\text{T}} = [0.01, 0.1, 1]$ /s is the total strain rate. Figure 6.4(a)–(c) plot the numerical stiffness definitions S_1, S_2 and S_3 (see Table 6.1) against plastic strain. As can be seen, in all cases, the ratio between λ_{min} and λ_{max} is initially the highest and decreases as the plastic strain increases. Figure 6.4(d) shows the stress-strain curves at three selected strain rates of 0.01, 0.1, and 1 /s, where the stress increased with increasing plastic strain until the yield point was obtained at 100, 190, and 250 MPa, respectively. During the computations, the step size was dynamically controlled for all strain rates using Equation (6.7) with an absolute error of $Tol_{\text{abs}} = 10^{-6}$ and a relative error of $Tol_{\text{rel}} = 10^{-5}$. Figure 6.4(e) and (f) show the step size against the plastic strain. It should be noted that t_{f} increases with decreasing total strain rate. In other words, the relative step size remained approximately the same for different strain rates.



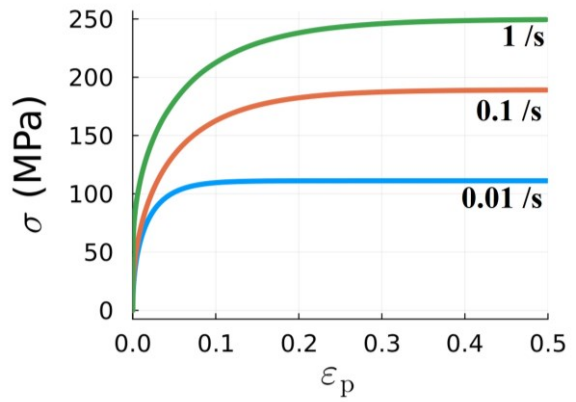
(a) Stiffness index S_1 versus plastic strain ε_p



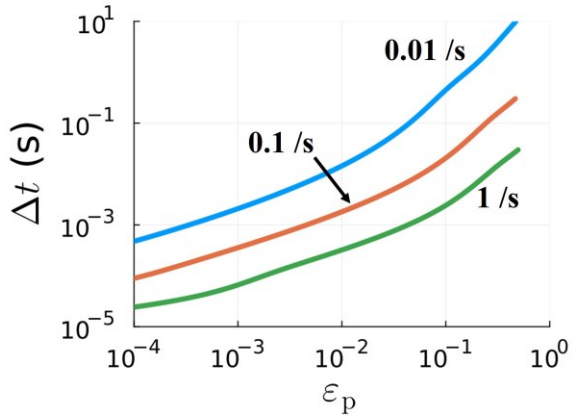
(b) Stiffness index S_2 versus plastic strain ε_p



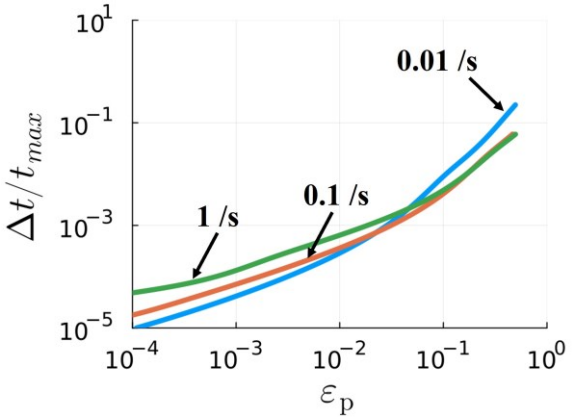
(c) Stiffness index S_3 versus plastic strain ε_p



(d) Stress σ versus strain ε_p



(e) Controlled step size Δt versus strain ε_p



(f) Step size Δt scaled with $t_{\max}$ versus ε_p

Figure 6.4 Computations of the constitutive equation SET 1 at three different strain rates $\dot{\varepsilon}_T = [0.01, 0.1, 1]$ /s for $0 \leq t \leq \frac{0.5}{\dot{\varepsilon}_T}$ s at 1100 K.

As shown in Figure 6.4(a)-(c), compared to stiffness indexes S_1 and S_3, stiffness index S_2 exhibits the greatest variation with strain rate, in which there is an order of magnitude difference in the value of S_2 for different strain rates. This indicates that S_1 and S_3, which

provide a unitless assessment of stiffness, are more appropriate numerical stiffness indices for equation SET 1. For the other two equation SETs considered, only numerical stiffness criteria S_1 and S_3 were therefore employed.

To further demonstrate the stiffness of equation SET 1 at a selected strain rate of $\dot{\varepsilon}_T$ = 0.1 /s, the error-workload curves were determined. In this analysis, the truncation error $\|\boldsymbol{e}\|$ was used because it is representative of the whole problem. Figure 6.5 shows the effects of truncation error on the CPU time for equation SET 1, in which the solution was determined within tolerances of $10^{-4} \leq Tol_{\text{rel}} \leq 10^{-9}$ and $10^{-5} \leq Tol_{\text{abs}} \leq 10^{-10}$. The error-workload curves were used to benchmark each numerical method at comparable levels of accuracy. The results in Figure 6.5 show that the TR, TR-BDF2, and R23 methods are almost equivalent in accuracy for low errors, with a slight advantage for the R23 method. Most evidently, the RADAU5 outperformed all other methods in terms of workload.

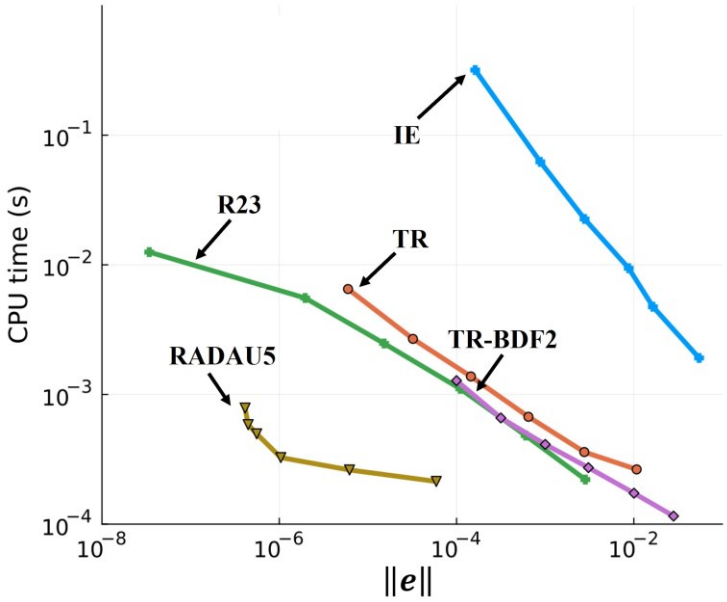
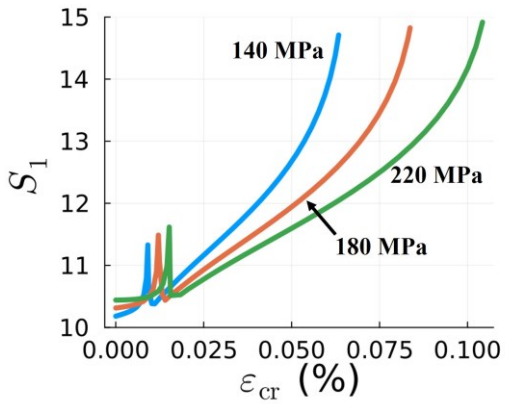


Figure 6.5 Numerical benchmarking of the five considered implicit integration methods (IE, TR, TR-BDF2, R23, and RADAU5) against equation SET 1 at a strain rate of $\dot{\varepsilon}_T = 0.1$ /s for the time interval of $0 \leq t \leq 5$ s.

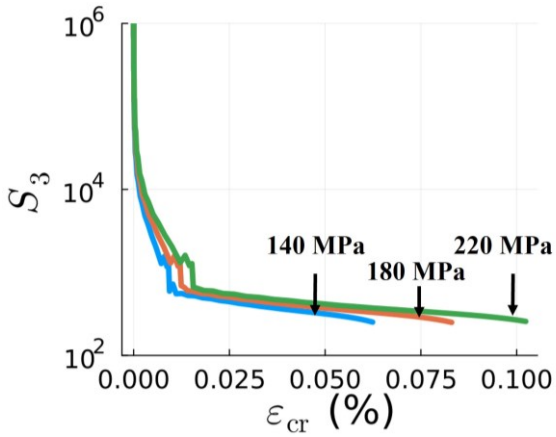
6.4.2 Numerical computations of stiff equation SET 2

As a representative case for creep ageing, equation SET 2 (see Equation A.4-A.14) was used to model the creep strain and time response of aluminium alloy AA2050-T34 under applied stresses [63]. Equation SET was solved using the material constants listed in Table A.2 in the

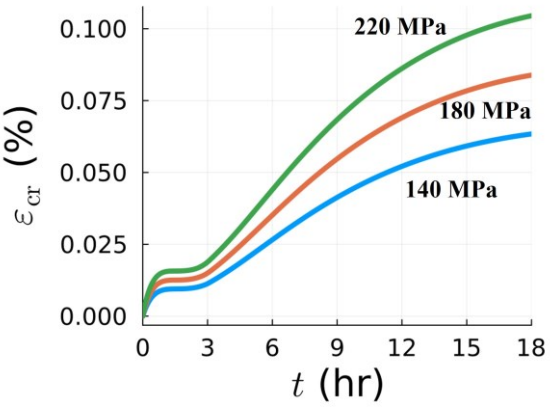
interval of $0 \leq t \leq 18$ hr at applied stresses of $\sigma = [140, 180, 220]$ MPa. Figure 6.6(a) shows the numerical stiffness index S_1 against the creep strain. Initially, the ratio between $\lambda_{\min}$ and $\lambda_{\max}$ was the smallest and increased with time. Fig 6(b) shows the numerical stiffness index S_3 against creep strain. This numerical stiffness initially obtains a maximum value and then decreases to a plateau. Furthermore, numerical solutions at all three stresses were obtained, although the spikes in S_1 and S_3 indicated a slight instability in obtaining the solution. Figure 6.6(c) shows the corresponding creep strain-time solution of the material during creep ageing under different applied stresses. All three creep curves exhibit an initial quick rise and short plateau due to combined effect of dislocation hardening, dissolution of existing clusters, and nucleation of new precipitates [144]. The step sizes used in each of the numerical solutions were dynamically controlled for each stress using Equation (6.7) under the tolerances of an absolute error of $Tol_{\text{abs}} = 10^{-6}$ and a relative error of $Tol_{\text{rel}} = 10^{-5}$. Figure 6.6(d) plots the step size against the plastic strain. Some fluctuations were observed, indicating numerical instability. Additionally, equation SET 2 exhibits less severe stiffness, as indicated in Figure 6.6(a) and (b).



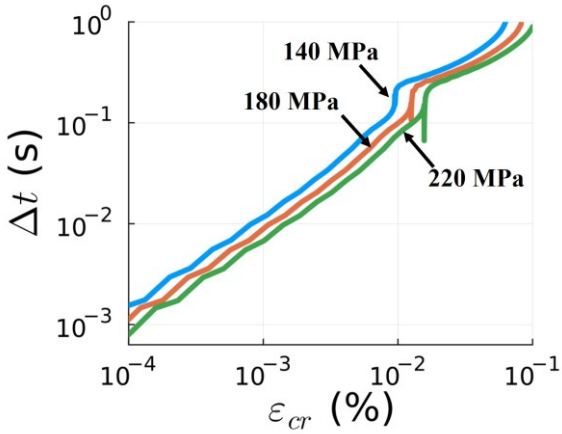
(a) Stiffness index S_1 versus creep strain $\varepsilon_{\mathrm{cr}}$



(b) Stiffness index S_3 versus creep strain $\varepsilon_{\mathrm{cr}}$



(c) Creep strain $\varepsilon_{\mathrm{cr}}$ versus time t



(d) Step size Δt versus plastic strain $\varepsilon_{\mathrm{cr}}$

Figure 6.6 Comparison of stiffness criteria S_1 and S_3 evaluated over the solution trajectory for equation SET 2, for three different stresses $\sigma = [140, 180, 220]$ MPa at 428 K for the time interval of $0 \leq t \leq$ 18 hr.

Figure 6.7 displays the error-workload curves for a stress of σ = 180. In the analysis, the truncation error, $\|\boldsymbol{e}\|$ (Equation (6.25)) was used, and the solution was determined within tolerances of $10^{-4} \leq Tol_{\mathrm{rel}} \leq 10^{-8}$ and $10^{-5} \leq Tol_{\mathrm{abs}} \leq 10^{-9}$. The error-workload curves were used to benchmark each numerical method at comparable levels of accuracy. As can be seen, the RADAU5 minimises the local truncation error associated from creep strain and provides the most computationally efficient solution for equation SET 2.

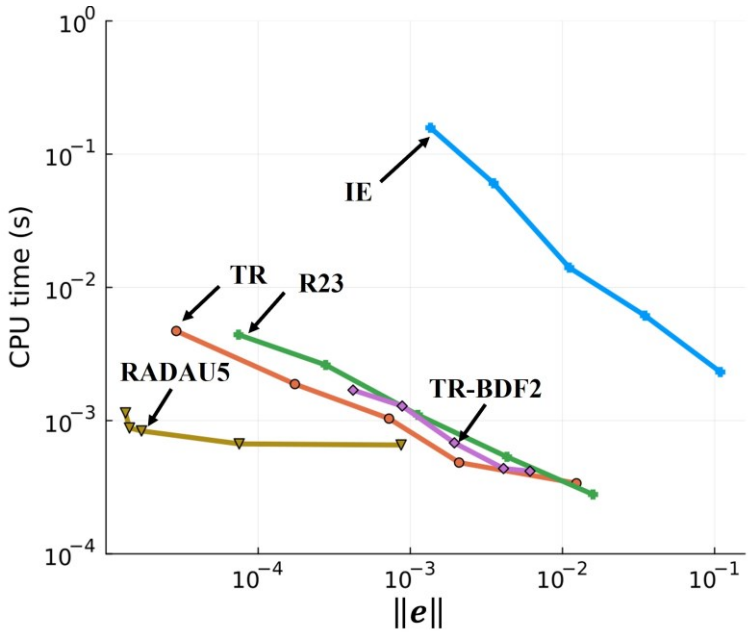
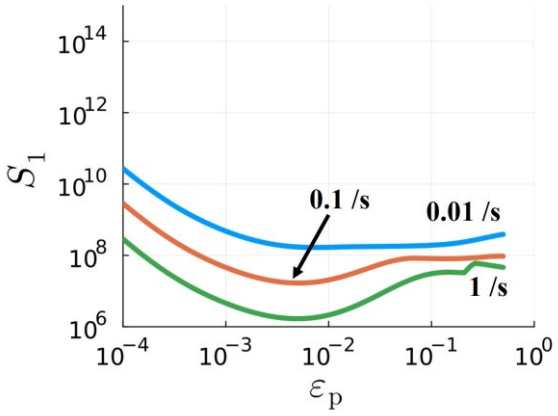


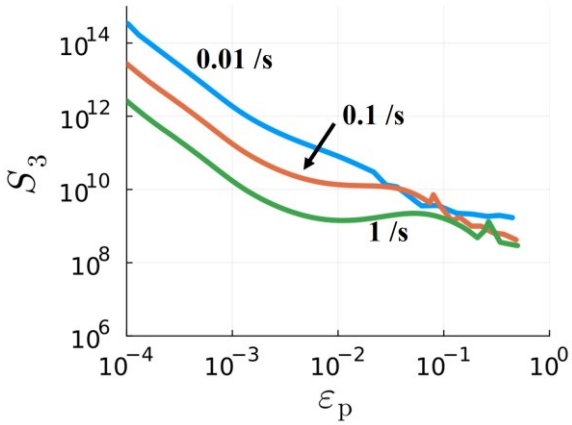
Figure 6.7 Numerical benchmarking of the five considered implicit integration methods (IE, TR, TR-BDF2, R23, and RADAU5) against equation SET 2 at σ =180 MPa for the time interval of $0 \leq t \leq$ 18 hr.

6.4.3 Numerical computations of stiff equation SET 3

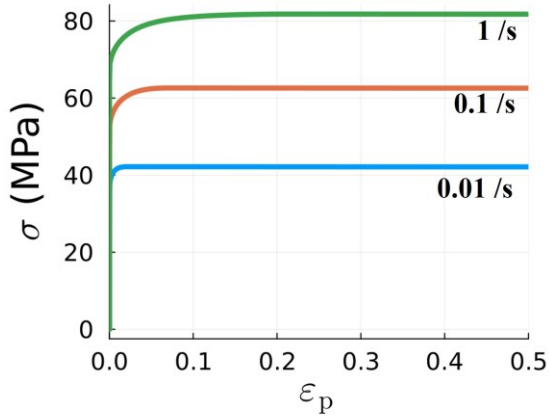
Equation SET 3 is a six-dimensional ODE system modelling CDRX for hot deformation of aluminium alloys [138] (see Equation A.15-A.24), which was solved using the initial values and material parameters listed in Table A.3, for $0 \leq t \leq \frac{0.5}{\dot{\varepsilon}_{\mathrm{T}}}$ s at strain rates of $\dot{\varepsilon}_{\mathrm{T}} = [0.01, 0.1, 1]$ /s and a temperature of T = 693 K. Figure 6.8(a) and (b) plot the numerical stiffness indexes S_1 and S_3 against plastic strain, respectively. In all cases, the ratio between $\lambda_{\min}$ and $\lambda_{\max}$ was the highest at the beginning and decreased with increasing plastic strain. Figure 6.8(c) shows the stress-strain curves for three strain rates of 0.01, 0.1, and 1 /s, where the stress increased with increasing plastic strain until the yield point was obtained at 40, 60, and 80 MPa, respectively. The step size was dynamically controlled for all the strain rates using Equation (9) provides an absolute error of $Tol_{\mathrm{abs}} = 10^{-6}$ and a relative error of $Tol_{\mathrm{rel}} = 10^{-5}$. Figure 6.8(d) shows the plastic strain against the step size. Larger step sizes were obtained at smaller strain rates, and the largest step size was obtained for a strain rate of 0.01 /s. Additionally, mild fluctuation in the dynamically controlled step size occurred for all strain rates owing to the associated numerical stiffness of equation SET 3. These fluctuations are more pronounced at lower strain rates.



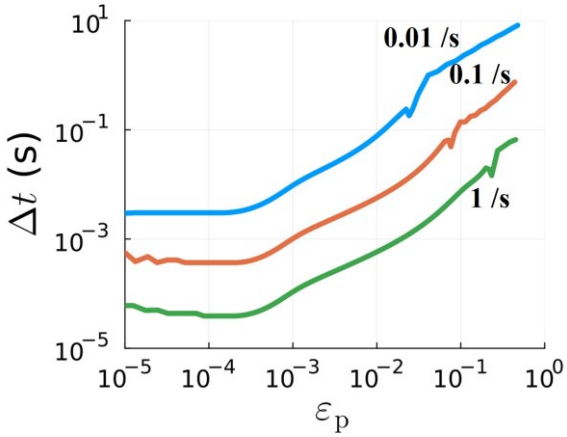
(a) Stiffness index S_1 versus plastic strain ε_p



(b) Stiffness index S_3 versus plastic strain ε_p



(c) Stress σ versus strain ε_p



(d) Step size Δt versus plastic strain ε_p

Figure 6.8 Computations of constitutive equations SET 3, at three different strain rates given by $\dot{\varepsilon}_T = [0.01, 0.1, 1]$ /s and at a temperature of 693 K for the time interval of $0 \leq t \leq \frac{0.5}{\dot{\varepsilon}_T}$ s.

Compared to equation SETs 1 and 2, equation SET 3 exhibits the most severe numerical stiffness, as seen in Figure 6.8(a) and (b), in which, for all the strain rates, S_3 is higher than or equal to 10^5 over each solution trajectory. For equation SET 3 at a strain rate of $\dot{\varepsilon}_T = 0.1$ /s and a temperature of 693 K, the truncation error $\|\boldsymbol{e}\|$ is shown in the error-workload curves in Figure 6.9, which were used to benchmark each numerical method at comparable levels of accuracy within the tolerances of $10^{-4} \leq Tol_{\text{rel}} \leq 10^{-8}$ and $10^{-5} \leq Tol_{\text{abs}} \leq 10^{-9}$. As can be seen, despite the increased numerical stiffness, the R23 method minimises the truncation error associated with stress for low to medium accuracy. However, this method was outperformed by the RADAU5 method at high accuracy owing to its higher-order nature.

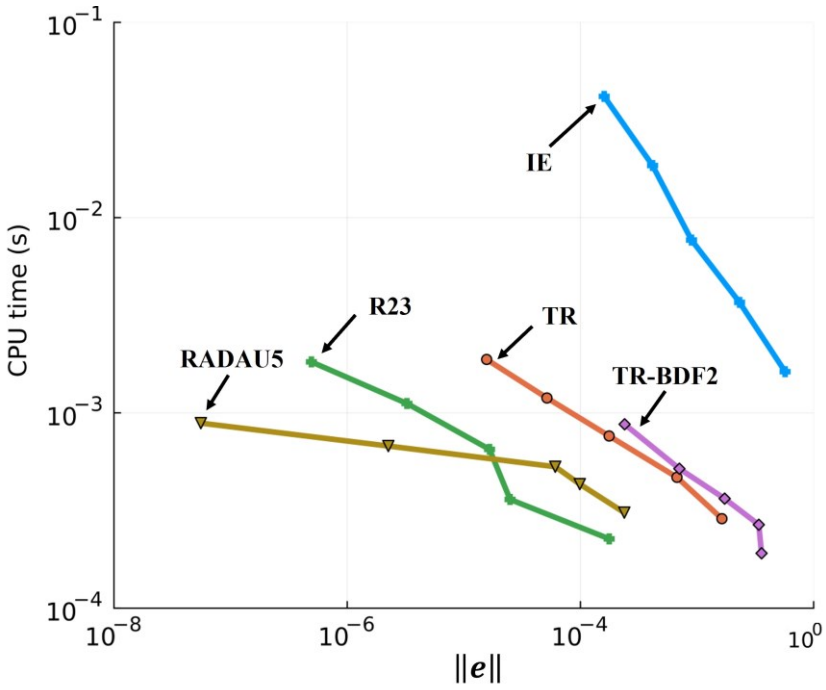


Figure 6.9 Numerical benchmarking of the five considered implicit integration methods (IE, TR, TR-BDF2, R23, and RADAU5) against equation SET 3 at $\dot{\varepsilon}_T = 0.1$ /s and 693 K for the time interval of $0 \leq t \leq 5$ s.

In summary, for equation SETs 1-3, the RADAU5 method produced the most computationally efficient solution. In addition, bottlenecks arising from the nonlinear differential equations have been found to be efficiently solved, allowing efficient numerical integration. It should be noted that, in this study, the numerical integration methods were exclusively applied to the equations, which describe the deformation processes under the simple loading condition, uniaxial tension. In practical forming processes, high gradients of state variables may exist near certain surfaces and further research is required on their effects on the efficiency of this method.

6.5 Summary

A numerical analysis was performed to investigate the difficulties in the numerical integration of unified viscoplastic/creep constitutive equations, which are stiff ordinary differential equations (ODEs). Five implicit numerical integration methods, implicit Euler (IE), trapezoidal rule (TR), trapezoidal rule-backward differentiation formulae 2 (TR-BDF2), Rosenbrock23 (R23), and RADAU5, were analysed in this research, and a comparative study was undertaken to benchmark the efficiency and accuracy of these implicit methods on three sets of unified constitutive equations are numerically stiff. A novel method for detecting localised stiffness in constitutive equations was introduced and demonstrated to be effective for viscoplastic/creep-

ageing constitutive equations. The formulation of the stiffness index enables a more accurate assessment of the stiffness for unified constitutive equations, facilitating the selection of the most appropriate numerical method.

The IE method is simple and straightforward, thus making it easy to implement. However, it can be computationally more intensive and is outperformed by higher-order implicit methods, particularly for stiffer problems. The TR method provides higher accuracy but comes at the expense of decreased stability. The TR-BDF2 method is considered computationally efficient and reliable for most equation sets with moderate-to high stiffness, primarily because it ensures L-stability. Additionally, the bottlenecks arising from the nonlinear differential equations can be solved efficiently, allowing for efficient numerical integration. The R23 method has shown promise for moderately stiff systems where it can be computationally more efficient. However, this method requires the use of accurate numerical Jacobians. A higher-order method, RADAU5, has been found to be more effective and efficient in handling of stiff ODEs compared to the other implicit methods considered. However, the reduced stability region may limit the step size in some cases and involve a higher computational cost per step compared to lower-order methods.

In summary, each of the five implicit methods has strengths and weaknesses, and the selection of a method depends on the specific requirements of the application. However, for solving stiff ODEs, the RADAU5 method was found to be more effective and efficient than the other implicit methods considered. The research findings contribute to understanding which numerical methods are best suited for integration into finite element simulations, providing a foundation for future applications.

7 Conclusions and Future Work

7.1 Conclusions

This PhD thesis has explored the application of various mathematical methods to metal forming processes and the determination of constitutive properties for metal forming applications. A key contribution of this work is the integration of a Machine Learning (ML) approach for strain rate control, which has demonstrated significant advantages in thermomechanical testing procedures. When this is combined with accurate determination of the constitutive relationships, by effective integration processes, a more accurate representation of metal forming processes is achieved.

The main conclusions of this PhD thesis are summarised in the following subsections, covering four main aspects of the research:

7.1.1 Application of the machine learning approach

The study demonstrates the successful integration of the Gleeble thermomechanical material simulator with data-driven material modeling through LSTM (Long Short-Term Memory) neural networks for uniaxial tensile testing under hot stamping conditions. The ML approach effectively predicts non-homogeneous strain distributions under different deformation conditions and is useful in optimising the displacement-time relationship. This offers far superior strain rate control compared to traditional methods, highlighting the method's efficiency for use in thermomechanical testing. Therefore, this novel approach not only mitigates the inaccuracies attributed in the conventional SST (Stroke based Strain Testing) but also achieves far superior strain rates control. The data-driven machine learning approach was proven highly effective for controlling strain rate and the main finding was:

- The novel approach mitigates the inaccuracies in the conventional Stroke-based Strain Testing (SST) and achieves the Mean Absolute Percentage Error (MAPE) for strain rate less than 0.11 or 11%, while the MAPE for the conventional approach can be as high as 138%. The ML based SST results show an improvement of strain rate MAPE ranging between 91.3% to 94.1%.

7.1.2 Thermomechanical properties of AA6082 under HFQ

The finding on the application of machine learning on the thermomechanical properties of AA6082 under Hot Forming Quench (HFQ) are:

- The integration of ML ensures more accurate determination of material constants by maintaining a constant strain rate, avoiding the deviations seen in traditional methods, and ultimately improving the precision of constitutive models.
- The overall trend of flow stress is the same for the two approaches, i.e. increasing with decreasing temperature and increasing strain rate. The new approach allows more accurate determination of the material thermomechanical properties at various temperatures and strain rates. The strain rate using the conventional method can increase up to seven times the target strain rate as the test progresses, therefore leading to unreal strain hardening, whilst the experimental flow stress of AA6082 obtained using ML-approach shows much weaker hardening behaviour. The difference in flow stress can be as high as over 40 MPa.
- A hardening of between 20-50 MPa during plasticity was exhibited for the conventional based method of strain rate control and a hardening of less than 10 MPa was exhibited for the ML based method of strain rate control. Between the two methods the hardening percentage reduction between can be over 400%.
- This research underscored the potential of combining advanced constitutive modelling with machine learning techniques to achieve more robust and precise understanding of material behaviour. This approach is crucial for optimising manufacturing processes and advancing material design.

7.1.3 Unified constitutive equation determination

The main points raised in the Chapter are as follows:

- An analysis of the suitability of several constitutive models, including the Norton-Hoff model, the Johnson-Cook model, and ODE-based unified constitutive equations was performed. These models are essential for predicting how materials respond under different deformation conditions.

- The fitting of these models was performed using experimental stress-strain curves from the uniaxial deformation of aluminium alloy AA6082 under a wide range of deformation conditions.
- The study also emphasised the problems associated with determining accurate material constants accurately from experimental data strain with non-constant strain rate as common in Conventional approach, where the applied strain rate often deviates from the target strain rate, resulting in inaccuracies. By integrating machine learning into the testing process, near-constant strain rate control was achieved, effectively mitigating this issue and improving the accuracy of the models.
- A comparison was conducted between calibrated models based on data collected through the machine learning approach and conventional approach. A percentage difference of up to 600% was observed in the fitted parameters between the two methods.

7.1.4 Numerical integration

A numerical analysis was performed to investigate the difficulties in the numerical integration of unified viscoplastic/creep constitutive equations, which are stiff ordinary differential equations (ODEs). Five implicit numerical integration methods, implicit Euler (IE), trapezoidal rule (TR), trapezoidal rule-backward differentiation formulae 2 (TR-BDF2), Rosenbrock23 (R23), and RADAU5, were analysed in this research. A comparative study was undertaken to benchmark the efficiency and accuracy of these implicit methods on three sets of stiff unified constitutive equations. The key findings are as follows:

- A novel method for detecting localised stiffness in constitutive equations was introduced and demonstrated to be effective for viscoplastic/creep-ageing constitutive equations. The formulation of the stiffness index enables a more accurate assessment of the stiffness for unified constitutive equations, facilitating the selection of the most appropriate numerical method.
- The IE method and TR method were found to be ineffective due to their lower-order accuracy.
- The TR-BDF2 and R23 methods were considered computationally efficient and reliable for most equation sets with moderate-to high stiffness.

- Each of the five implicit methods has strengths and weaknesses, and choice of a method depends on the specific requirements of the application. However, for solving stiff ODEs, the RADAU5 method was found to be the most effective and efficient of those considered.

These research findings contribute to a better understanding of which numerical methods are best suited for integration into finite element simulations, laying a foundation for future applications.

7.2 Suggestions for future work

Whilst this study has demonstrated the effectiveness of machine learning techniques for strain rate control and constitutive modelling in aluminium alloy AA6082, future research could explore the extension of these techniques to different materials. Future work could focus on expanding the ML model to include more complex deformation conditions and additional material types where a more comprehensive dataset is developed that captures uniaxial and multiaxial loading. The effect of the orientation of the specimen from rolling direction could be consider anisotropic materials. Since mechanical properties can vary based on anisotropy in rolled materials, incorporating this factor into both experimental and ML-based approaches could improve the predictive accuracy of constitutive models under more diverse deformation scenarios.

The current research has primarily focused on uniaxial conditions. Future studies could apply machine learning techniques to analyses strain fields under biaxial testing conditions, which are more representative of real-world applications. By providing accurate strain rate control during biaxial tests, this approach could enhance the accuracy of Forming Limit Diagrams (FLD) and Fracture Forming Limit Diagrams (FFLD), offering more precise predictions of material failure limits in complex forming scenarios.

Utilising the accurately calibrated constitutive models, a high-fidelity simulation of the uniaxial testing process could be developed. These simulations would allow for a more detailed understanding of material behaviour under various strain rates and temperatures, providing valuable insights into material response that could be applied to further optimise testing and forming processes.

Appendix A

In material modelling, constitutive equations play a crucial role in describing the behaviour of materials under various loading conditions. These equations can be used to model how materials respond to different stresses, strains, temperatures and strain rates.

Material forming dataset for warm forming – SET 1

During warm forming processes, metallic workpiece/material is deformed under elastic-viscoplastic conditions. To model the elastic–viscoplastic deformation and material hardening, the following set of constitutive equations is proposed and determined for micro-alloyed air-quenched steel in warm/hot forming [90]:

$$\dot{\varepsilon}_{\mathrm{p}} = \left[\frac{\sigma - B\sqrt{\bar{\rho}} - k}{K}\right]_{+}^{n} \tag{A.1}$$

$$\dot{\bar{\rho}} = A(1-\bar{\rho})\dot{\varepsilon}_{\mathrm{p}} - C\bar{\rho}^{\gamma} \tag{A.2}$$

$$\dot{\sigma} = E\left(\dot{\varepsilon}_{\mathrm{T}} - \dot{\varepsilon}_{\mathrm{p}}\right) \tag{A.3}$$

where ε_{p} is the plastic strain, σ is the stress, and $\bar{\rho}$ is the normalised dislocation density. Here $\bar{\rho}$ is defined as: $\bar{\rho} = (\rho - \rho_{\mathrm{i}})/\rho_{\mathrm{s}}$ [63], where ρ_{i} is the initial dislocation density and ρ_{s} is the saturated dislocation density. In SET 1, evolution of strain is modelled by a power law relation, and evolution of normalised dislocation density is described by accumulation of dislocation due to plastic deformation $A\dot{\varepsilon}_{\mathrm{p}}$, annihilation due to dynamic recovery/recrystallisation $A\bar{\rho}\dot{\varepsilon}_{\mathrm{p}}$ and static recovery $C\bar{\rho}^{\gamma_0}$. Hooke's law is used to model the evolution of stress where E is the Young's modulus, and $\dot{\varepsilon}_{\mathrm{T}}$ is a constant quantity known as the strain rate. For example, the Equation (A.1-A.3) was used to model the hardening of micro-alloyed steel the determined values were presented in Table A.1 The material constants are determined for micro-alloyed air-quenching steel under warm forming conditions and they are listed in Table A.1 [92].

Table A.1 Determined material constants used to model elastic-viscoplastic deformation and material hardening of micro-alloyed steel at a temperature 1100 K.

k (MPa)	K (MPa)	n	A	C (/s)	γ_0	B (MPa)	E (Gpa)
0.34	51.67	1.31	10.49	0.25	1.01	200.18	110

Material dataset for creep ageing deformation of aluminium alloy – SET 2

The constitutive model for creep-ageing of aluminium alloy AA2050-T34 is a set of equations [63] which couple the creep strain rate that is controlled by the applied stress, as well as the increasing dislocation density, dissolving precipitates, new precipitates and other metallurgical and microstructural features in the alloy. This constitutive equation set is given below:

$$\dot{\varepsilon}_{\mathrm{cr}} = A_4 \sinh\big(B_1(\sigma - \sigma_{\mathrm{th0}})(1-H)\big)\mathrm{sign}(\sigma) \tag{A.4}$$

$$H = k_1\bar{\rho} + k_2\bar{c} + k_3\left(\bar{r}_{n2} + \beta^{\frac{1}{2}}\bar{r}_d\right) \tag{A.5}$$

$$\dot{\bar{r}}_{n2} = C_r(Q - \bar{r}_{n2})^{m3}(1 + \gamma_0\bar{\rho}^{m4}) \tag{A.6}$$

$$\dot{\bar{r}}_d = -\frac{C_{r1}}{\bar{r}_d} \tag{A.7}$$

$$\dot{\bar{c}} = -A_2(\bar{c} - \bar{c}_a)(1 + \gamma_0\bar{\rho}^{m4}) \tag{A.8}$$

$$\dot{\bar{\rho}} = A_1(1 - \bar{\rho})|\dot{\varepsilon}_{\mathrm{cr}}|^{m_1} - C_p\bar{\rho}^{m2} \tag{A.9}$$

$$\dot{\sigma}_{n2} = C_a\dot{\bar{r}}_{n2}^{m5}\left(1 - \bar{r}_{n2}{}^{m6}\right) \tag{A.10}$$

$$\dot{\sigma}_d = C_{a1}r_d^{m7}\,\dot{\bar{r}}_d \tag{A.11}$$

$$\dot{\sigma}_{ss} = -C_{ss}|\dot{\bar{c}}|^{m_5}(\bar{c} - \bar{c}_a) \tag{A.12}$$

$$\dot{\sigma}_{\mathrm{dis}} = A_3 n\bar{\rho}^{n-1}\dot{\bar{\rho}} \tag{A.13}$$

$$\sigma_y = \sigma_{\mathrm{ss}} + \sqrt{\sigma_{n2}^2 + \sigma_d^2 + \sigma_{\mathrm{dis}}^2} \tag{A.14}$$

where $\varepsilon_{\mathrm{cr}}$ is the creep strain, H is a microstructure-controlled creep variable, $\bar{r}_{n2}$, $\bar{r}_d$, $\bar{c}$ and $\bar{\rho}$ are the normalised microstructural variables representing the new precipitate radius, dissolving precipitate radius, solute concentration and dislocation density, σ_{n2}, σ_d, σ_{ss} and σ_{dis} are the strength contributions to the yield strength σ_y from new precipitates, dissolving precipitates, solutes and dislocations, respectively [63]. The nine dimensional system has $\boldsymbol{y} = [\varepsilon_{\mathrm{cr}}, \bar{r}_{n2}, \bar{r}_d, \bar{c}, \bar{\rho}, \sigma_{n2}, \sigma_d, \sigma_{\mathrm{ss}}, \sigma_{\mathrm{dis}}]^{\mathrm{T}}$, with intial conditions $\boldsymbol{y}_0$ = [0, 0, 1, 0.978, 10^{-6}, 0, 110, 120, 100]$^{\mathrm{T}}$ and with parameters $\boldsymbol{p} = \sigma$, where σ is the applied stress. With parameter β = 0.101, the determined material constants for equation SET 2 are listed in Table A.2 [63].

Table A.2 Determined material constants for creep-ageing of AA2050-T34 at 428 K.

$\bar{c}_a$	C_r (/hr)	Q	m_3	C_a (MPa)	m_5	m_6	C_{r1} (/hr)	C_{a1} (MPa)
0.316	0.108	1.1	1.25	180	0.65	6.5	0.108	120
m_7	A_2	C_{ss} (MPa)	m_8	A_1 (/hr)	m_1	m_2	C_p	A_3
0.10	0.45	40.0	0.02	1.7	0.03	2.1	0.07	12
n	A_4	B_1	k_1	k_2	k_3	γ_0	m_4	σ_{tho} (MPa)
0.8	4.5E-4	1.32E-2	0.618	0.622	0.226	0.08	1.28	18

Material forming dataset for recrystallisation of aluminium alloys - SET 3

A continuous dynamic recrystallisation (CDRX)-based constitutive model was developed for hot deformation of aluminium alloys [138] as shown below:

$$\dot{\varepsilon}_{\mathrm{p}} = A_1 \sinh[A_2(|\sigma| - H - k)] \cdot S_{\mathrm{HAB}}^{\gamma_d} \tag{A.15}$$

$$\dot{H} = {}^{1}\!/_{2}\, B \bar{\rho}^{-0.5} \dot{\bar{\rho}} \tag{A.16}$$

$$\dot{\bar{\rho}} = c_0 \left({}^{S_{\mathrm{HAB0}}}\!/_{S_{\mathrm{HAB}}}\right)^{\gamma_S} (1 - \bar{\rho}) \dot{\varepsilon}_{\mathrm{p}} - \alpha_1 \bar{\rho}^{c_1} - \alpha_2 S \bar{\rho}^{\gamma_\alpha} \tag{A.17}$$

$$\dot{S}_{\mathrm{HAB}} = c_2 S_{\mathrm{lab}} \dot{\bar{\theta}}_{\mathrm{sub}} \alpha_3 \bar{\rho}^{\gamma_{lab}} S_{\mathrm{lab}}^2 \bar{\theta}_{\mathrm{sub}}^{\gamma_\theta} \left(1 - \ln(\bar{\theta}_{\mathrm{sub}})\right) - \alpha_2 \bar{\rho}^{\gamma_{\mathrm{HAB}}} S_{\mathrm{HAB}}^2 \tag{A.18}$$

$$\dot{S}_{\mathrm{lab}} = \alpha_4 \bar{\rho}^{\gamma_1} \dot{\varepsilon}_{\mathrm{p}} - c_2 S_{lab} \dot{\bar{\theta}}_{\mathrm{sub}} \alpha_3 \bar{\rho}^{\gamma_{lab}} S_{lab}^2 \bar{\theta}_{sub}^{\gamma_\theta} \left(1 - \ln(\bar{\theta}_{\mathrm{sub}})\right) - \alpha_5 S_{\mathrm{lab}} S_{\mathrm{HAB}} \bar{\rho}^{\gamma_{\mathrm{HAB}}} \quad \text{(A.19)}$$

$$\dot{\bar{\theta}}_{\mathrm{sub}} = \alpha_6 \bar{\rho}^{\gamma_2} \dot{\varepsilon}_p S_{\mathrm{lab}}^2 \bar{\theta}_{\mathrm{sub}} (\theta_r \bar{\theta}_{\mathrm{sub}} - 1) \ln(n \cdot \bar{\theta}_{\mathrm{sub}}) \quad \text{(A.20)}$$

$$\dot{\sigma} = E\left(\dot{\varepsilon}_{\mathrm{T}} - \dot{\varepsilon}_{\mathrm{p}}\right) \quad \text{(A.21)}$$

$$S = S_{\mathrm{HAB}} + S_{\mathrm{lab}} \quad \text{(A.22)}$$

$$f_{\mathrm{HAB}} = {S_{\mathrm{HAB}}}/{S} \quad \text{(A.23)}$$

$$d = 2/S_{\mathrm{HAB}} \quad \text{(A.24)}$$

where T is the temperature, $\dot{\varepsilon}_{\mathrm{T}}$ is the total strain rate determining the deformation conditions, ε_{p} is the plastic strain, H is the primary hardening, $\bar{\rho}$ is the normalised dislocation, S_{HAB} is area of high angle grain boundaries per unit volume, S_{lab} is area of low angle grain boundaries per unit volume and σ is the stress. State variables are $\boldsymbol{y} = [\varepsilon_{\mathrm{p}}, H, \bar{\rho}, \mathrm{S_{HAB}}, \mathrm{S_{lab}}, \bar{\theta}_{\mathrm{sub}}, \sigma]^{\mathrm{T}}$, and initial conditions are set to $\boldsymbol{y}_0$ = [0, 0, 10^{-6}, 0.035, 0.0045, 0.133, 0]$^{\mathrm{T}}$. Dependant parameters determining the deformation conditions are $\boldsymbol{p} = [T, \dot{\varepsilon}_{\mathrm{T}}]^{\mathrm{T}}$. With parameters $n = \frac{\theta_{\mathrm{c}}}{\theta_{\mathrm{m}}}$ and $\theta_r = \frac{\theta_{\mathrm{c}}}{\theta_{\mathrm{sat}}}$, the temperature-dependent parameters are given by the following relations:

$$E = E_0 \exp\left(-K_g T\right) \quad \text{(A.25)}$$

$$B = -c_B T + B_0 \quad \text{(A.26)}$$

$$k = -c_k T + k_0 \quad \text{(A.27)}$$

$$\alpha_1 = c_{\alpha 1} \exp\left(-\frac{Q_a}{RT}\right) \quad \text{(A.28)}$$

$$\alpha_2 = \frac{C_{\alpha_2}}{T} \exp\left(-K_g T - \frac{Q_b}{RT}\right) \quad \text{(A.29)}$$

$$\alpha_3 = \frac{C_{\alpha_3}}{T} \exp\left(-K_g T - \frac{Q_b}{RT}\right) \quad \text{(A.30)}$$

$$\alpha_4 = c_{\alpha_4} \exp\left(-\frac{Q_a}{RT}\right) \quad \text{(A.31)}$$

$$\alpha_5 = c_{\alpha_5} \exp\left(-\frac{Q_a}{RT}\right) \tag{A.32}$$

$$\alpha_6 = c_{\alpha_6} \exp\left(-\frac{Q_a}{RT}\right) \tag{A.33}$$

where, T in K is temperature and all other determined material constants used in the model are listed in Table A.3 [138].

Table A.3 List of the constant values used for the set of CDRX equations for AA7050.

A_1 (/s)	A_2 (/MPa)	R (J/mol)	K_g	c_0	c_1	c_2	γ_1
8.2E-4	0.15	8.31	5.40E-4	15.00	1.15	0.70	0.70
γ_2	γ_s	γ_d	γ_θ	γ_{lab}	γ_{HAB}	γ_α	n
0.15	5.00	0.01	6.18	0.77	2.10	4.20	0.75
$c_{\alpha 1}$ (/s)	$c_{\alpha 2}$ (μm·K/s)	$c_{\alpha 3}$ (μm·K/s)	$c_{\alpha 4}$ (/μm)	$c_{\alpha 5}$ (/μm)	$c_{\alpha 6}$ (μm^2)	Q_a (J/mol)	Q_b (J/mol)
38.11	2.92E+2	1.46E+7	14.15	2.00E+3	1.61E+5	1.78E+4	1.34E+4
E_0 (MPa)	θ_c	θ_m	θ_{sat}	c_B (MPa/K)	c_k (MPa/K)	B_0 (MPa)	k_0 (MPa)
7E+4	15.00	20.00	6.00	0.40	0.14	2.96E+2	1.12E+2

References

[1] M. Martinón-Torres, X. J. Li, A. Bevan, Y. Xia, Z. Kun, and T. Rehren, "Making weapons for the Terracotta Army," *Archaeology International,* vol. 13, pp. 65-67, 2011.

[2] M. El-Shennawy, K. Abdel-Aziz, and A. Omar, "Metallurgical and mechanical properties of heat treatable aluminum alloy AA6082 welds," *International Journal of Applied Engineering Research,* vol. 12, no. 11, pp. 2832-2839, 2017.

[3] Y. Ono and T. Yokoyama, "Determination of local constitutive behavior of AA6061–T6 friction stir welds using digital image correlation," *Proceedings of the Institution of Mechanical Engineers, Part L: Journal of Materials: Design and Applications,* vol. 236, no. 8, pp. 1574-1589, 2022, doi: 10.1177/14644207221075467.

[4] K. Liu, S. Wang, L. Pan, and X.-G. Chen, "Thermo-Mechanical Fatigue Behavior and Resultant Microstructure Evolution in Al-Si 319 and 356 Cast Alloys," *Materials,* vol. 16, no. 2, p. 829, 2023. [Online]. Available: https://www.mdpi.com/1996-1944/16/2/829.

[5] E. Kardoulaki, J. Lin, D. Balint, and D. Farrugia, "Investigation of the effects of thermal gradients present in Gleeble high-temperature tensile tests on the strain state for free cutting steel," *The Journal of Strain Analysis for Engineering Design,* vol. 49, no. 7, pp. 521-532, 2014, doi: https://doi.org/10.1177/0309324714531950.

[6] Y. Li, S. Li, Y. Chen, and G. Han, "Constitutive parameters identification based on DIC assisted thermo-mechanical tensile test for hot stamping of boron steel," *Journal of Materials Processing Technology,* vol. 271, pp. 429-443, 2019/09/01/ 2019, doi: https://doi.org/10.1016/j.jmatprotec.2019.04.020.

[7] J. Rakhmonov *et al.*, "A New Approach to Determine Tensile Stress-Strain Evolution in Semi-Solid State at Near-Solidus Temperature of Aluminum Alloys," *Metals,* vol. 11, no. 3, p. 396, 2021. [Online]. Available: https://www.mdpi.com/2075-4701/11/3/396.

[8] N. Li, Z. T. Shao, J. G. Lin, and T. A. Dean, "Investigation of uniaxial tensile properties of AA6082 under HFQ® conditions," *Key Engineering Materials,* vol. 716, pp. 337-344, 2016.

[9] R. Zhang, Z. Shao, J. Lin, and T. Dean, "Measurement and analysis of heterogeneous strain fields in uniaxial tensile tests for boron steel under hot stamping conditions," *Experimental Mechanics,* vol. 60, no. 9, pp. 1289-1300, 2020.

[10] "IEA, Global CO2 emissions from transport by sub-sector in the Net Zero Scenario, 2000-2030, IEA, Paris." IEA. Licence: CC BY 4.0. https://www.iea.org/energy-system/transport (accessed 23/06/24.

[11] "Aluminium Industry's Contribution to the UN SDGs," The International Aluminium Institute, 2020. Accessed: 23/06/24. [Online]. Available: https://international-aluminium.org/wp-content/uploads/2022/12/Aluminium-Industrys-Contribution-to-the-UN-SDGs-FINAL.pdf

[12] H. Ritchie, P. Rosado, and M. Roser. "Breakdown of carbon dioxide, methane and nitrous oxide emissions by sector." https://ourworldindata.org/emissions-by-sector (accessed.

[13] A. L. C. Ferrer and A. M. T. Thomé, "Carbon emissions in transportation: A synthesis framework," *Sustainability,* vol. 15, no. 11, p. 8475, 2023.

[14] J. G. Lenard, *Primer on flat rolling*. Newnes, 2013.

[15] R. J. H. Wanhill, "Chapter 15 - Aerospace Applications of Aluminum–Lithium Alloys," in *Aluminum-lithium Alloys*, N. Eswara Prasad, A. A. Gokhale, and R. J. H. Wanhill Eds. Boston: Butterworth-Heinemann, 2014, pp. 503-535.
[16] S. Hegde, B. Satish Shenoy, and K. N. Chethan, "Review on carbon fiber reinforced polymer (CFRP) and their mechanical performance," *Materials Today: Proceedings,* vol. 19, pp. 658-662, 2019/01/01/ 2019, doi: https://doi.org/10.1016/j.matpr.2019.07.749.
[17] J. J. d. G. Venezuela, "The influence of hydrogen on MS980, MS1180, MS1300 and MS1500 martensitic advanced high strength steels used for automotive applications," School of Mechanical and Mining Engineering, University of Queensland, 2017.
[18] W. Miller *et al.*, "Recent development in aluminium alloys for the automotive industry," *Materials Science and Engineering: A,* vol. 280, no. 1, pp. 37-49, 2000.
[19] D. Carle and G. Blount, "The suitability of aluminium as an alternative material for car bodies," *Materials & design,* vol. 20, no. 5, pp. 267-272, 1999.
[20] F. Khan *et al.*, "Advances of composite materials in automobile applications – A review," *Journal of Engineering Research,* 2024/02/27/ 2024, doi: https://doi.org/10.1016/j.jer.2024.02.017.
[21] Y. Li, Z. Lin, A. Jiang, and G. Chen, "Use of high strength steel sheet for lightweight and crashworthy car body," *Materials & Design,* vol. 24, no. 3, pp. 177-182, 2003/05/01/ 2003, doi: https://doi.org/10.1016/S0261-3069(03)00021-9.
[22] M. Esmaily *et al.*, "Fundamentals and advances in magnesium alloy corrosion," *Progress in Materials Science,* vol. 89, pp. 92-193, 2017/08/01/ 2017, doi: https://doi.org/10.1016/j.pmatsci.2017.04.011.
[23] V. Capitalist. "All the Metals We Mined in One Visualization." https://www.visualcapitalist.com/all-the-metals-we-mined-in-one-visualization/ (accessed 23/04/24.
[24] P. A. P. IAI, "International Aluminium Institute," *United Kingdom,* 2021.
[25] G. Xiao and Z. Zan, "Hot Stamping Process Simulation of 22MnB5 Steel Based on Identified Heat Boundary Condition," in *IOP Conference Series: Earth and Environmental Science*, 2021, vol. 692, no. 2: IOP Publishing, p. 022080.
[26] M. S. Mohamed, A. D. Foster, J. Lin, D. S. Balint, and T. A. Dean, "Investigation of deformation and failure features in hot stamping of AA6082: Experimentation and modelling," *International Journal of Machine Tools and Manufacture,* vol. 53, no. 1, pp. 27-38, 2012/02/01/ 2012, doi: https://doi.org/10.1016/j.ijmachtools.2011.07.005.
[27] N. Li, Z. T. Shao, J. G. Lin, and T. A. Dean, "Investigation of uniaxial tensile properties of AA6082 under HFQ® conditions," in *Key Engineering Materials*, 2016, vol. 716: Trans Tech Publ, pp. 337-344.
[28] A. Norrbottens Jaernverk, "Manufacturing a hardened steel article," *GB1490535,* 1977.
[29] G. Berglund, "The history of hardening of boron steel in northern Sweden," in *1st international conference on hot sheet metal forming of high-performance steel, Kassel, Germany*, 2008, pp. 175-177.
[30] C. Tong *et al.*, "New Developments and Future Trends in Low-Temperature Hot Stamping Technologies: A Review," *Metals,* vol. 10, no. 12, p. 1652, 2020. [Online]. Available: https://www.mdpi.com/2075-4701/10/12/1652.
[31] R. E. Reed-Hill, R. Abbaschian, and R. Abbaschian, *Physical metallurgy principles*. Van Nostrand New York, 1973.
[32] K. Zheng *et al.*, "The effect of hot form quench (HFQ®) conditions on precipitation and mechanical properties of aluminium alloys," *Materials Science and Engineering:*

A, vol. 761, p. 138017, 2019/07/22/ 2019, doi: https://doi.org/10.1016/j.msea.2019.06.027.
[33] A. Association, *Aluminum: properties and physical metallurgy*. ASM international, 1984.
[34] A. Foster, T. A. Dean, and J. Lin, "Process for forming aluminium alloy sheet components," ed: Google Patents, 2020.
[35] M. Raugei, O. El Fakir, L. Wang, J. Lin, and D. Morrey, "Life cycle assessment of the potential environmental benefits of a novel hot forming process in automotive manufacturing," *Journal of Cleaner Production,* vol. 83, pp. 80-86, 2014.
[36] J. Sarkar, R. Bhattacharya, S. Mandal, N. Mishra, and N. Singh, "Study of Electrochemical Behaviour of Aluminium Alloys of Various Tempers," 2015.
[37] E. Hsu, J. E. Carsley, and R. Verma, "Development of forming limit diagrams of aluminum and magnesium sheet alloys at elevated temperatures," *Journal of materials engineering and performance,* vol. 17, pp. 288-296, 2008.
[38] Z. Shao, N. Li, J. Lin, and T. A. Dean, "Development of a New Biaxial Testing System for Generating Forming Limit Diagrams for Sheet Metals Under Hot Stamping Conditions," *Experimental Mechanics,* vol. 56, no. 9, pp. 1489-1500, 2016/11/01 2016, doi: 10.1007/s11340-016-0183-9.
[39] T. M. Mitchell, "Does machine learning really work?," *AI magazine,* vol. 18, no. 3, pp. 11-11, 1997.
[40] F. Pedregosa *et al.*, "Scikit-learn: Machine learning in Python," *the Journal of machine Learning research,* vol. 12, pp. 2825-2830, 2011.
[41] N. Ketkar and N. Ketkar, "Introduction to keras," *Deep learning with python: a hands-on introduction,* pp. 97-111, 2017.
[42] R. Perrault and J. Clark, "Artificial Intelligence Index Report 2024," 2024.
[43] "Google Scholar." https://scholar.google.com (accessed 20/05/2024.
[44] Z.-Y. Zhang, W. Liu, P.-F. Li, J.-P. Zhang, and L.-Y. Fan, "A numerical control machining tool path step error prediction method based on BP neural network," *Scientific Reports,* vol. 13, no. 1, p. 16347, 2023/09/28 2023, doi: 10.1038/s41598-023-43617-6.
[45] B. Mahesh, "Machine learning algorithms-a review," *International Journal of Science and Research (IJSR).[Internet],* vol. 9, no. 1, pp. 381-386, 2020.
[46] I. H. Sarker, "Deep Learning: A Comprehensive Overview on Techniques, Taxonomy, Applications and Research Directions," *SN Computer Science,* vol. 2, no. 6, p. 420, 2021/08/18 2021, doi: 10.1007/s42979-021-00815-1.
[47] Y. Yu, X. Si, C. Hu, and J. Zhang, "A review of recurrent neural networks: LSTM cells and network architectures," *Neural computation,* vol. 31, no. 7, pp. 1235-1270, 2019.
[48] H. Salehinejad, S. Sankar, J. Barfett, E. Colak, and S. Valaee, "Recent advances in recurrent neural networks," *arXiv preprint arXiv:1801.01078,* 2017.
[49] J. Chung, S. Ahn, and Y. Bengio, "Hierarchical multiscale recurrent neural networks," *arXiv preprint arXiv:1609.01704,* 2016.
[50] Y. Hu, X. Sun, X. Nie, Y. Li, and L. Liu, "An Enhanced LSTM for Trend Following of Time Series," *IEEE Access,* vol. 7, pp. 34020-34030, 2019, doi: 10.1109/ACCESS.2019.2896621.
[51] D. P. Kingma and J. Ba, "Adam: A method for stochastic optimization," *arXiv preprint arXiv:1412.6980,* 2014.
[52] S. J. Reddi, S. Kale, and S. Kumar, "On the convergence of adam and beyond," *arXiv preprint arXiv:1904.09237,* 2019.

[53] M. Torres-Velázquez, W. J. Chen, X. Li, and A. B. McMillan, "Application and Construction of Deep Learning Networks in Medical Imaging," *IEEE Transactions on Radiation and Plasma Medical Sciences,* vol. 5, no. 2, pp. 137-159, 2021, doi: 10.1109/TRPMS.2020.3030611.

[54] H. Sharma, M. Patil, and C. Woolsey, "A review of structure-preserving numerical methods for engineering applications," *Computer Methods in Applied Mechanics and Engineering,* vol. 366, p. 113067, 2020/07/01/ 2020, doi: https://doi.org/10.1016/j.cma.2020.113067.

[55] D. Kochkov, J. A. Smith, A. Alieva, Q. Wang, M. P. Brenner, and S. Hoyer, "Machine learning–accelerated computational fluid dynamics," *Proceedings of the National Academy of Sciences,* vol. 118, no. 21, p. e2101784118, 2021.

[56] Y. Miyazawa, F. Briffod, T. Shiraiwa, and M. Enoki, "Prediction of Cyclic Stress–Strain Property of Steels by Crystal Plasticity Simulations and Machine Learning," *Materials,* vol. 12, no. 22, p. 3668, 2019. [Online]. Available: https://www.mdpi.com/1996-1944/12/22/3668.

[57] D. Merayo, A. Rodríguez-Prieto, and A. M. Camacho, "Topological Optimization of Artificial Neural Networks to Estimate Mechanical Properties in Metal Forming Using Machine Learning," *Metals,* vol. 11, no. 8, p. 1289, 2021. [Online]. Available: https://www.mdpi.com/2075-4701/11/8/1289.

[58] M. Hu *et al.*, "Prediction of Mechanical Properties of Wrought Aluminium Alloys Using Feature Engineering Assisted Machine Learning Approach," *Metallurgical and Materials Transactions A,* vol. 52, no. 7, pp. 2873-2884, 2021/07/01 2021, doi: 10.1007/s11661-021-06279-5.

[59] R. Liu, Y. C. Yabansu, A. Agrawal, S. R. Kalidindi, and A. N. Choudhary, "Machine learning approaches for elastic localization linkages in high-contrast composite materials," *Integrating Materials and Manufacturing Innovation,* vol. 4, pp. 192-208, 2015.

[60] M. Raj, S. Thakre, R. K. Annabattula, and A. K. Kanjarla, "Estimation of local strain fields in two-phase elastic composite materials using UNet-based deep learning," *Integrating Materials and Manufacturing Innovation,* vol. 10, pp. 444-460, 2021.

[61] S. H. Adarsh and V. Sampath, "Prediction of high temperature deformation characteristics of an Fe-based shape memory alloy using constitutive and artificial neural network modelling," *Materials Today Communications,* vol. 22, p. 100841, 2020/03/01/ 2020, doi: https://doi.org/10.1016/j.mtcomm.2019.100841.

[62] Z. Ding, H. R. Attar, H. Wang, H. Liu, and N. Li, "Integrating convolutional neural network and constitutive model for rapid prediction of stress-strain curves in fibre reinforced polymers: A generalisable approach," *Materials & Design,* vol. 241, p. 112849, 2024/05/01/ 2024, doi: https://doi.org/10.1016/j.matdes.2024.112849.

[63] Y. Li, Z. Shi, J. Lin, Y.-L. Yang, and Q. Rong, "Extended application of a unified creep-ageing constitutive model to multistep heat treatment of aluminium alloys," *Materials & Design,* vol. 122, pp. 422-432, 2017, doi: https://doi.org/10.1016/j.matdes.2017.03.023.

[64] S. Alexandrov and Y.-R. Jeng, "Singular rigid/plastic solutions in anisotropic plasticity under plane strain conditions," *Continuum Mechanics and Thermodynamics,* vol. 25, no. 5, pp. 685-689, 2013/09/01 2013, doi: 10.1007/s00161-013-0304-y.

[65] J. Lechler, M. Merklein, and M. Geiger, "Determination of Thermal and Mechanical Material Properties of Ultra-High Strength Steels for Hot Stamping," *steel research*

international, vol. 79, no. 2, pp. 98-104, 2008, doi: https://doi.org/10.1002/srin.200806323.
[66] L. Li *et al.*, "Mechanical behavior and modeling of grinding force: A comparative analysis," *Journal of Manufacturing Processes,* vol. 102, pp. 921-954, 2023/09/29/ 2023, doi: https://doi.org/10.1016/j.jmapro.2023.07.074.
[67] J. H. Hollomon, "Tensile Deformation," *Transactions of the Metallurgical Society of AIME*.
[68] R. H. Wagoner and J.-L. Chenot, *Metal forming analysis*. Cambridge University Press, 2001.
[69] M. Umemoto, K. Tsuchiya, Z. G. Liu, and S. Sugimoto, "Tensile stress-strain analysis of single-structure steels," *Metallurgical and Materials Transactions A,* vol. 31, no. 7, pp. 1785-1794, 2000/07/01 2000, doi: 10.1007/s11661-006-0249-x.
[70] J. Lechler, M. Merklein, and M. Geiger, "Determination of thermal and mechanical material properties of ultra-high strength steels for hot stamping," *steel research international,* vol. 79, no. 2, pp. 98-104, 2008.
[71] A. Saxena, S. P. Dwivedi, A. Kumaraswamy, A. K. Srivastava, and N. K. Maurya, "Influence of SD effect on Johnson–Cook hardening constitutive material model: numerical and experimental investigation for armor steel," *Mechanics of Advanced Materials and Structures,* vol. 29, no. 2, pp. 285-302, 2022.
[72] W. Zhou, J. Lin, D. S. Balint, and T. A. Dean, "Clarification of the effect of temperature and strain rate on workpiece deformation behaviour in metal forming processes," *International Journal of Machine Tools and Manufacture,* vol. 171, pp. 1-6, 2021, doi: https://doi.org/10.1016/j.ijmachtools.2021.103815.
[73] J. Lin and T. Dean, "Modelling of microstructure evolution in hot forming using unified constitutive equations," *Journal of Materials Processing Technology,* vol. 167, no. 2-3, pp. 354-362, 2005, doi: https://doi.org/10.1016/j.jmatprotec.2005.06.026.
[74] E. Hairer, S. P. Norsett, and G. Wanner, *Solving Ordinary, Differential Equations I, Nonstiff problems* (Springer Series in Computational Mathematics). Springer, Berlin, Heidelberg, 1993, p. 528.
[75] L. Bonaventura and A. Della Rocca, "Monotonicity, positivity and strong stability of the TR-BDF2 method and of its SSP extensions," *arXiv preprint: 1510.04303,* 2015, doi: https://doi.org/10.48550/arXiv.1510.04303.
[76] C. A. Kennedy and M. H. Carpenter, "Diagonally implicit Runge–Kutta methods for stiff ODEs," *Applied Numerical Mathematics,* vol. 146, pp. 221-244, 2019, doi: https://doi.org/10.1016/j.apnum.2019.07.008.
[77] S. Kumar and B. P. Patel, "A novel accurate and computationally efficient integration approach to viscoplastic constitutive model," *International Journal for Numerical Methods in Engineering,* vol. 122, no. 1, pp. 219-234, 2021, doi: https://doi.org/10.1002/nme.6534.
[78] J. Lin, J. Cao, and D. Balint, "Development and determination of unified viscoplastic constitutive equations for predicting microstructure evolution in hot forming processes," *International Journal of Mechatronics and Manufacturing Systems,* vol. 4, no. 5, pp. 387-401, 2011.
[79] J. Lin, M. Mohamed, D. Balint, and T. Dean, "The development of continuum damage mechanics-based theories for predicting forming limit diagrams for hot stamping applications," *International Journal of Damage Mechanics,* vol. 23, no. 5, pp. 684-701, 2014, doi: https://doi.org/10.1177/1056789513507731.

[80] W. Zhou, J. Lin, D. S. Balint, and T. A. Dean, "Clarification of the effect of temperature and strain rate on workpiece deformation behaviour in metal forming processes," *International Journal of Machine Tools and Manufacture,* vol. 171, p. 103815, 2021/12/01/ 2021, doi: https://doi.org/10.1016/j.ijmachtools.2021.103815.

[81] D. Wen *et al.*, "Hot tensile behavior of a low-alloyed ultrahigh strength steel: Fracture mechanism and physically-based constitutive model," *Journal of Materials Research and Technology,* vol. 13, pp. 1684-1697, 2021, doi: https://doi.org/10.1016/j.jmrt.2021.05.100.

[82] R. A. Barrett, P. O'Donoghue, and S. B. Leen, "An improved unified viscoplastic constitutive model for strain-rate sensitivity in high temperature fatigue," *International Journal of Fatigue,* vol. 48, pp. 192-204, 2013, doi: https://doi.org/10.1016/j.ijfatigue.2012.11.001.

[83] M. Agoras and P. P. Castañeda, "Anisotropic finite-strain models for porous viscoplastic materials with microstructure evolution," *International Journal of Solids and Structures,* vol. 51, no. 5, pp. 981-1002, 2014, doi: https://doi.org/10.1016/j.ijsolstr.2013.11.025.

[84] X. Fan, H. Yang, and P. Gao, "Prediction of constitutive behavior and microstructure evolution in hot deformation of TA15 titanium alloy," *Materials & Design,* vol. 51, pp. 34-42, 2013, doi: https://doi.org/10.1016/j.matdes.2013.03.103.

[85] G. Li, H. Ding, and J. Wang, "A new set of physically-based unified viscoplastic constitutive equations for superplastic deformation of Al-Zn-Mg-Cu alloy," *Mechanics Research Communications,* vol. 123, p. 103904, 2022, doi: https://doi.org/10.1016/j.mechrescom.2022.103904.

[86] T. Dewen, P. Cong, and Z. Jiayu, "Finite element simulation of high-speed finish milling of SKD11 hardened steel based on modified constitutive equation," *Cogent Engineering,* vol. 5, no. 1, p. 1482589, 2018/01/01 2018, doi: https://doi.org/10.1080/23311916.2018.1482589.

[87] S. Davenport, N. Silk, C. Sparks, and C. M. Sellars, "Development of constitutive equations for modelling of hot rolling," *Materials Science and Technology,* vol. 16, no. 5, pp. 539-546, 2000, doi: https://doi.org/10.1179/026708300101508045.

[88] M. Abspoel, B. M. Neelis, and P. van Liempt, "Constitutive behaviour under hot stamping conditions," *Journal of Materials Processing Technology,* vol. 228, pp. 34-42, 2016, doi: https://doi.org/10.1016/j.jmatprotec.2015.05.007.

[89] W. Zhou, J. Lin, T. A. Dean, and L. Wang, "Feasibility studies of a novel extrusion process for curved profiles: experimentation and modelling," *International Journal of Machine Tools and Manufacture,* vol. 126, pp. 27-43, 2018, doi: https://doi.org/10.1016/j.ijmachtools.2017.12.001.

[90] B. Li, J. Lin, and X. Yao, "A novel evolutionary algorithm for determining unified creep damage constitutive equations," *International Journal of Mechanical Sciences,* vol. 44, no. 5, pp. 987-1002, 2002, doi: https://doi.org/10.1016/S0020-7403(02)00021-8.

[91] M. S. Mohamed, J. Lin, L. Wang, and D. Balint, "Hybrid forming processes for production of lightweight high strength automotive panel parts," *International Heat Treatment and Surface Engineering,* vol. 4, no. 4, pp. 160-165, 2010/12/01 2010, doi: 10.1179/174951410X12851626813014.

[92] J. Cao, J. Lin, and T. Dean, "An implicit unitless error and step-size control method in integrating unified viscoplastic/creep ODE-type constitutive equations," *International*

journal for numerical methods in engineering, vol. 73, no. 8, pp. 1094-1112, 2008, doi: https://doi.org/10.1002/nme.2112.

[93] G. D. Byrne and A. C. Hindmarsh, "Stiff ODE solvers: A review of current and coming attractions," *Journal of Computational physics,* vol. 70, no. 1, pp. 1-62, 1987, doi: https://doi.org/10.1016/0021-9991(87)90001-5.

[94] A. Sandu *et al.*, "Benchmarking stiff ode solvers for atmospheric chemistry problems-I. implicit vs explicit," *Atmospheric environment,* vol. 31, no. 19, pp. 3151-3166, 1997, doi: https://doi.org/10.1016/S1352-2310(97)00059-9.

[95] D. I. Ketcheson, "Highly efficient strong stability-preserving Runge–Kutta methods with low-storage implementations," *SIAM Journal on Scientific Computing,* vol. 30, no. 4, pp. 2113-2136, 2008, doi: https://doi.org/10.1137/07070485X.

[96] L. F. Shampine and M. W. Reichelt, "The matlab ode suite," *SIAM journal on scientific computing,* vol. 18, no. 1, pp. 1-22, 1997, doi: https://doi.org/10.1137/S1064827594276424.

[97] J. Dear, Z. Shi, and J. Lin, "An efficient numerical integration system for stiff unified constitutive equations for metal forming applications," in *IOP Conference Series: Materials Science and Engineering*, 2022, vol. 1270, no. 1: IOP Publishing, p. 012008, doi: https://doi.org/10.1088/1757-899X/1270/1/012008.

[98] N. Gunantara, "A review of multi-objective optimization: Methods and its applications," *Cogent Engineering,* vol. 5, no. 1, p. 1502242, 2018/01/01 2018, doi: https://doi.org/10.1080/23311916.2018.1502242.

[99] O. S. Odebiyi, S. M. Adedayo, L. A. Tunji, and M. O. Onuorah, "A review of weldability of carbon steel in arc-based welding processes," *Cogent Engineering,* vol. 6, no. 1, p. 1609180, 2019/01/01 2019, doi: https://doi.org/10.1080/23311916.2019.1609180.

[100] K. Xue, W. Tian, S. Yan, H. Zhu, and P. Li, "A Unified Constitutive Model for CLAM Steel Coupling Microstructure Evolution and Considering Phase Transformation in a Wide Range of Temperatures," *Transactions of the Indian Institute of Metals,* vol. 76, no. 4, pp. 1061-1073, 2023, doi: https://doi.org/10.1007/s12666-022-02809-w.

[101] A. Narayanan, K. Dubey, C. Davies, and J. Dear, "The creep of alloy 617 at 700° C: Material properties, measurement of strain and comparison between finite element analysis and digital image correlation," *International Journal of Solids and Structures,* vol. 129, pp. 195-203, 2017, doi: https://doi.org/10.1016/j.ijsolstr.2017.08.021.

[102] T. Simos, "Exponentially fitted Runge–Kutta methods for the numerical solution of the Schrödinger equation and related problems," *Computational Materials Science,* vol. 18, no. 3-4, pp. 315-332, 2000, doi: http://dx.doi.org/10.1016/S0010-4655(00)00080-1.

[103] S. Dharmaraja, Y. Wang, and G. Strang, "Optimal stability for trapezoidal–backward difference split-steps," *IMA journal of numerical analysis,* vol. 30, no. 1, pp. 141-148, 2010, doi: https://doi.org/10.1093/imanum/drp022.

[104] J. Butcher and D. Chen, "A new type of singly-implicit Runge–Kutta method," *Applied numerical mathematics,* vol. 34, no. 2-3, pp. 179-188, 2000, doi: https://doi.org/10.1016/S0168-9274(99)00126-9.

[105] M. Hosea and L. Shampine, "Analysis and implementation of TR-BDF2," *Applied Numerical Mathematics,* vol. 20, no. 1-2, pp. 21-37, 1996, doi: https://doi.org/10.1016/0168-9274(95)00115-8.

[106] E. Hairer and G. Wanner, "Stiff differential equations solved by Radau methods," *Journal of Computational and Applied Mathematics,* vol. 111, no. 1-2, pp. 93-111, 1999, doi: https://doi.org/10.1016/S0377-0427(99)00134-X.

[107] R. Zhang, Z. Shi, V. A. Yardley, and J. Lin, "Experimental studies of necking and fracture limits of boron steel sheet under hot stamping conditions," *Journal of Materials Processing Technology,* vol. 302, p. 117481, 2022.
[108] Z. Shao, N. Li, J. Lin, and T. Dean, "Formability evaluation for sheet metals under hot stamping conditions by a novel biaxial testing system and a new materials model," *International Journal of Mechanical Sciences,* vol. 120, pp. 149-158, 2017.
[109] C. Tong *et al.*, "Investigation of the effect of initial states of medium-Mn steel on deformation behaviour under hot stamping conditions," *Materials Science and Engineering: A,* vol. 855, p. 143914, 2022.
[110] F. Kellogg, B. Butler, and A. R. L. A. P. G. MD, "Gleeble Testing of Tungsten Samples," *Army Research Laboratory,* 2013.
[111] Q. Qin, M.-L. Tian, and P. Zhang, "Investigation of a Coupled Arrhenius-Type/Rossard Equation of AH36 Material," *Materials,* vol. 10, no. 4, p. 407, 2017. [Online]. Available: https://www.mdpi.com/1996-1944/10/4/407.
[112] A. Blug *et al.*, "Real-Time GPU-Based Digital Image Correlation Sensor for Marker-Free Strain-Controlled Fatigue Testing," *Applied Sciences,* vol. 9, no. 10, p. 2025, 2019. [Online]. Available: https://www.mdpi.com/2076-3417/9/10/2025.
[113] B. Pan and L. Tian, "Superfast robust digital image correlation analysis with parallel computing," *Optical Engineering,* vol. 54, no. 3, pp. 034106-034106, 2015.
[114] T. Wang, Q. Kemao, H. S. Seah, and F. Lin, "A flexible heterogeneous real-time digital image correlation system," *Optics and Lasers in Engineering,* vol. 110, pp. 7-17, 2018/11/01/ 2018, doi: https://doi.org/10.1016/j.optlaseng.2018.05.010.
[115] V. Hansen, A. Vevecka-Priftaj, J. Fjerdingen, Y. Langsrud, and J. Gjønnes, "The Influence of Silicon on Age Hardening Kinetics and Phase Precipitation in Al-Mg-Zn Alloys," *Materials Science Forum,* vol. 519-521, pp. 579-584, 2006, doi: 10.4028/www.scientific.net/MSF.519-521.579.
[116] J. Y. Hwang, H. Doty, and M. Kaufman, "The effects of Mn additions on the microstructure and mechanical properties of Al–Si–Cu casting alloys," *Materials Science and Engineering: A,* vol. 488, pp. 496–504, 08/15 2008, doi: 10.1016/j.msea.2007.12.026.
[117] R. Zhang, W. Wang, J. Lin, and T. A. Dean, "An indirect hot form and Quench (HFQ) for manufacturing components of aluminum alloy sheets and comparison with direct HFQ," *International Journal of Machine Tools and Manufacture,* vol. 192, 2023, doi: 10.1016/j.ijmachtools.2023.104073.
[118] M. Van Rooyen and T. Becker, *A 3D-DIC Method for High Temperature Application*. 2015.
[119] S. Chen, R. Zhang, Z. Shi, and J. Lin, "An improved DIC method for full-field strain measurement in tensile tests on aluminium alloys under hot stamping conditions," *International Journal of Lightweight Materials and Manufacture,* vol. 7, no. 3, pp. 438-449, 2024/05/01/ 2024, doi: https://doi.org/10.1016/j.ijlmm.2024.01.001.
[120] S. Chen, R. Zhang, Z. Shi, and J. Lin, "An improved DIC method for full-field strain measurement in tensile tests on aluminium alloys under hot stamping conditions," *International Journal of Lightweight Materials and Manufacture,* 2024/01/09/ 2024, doi: https://doi.org/10.1016/j.ijlmm.2024.01.001.
[121] W. S. LePage, S. H. Daly, and J. A. Shaw, "Cross polarization for improved digital image correlation," *Experimental Mechanics,* vol. 56, pp. 969-985, 2016.
[122] B. V. Farahani, R. Amaral, P. J. Tavares, P. M. Moreira, and A. d. Santos, "Material characterization and damage assessment of an AA5352 aluminium alloy using digital

image correlation," *The Journal of Strain Analysis for Engineering Design,* vol. 55, no. 1-2, pp. 3-19, 2020, doi: 10.1177/0309324719892727.
[123] S. G. K. Patro and K. K. sahu, "Normalization: a preprocessing stage," *arXiv preprint,* vol. arXiv:1503.06462, 2015, doi: 10.48550/arXiv.1503.06462.
[124] G. Van Houdt, C. Mosquera, and G. Nápoles, "A review on the long short-term memory model," *Artificial Intelligence Review,* vol. 53, no. 8, pp. 5929-5955, 2020, doi: 10.1007/s10462-020-09838-1.
[125] S. Zheng, K. Ristovski, A. Farahat, and C. Gupta, "Long Short-Term Memory Network for Remaining Useful Life Estimation," presented at the 2017 IEEE International Conference on Prognostics and Health Management (ICPHM), Dallas, TX, USA, 2017.
[126] S. Zheng, K. Ristovski, A. Farahat, and C. Gupta, "Long short-term memory network for remaining useful life estimation," in *2017 IEEE international conference on prognostics and health management (ICPHM)*, 2017: IEEE, pp. 88-95.
[127] G. Corrolate, *GmbH (2015) GOM Correlate Professional V8 SR1 Manual Basic*.
[128] A. Savitzky and M. J. E. Golay, "Smoothing and Differentiation of Data by Simplified Least Squares Procedures," *Analytical Chemistry,* vol. 36, no. 8, pp. 1627-1639, 1964/07/01 1964, doi: 10.1021/ac60214a047.
[129] C. R. Harris *et al.*, "Array programming with NumPy," *Nature,* vol. 585, no. 7825, pp. 357-362, 2020.
[130] E. A. El-Danaf, A. A. AlMajid, and M. S. Soliman, "Hot deformation of AA6082-T4 aluminum alloy," *Journal of Materials Science,* vol. 43, no. 18, pp. 6324-6330, 2008/09/01 2008, doi: 10.1007/s10853-008-2895-4.
[131] G. Song and S.-W. Lee, "Effects of temperature on surface-controlled dislocation multiplication in body-centered-cubic metal nanowires," *Computational Materials Science,* vol. 168, pp. 172-179, 2019/10/01/ 2019, doi: https://doi.org/10.1016/j.commatsci.2019.05.063.
[132] C. M. Sellars and W. J. McTegart, "On the mechanism of hot deformation," *Acta Metallurgica,* vol. 14, no. 9, pp. 1136-1138, 1966/09/01/ 1966, doi: https://doi.org/10.1016/0001-6160(66)90207-0.
[133] M. Taheri-Mandarjani, A. Zarei-Hanzaki, and H. R. Abedi, "Hot ductility behavior of an extruded 7075 aluminum alloy," *Materials Science and Engineering: A,* vol. 637, pp. 107-122, 2015/06/18/ 2015, doi: https://doi.org/10.1016/j.msea.2015.03.038.
[134] M. Kaltenbach, "The Levenberg-Marquardt Method and its Implementation in Python," 2022.
[135] P. Virtanen *et al.*, "SciPy 1.0: fundamental algorithms for scientific computing in Python," *Nature methods,* vol. 17, no. 3, pp. 261-272, 2020.
[136] G. R. Johnson, "A constitutive model and data for metals subjected to large strains, high strain rates and high temperatures," in *Proceedings of the 7th International Symposium on Ballistics, The Hague, Netherlands, 1983*, 1983.
[137] S. M. Cox and P. C. Matthews, "Exponential time differencing for stiff systems," *Journal of Computational Physics,* vol. 176, no. 2, pp. 430-455, 2002, doi: https://doi.org/10.1006/jcph.2002.6995.
[138] Y. Li, B. Gu, S. Jiang, Y. Liu, Z. Shi, and J. Lin, "A CDRX-based material model for hot deformation of aluminium alloys," *International Journal of Plasticity,* vol. 134, p. 102844, 2020, doi: https://doi.org/10.1016/j.ijplas.2020.102844.
[139] S. Kim, W. Ji, S. Deng, Y. Ma, and C. Rackauckas, "Stiff neural ordinary differential equations," *Chaos: An Interdisciplinary Journal of Nonlinear Science,* vol. 31, no. 9, p. 093122, 2021, doi: https://doi.org/10.1063/5.0060697.

[140] L. F. Shampine, "Error estimation and control for ODEs," *Journal of Scientific Computing,* vol. 25, pp. 3-16, 2005, doi: http://dx.doi.org/10.1007/BF02728979.
[141] D. W. Zingg and T. T. Chisholm, "Runge–Kutta methods for linear ordinary differential equations," *Applied Numerical Mathematics,* vol. 31, no. 2, pp. 227-238, 1999, doi: https://doi.org/10.1016/S0168-9274(98)00129-9.
[142] G. Orlando, A. Della Rocca, P. F. Barbante, L. Bonaventura, and N. Parolini, "An efficient and accurate implicit DG solver for the incompressible Navier–Stokes equations," *International Journal for Numerical Methods in Fluids,* vol. 94, no. 9, pp. 1484-1516, 2022, doi: https://ui.adsabs.harvard.edu/link_gateway/2021arXiv210707776O/doi:10.48550/arXiv.2107.07776.
[143] C. Rackauckas and Q. Nie, "Differentialequations. jl–a performant and feature-rich ecosystem for solving differential equations in julia," *Journal of Open Research Software,* vol. 5, no. 1, 2017, doi: http://dx.doi.org/10.5334/jors.151.
[144] Y. Li *et al.*, "Experimental investigation of tension and compression creep-ageing behaviour of AA2050 with different initial tempers," *Materials Science and Engineering: A,* vol. 657, pp. 299-308, 2016/03/07/ 2016, doi: https://doi.org/10.1016/j.msea.2016.01.074.